Material Exploration for Spin Transfer Torque-Magnetic Random Access Memory

Yishen Cui

Lincang, Yunnan, China

Bachelor of Science, Peking University, 2007

A Dissertation presented to the Graduate Faculty
of the University of Virginia in Candidacy for the Degree of
Doctor of Philosophy

Department of Physics

University of Virginia
August, 2013

_____

_____

_____

_____

CONTENTS

ABSTRACT

Spin Transfer Torque Magnetic Random Access Memory (STT-MRAM) has become increasingly important for the memory industry due to its projected scalability and performance. This key component of the memory is called a magnetic tunnel junction (MTJ), consisting of a trilayer of two magnetic and one insulating film whose resistance depends on the relative orientation of the magnetic layers. When writing the memory, one of the magnetic layers is fixed and the magnetization of the free layer can be rotated using a torque exerted by a spin polarized current. However, the critical polarized current density in conventional CoFeB-based MTJs is still too large, preventing the STT-MRAM size from scaling down. The objective of this dissertation is to examine new ferromagnetic materials as candidate electrodes in MTJs, with properties that can reduce the critical current density, and thus realize a practical STT-MRAM.

Materials of interest in this study include CoFeCrB, Co_2FeAl and MnAl, each showing advantages over CoFeB for STT-MRAMs in different ways such as reduced magnetization, low damping parameter and large perpendicular magnetic anisotropy. For CoFeCrB, as-deposited films were amorphous, but were α-*bcc* crystallized after annealing. The addition of Cr reduced the magnetization moment due to the antiferromagnetic coupling between Cr and Co/Fe. This work has shown the effect of Cr and B content on the crystallization and magnetic properties. With a high chemical ordering, Heusler alloy Co_2FeAl demonstrates a damping parameter at least three times lower than that of CoFeB. The efforts are devoted into achieving a very high film quality with high chemical ordering, which is critical in obtaining a low damping parameter. Besides, an interfacial perpendicular magnetic anisotropy of ~ 1.9×10^6 erg/cc was

introduced in Co_2FeAl/MgO interfaces annealed at 350 ˚C without an external magnetic field. These results indicate the significant benefits of using Co_2FeAl in reducing the critical current density of a perpendicular STT-MRAM. Ordered binary intermetallic τ-MnAl also demonstrates a large perpendicular magnetic anisotropy ∼ 5.34 x 10^6 erg/cc. The magnetization of τ-MnAl is much smaller than that of CoFeB, but robust enough for the STT-MRAM applications. Layer-by-layer deposition approach is developed to improve the degree of the chemical ordering in τ-MnAl. Different seeding conditions are studied to manipulate the crystal strains thus to optimize the perpendicular magnetic anisotropy. The damping parameter of τ-MnAl in my study is ∼0.033, lower than that of most perpendicular systems, yet not comparable to in-plane systems such as CoFeB.

This dissertation also explores spintronic devices including spin valves and magnetic tunnel junctions incorporating Co_2FeAl thin films. In pseudo spin valves ($Co_2FeAl/Cr/Co_2FeAl$), bilinear and biquadratic couplings are observed. The bilinear coupling shows an oscillatory behavior with the spacer thickness, while the biquadratic coupling demonstrates a significant dependence on the temperature. Co_2FeAl-based MTJs were developed. A well defined magnetic switching was achieved after proper optimizations of the junction structure and growth conditions.

ACKNOWLEDGEMENT

Hongxue Liu, Ryan Comes, Wenjing Yin, Wenbin Fan, Wei Chen, David Kirkwood, Melissa Commisso Dolph, Kevin West. It was a great pleasure to work in such an enjoyable environment everyday with them.

In the end, I would like to express my special gratitude to my parents and my husband Yuan for their unconditional love and support. I would like to dedicate this dissertation work to my dear parents, Yuan and our little one Amelia.

LIST OF TABLES

LIST OF FIGURES

1. Introduction

1.1 Marching to high density memories

Magnetic Random Access Memory (MRAM) was first introduced in the late 1980's to replace bulky and heavy plated wire radiation hard memories [1]. It utilizes the two-stage magnetoresistance of magnetic layered structures to encode "1" and "0" respectively. Anisotropic Magnetoresistive (AMR) materials were first adopted in the earliest MRAM memory architecture, in which the magnetoresistance depends on whether their magnetization is parallel or perpendicular to the current. However, the magnetoresistance change ratio is only 2% which doesn't meet the requirements for the MRAM application. Magnetoresistance ratio was greatly improved up to 20% after the discovery of Giant magnetoresistance (GMR)[2] but it is still way below the practical level to achieve a high performance of a MRAM. Additionally single GMR structure cannot be directly adapted to a front-end CMOS module due to its low resistance. Tunnel magnetoresistance (TMR) of a Magnetic Tunnel Junction (MTJ) provided a viable solution to both problems. A high magnetoresistance ratio was achieved ~220% in MgO-based MTJs in 2004[3, 4]. Besides the resistance of a MTJ can be effectively adjusted by varying the barrier layer thickness to match the underneath CMOS electronics.

The first commercial MRAM chip was introduced by Freescale Semiconductor in 2006. The magnetoresistance was manipulated by an external magnetic field generated by an electric current delivered through a pass transistor. 180 nm and 90 nm nonvolatile MRAM products are applied in various areas such as satellite applications and automotive data recorders with fast read/write speed and nearly unlimited endurance. On

the other hand, conventional MRAMs are greatly challenged as the bit size is scaled down beyond the 45 nm node. With the same retention time, the writing current increases inversely proportional with the MTJ size, preventing the memory bit from scaling down with the pass transistors. The scalability issue stimulated the introduction of the second generation MRAM: Spin Torque Transfer-MRAM (STT-MRAM). Spin torque transfer was first predicted in 1996[5, 6], with which the magnetization of a nanomagnet can be manipulated via a spin polarized current. STT-MRAM writes memory units utilizing a spin polarized current, which in theory leads to a breakthrough for magnetic random access memory (MRAM) to scale properly with Si CMOS transistors. Additionally STT-MRAM has the potential to meet both the endurance and speed requirements, which make it a strong candidate for a "Universal" memory (Table 1-1). The first STT-MRAM products have been launched by one of the MRAM leaders Everspin Technologies in the end of 2012.

Table 1-1 Comparison of the performance of STT-MRAM with other conventional semiconductor memories. The red font indicates the shortcomings of the corresponding memory technology.

	SRAM (45 nm)	DRAM (45nm)	Flash (45nm)	MRAM (180nm)	STT-MRAM (45nm)
Non-volatile	No	No	Yes	Yes	Yes
Cell size (μm^2)	0.18	0.03	0.03	1.25	0.03
Read time (ns)	0.5	1	10-50	35	5
Write time (ns)	0.5	1	0.1-100ms	5	5
Endurance	$>10^{15}$	$>10^{15}$	$>10^{15}$ read $>10^6$ write	$>10^{15}$	$>10^{15}$
Write power	5 pJ	0.02 pJ Needs refresh	10 nJ	150 pJ	0.04 pJ

1.2 Challenges for STT-MRAM

The main challenge for commercializing STT-MRAM products is to reduce the polarized writing current density. Grandis reported the first STT switching in a Al_2O_3-based MTJ with J_c less than 10^7 A/cm^2[7], and the critical current density was further reduced to 2-3x10^6 A/cm^2 in a MgO-based MTJ[8]. Yet the critical current density doesn't meet the practical level. As shown in Figure 1-1, a current density at the level of 5x10^5 A/cm^2 is highly desired to scale down the memory size with the CMOS transistors.
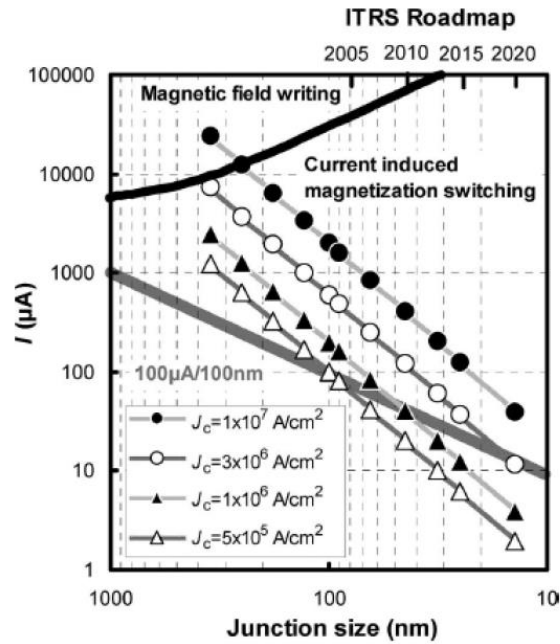
Figure 1-1 Switching currents required in STT-MRAMs as a function of MTJ size for various values of the current density (Solid dots: 1x10^7 A/cm^2; open dots: 3x10^6 A/cm^2; solid triangles: 1x10^6 A/cm^2; open triangles: 5x10^5 A/cm^2). The grey line stands for the maximum current a CMOS transistor can deliver as a function of the transistor size. The black line represents the writing current required in conventional MRAMs varied with the MTJ size, which clearly indicates the scalability problem in conventional MRAMs.(adapted from NSF EAGAR Proposal- Stuart A.Wolf)

A low polarized current density ~ 1x10^6 A/cm^2 has been achieved by introducing dual MTJ structures consisting of two insulating barriers of different resistances[9]. On

the other hand, the current density can be significantly reduced by engineering the intrinsic properties of ferromagnetic materials used in MTJs, such as magnetization, damping parameter, spin polarization and magnetic anisotropy. Particularly, the polarized current density has been reduced to 3.6×10^6 A/cm^2 by adopting TbCoFe, which has a perpendicular magnetic anisotropy[10]. This dissertation is focused on material exploration aimed at lowering the critical current densities for a high performance STT-MRAM technology.

1.3   Dissertation outline

This dissertation work is devoted into material exploration with the purpose of reducing the critical current density for STT-MRAM applications. The materials in focus include CoFeCrB, CoFeAl and MnAl.

Chapter 2 introduces the basic physics of spintronics and how it is applied in MRAMs. The working principles of MTJ in both conventional MRAMs and STT-MRAMs are reviewed in detail. Material properties desired to improve the STT-MRAM performance are derived by theory. Candidate materials for STT-MRAM applications are introduced accordingly.

Chapter 3 describes the experimental techniques used in this work including thin film fabrication, processing and characterization.

Chapter 4 is focused on Cr diluted-CoFeB. The structural and magnetic properties varied as a function of CoFeCrB composition are discussed in depth.

Chapter 5 describes the growth of ordered Heusler alloy Co_2FeAl. The correlations between the degree of chemical ordering and properties such as the magnetization,

damping parameter and spin polarization are investigated extensively. Interfacial perpendicular magnetic anisotropy is achieved by introducing Co_2FeAl/MgO interfaces.

Chapter 6 presents results on ordered binary intermetallic MnAl, which features large crystalline perpendicular magnetic anisotropy. The effect of lattice strain on the MnAl magnetic anisotropy is discussed.

Chapter 7 involves some preliminary results of spintronics devices. Dependence of interlayer couplings on spacer thickness and temperature in pseudo spin valves are studied. Some tentative efforts are made to improve the performance of MTJs, including MgO barrier layer optimization and exchange bias optimization.

The dissertation work is summarized in Chapter 8. A cross comparison is presented between the three candidate materials along with some directions for the future work.

2. Background

This chapter provides the background information related to this dissertation. It starts from the spin dependent transport in ferromagnetic materials, which forms the basis of the spin-based electronics. The magnetic tunnel junction (MTJ) is introduced as a key component in MRAM, as well as the mechanisms of tunnel magnetoresistance (TMR). While the conventional MRAM is greatly challenged in its scalability, the spin torque transfer (STT) emerges as a viable pathway toward high memory density, low energy cost, and high endurance and speed. The advantages and challenges of STT-MRAM are discussed in detail in comparison with conventional MRAM. I will also review parameters affecting the critical switching current as well as the thermal reliability of STT-MRAMs. Candidate ferromagnetic materials for STT-MRAM applications are discussed in the last section.

2.1 Spin dependent transport in ferromagnetic materials

Spintronics is based on electrical transport with the additional degree of freedom, 'spin'. The 'two currents' model of conduction was first proposed by Mott[11] in 1936 to describe the electrical transport in ferromagnetic materials. It is suggested that in ferromagnetic materials currents are carried by spin-up and spin-down electrons in parallel with different conductivities at the limit where spin-flip scattering events are negligible. This spin-dependent transport can be understood by carefully scrutinizing the density of states (DOS) with different orbital symmetries at the Fermi level. Figure 2-1 shows schematically the density of states of Co for bands 4s and 3d, both of which expand to the outer shell reaching the Fermi level. A split was found in 3d electronic

band due to the exchange interaction, which also explains the ferromagnetism. Specifically, the net magnetization is induced because more electrons are filled into the spin-up band (thus named as majority band) than those falling into the spin-down band (minority band).
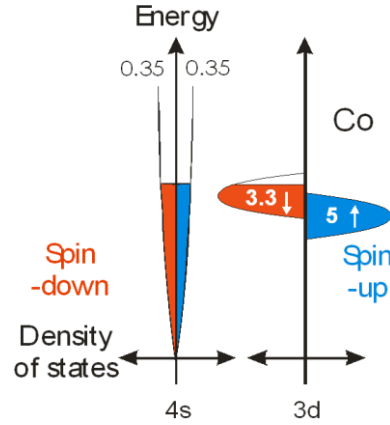
Figure 2-1 Density of states of Co (schematic). The blue halves are filled with spin-up electrons while the red parts are filled spin-down electrons. The numbers indicate the magnetic moment per atom for each band. (adapted from lecture notes for *Spin Transport, Dynamics and Quantum Information*, Prof. Stu Wolf, UVA 2013)

The s electrons with a small effective mass carry most of the electronic current. The transport resistance is mainly resulted from the electron scattering which obeys Fermi's golden rule (Equation **(2-1)**)[12]:

$$T_{i \to f} = \frac{2\pi}{\hbar} |\langle f|H'|i \rangle|^2 \rho \qquad \text{(2-1)}$$

$T_{i \to f}$ is the scattering possibility from the initial to final states. $\langle f|H'|i \rangle$ is the matrix element of the perturbation H' between the initial and final states and ρ is the DOS of the final states. In the case of ferromagnets, the resistance induced by s to d scattering is dominant compared to that by s to s, given the much larger DOS of 3d band than that of

4s band at the Fermi level. Additionally, the shifting within the 3d bands leads to an imbalance of the DOS at the Fermi level between the spin-up band and the spin-down band. According to Fermi's golden rule, electrons experience a much stronger scattering from the spin-down band (minority) than that from the spin-up band (majority) in the case shown in Figure 2-1. Thus the electric current is polarized after passing through ferromagnetic materials (Figure 2-2).
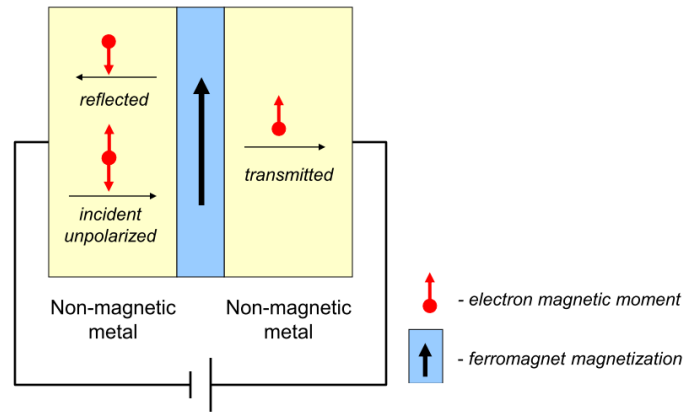
Figure 2-2 Spin polarized current after passing through the ferromagnetic layer. (adapted from Ref[13])

The spin polarization is defined as:

$$P = \frac{N_\uparrow - N_\downarrow}{N_\uparrow + N_\downarrow} \qquad \text{(2-2)}$$

$N_{\uparrow(\downarrow)}$ is the DOS at the Fermi level for the spin-up (spin-down) channel. One should notice that the majority spin channel does not necessarily hold a larger conductance. Instead the DOS at the Fermi level for each channel determines how the current is polarized. In non-ferromagnetic metals such as Cu, spin polarization is close to 0%. For Half metals such as CrO_2, spin polarization is above 90%[14].

2.2   Magnetic Tunnel Junction (MTJ)

2.2.1   Giant magnetoresistance (GMR)

The history of spintronics starts from the discovery of Giant magnetoresistance (GMR) in artificial Fe/Cr magnetic superlattices in 1988[15, 16]. The lowest resistance (R_P) is achieved when the magnetic moments of the ferromagnetic layers are parallel (P state) with each other while the highest resistance (R_{AP}) occurs when they are antiparallel (AP state) (Figure 2-3). The magetoresistance ratio (MR) is defined as:

$$MR = \frac{R_{AP} - R_P}{R_P} \qquad \text{(2-3)}$$
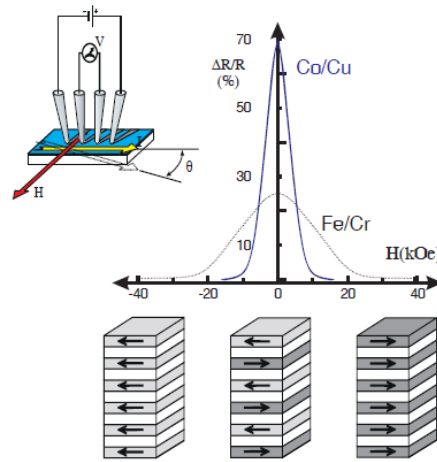
Figure 2-3 GMR~70% at room temperature observed in Co/Cu superlattice structures. Parallel magnetization alignment corresponds to low resistance while antiparallel alignment corresponds to high resistance. (adapted from Ref[17])

The discovery of GMR triggered the research for spin valves, which have a sandwiched structure of FM/N/FM. The magnetization of one of the ferromagnetic layers is pinned by an exchange bias through an intimate contact with an antiferromagnetic

layer[13, 18], while the other FM is relatively free to be switched when subjected to a magnetic field. Metallic layers such as Cu or Ru are used as the non-magnetic layer N in the case of spin valves (Figure 2-4). GMR Spin valve sensors demonstrated a higher sensitivity compared to AMR sensors. According to a report from IBM, the growth rate for the storage areal density was increased up to 100% per year by introducing the spin valve head into hard disk drive (HDD) read head[12]. However the MR readout of a spin valve still remains below ~ 20% in room-temperature operations even with a current-perpendicular-to-plane (CPP) configuration[2]. The low sensitivity does not satisfy the requirements for solid-state magnetic storage such as MRAM. Furthermore, the low metallic resistance of several Ohms is not well adapted to CMOS electronics[12, 19].
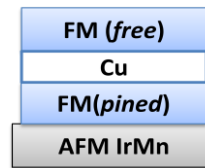
Figure 2-4 Schematic structure of a spin valve. IrMn is used as the antiferromagnetic layer while Cu is the non-ferromagnetic spacer in this case.

2.2.2 Tunnel magnetoresistance (TMR)

These technical challenges were resolved by introducing the Magnetic Tunnel Junction (MTJ) in which the metallic spacer is replaced by an insulating one (Figure 2-5). In 1975, Julliere observed tunnel magnetoresistance (TMR) in a MTJ structure of Fe/Ge-O/Fe[20]. The TMR effect was as low as 14% only at a low temperature of 4.2 K and didn't draw much attention at first until the discovery of GMR. In 1995, Giant TMR

~30% was observed at 4.2 K and ~18% at 300K with Al_2O_3 as the spacer layer[21]. The

TMR record of Al_2O_3-based MTJs achieved ~70% at room temperature in 2004[22].
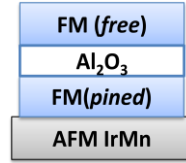
Figure 2-5 Schematic structure of a magnetic tunnel junction. IrMn is used as the antiferromagnetic layer while Al_2O_3 is the insulating spacer in this case.

Figure 2-6 shows the spin-dependent electron tunneling model with different

magnetization configurations (P and AP states) as proposed by Julliere. Spin is conserved

during the tunneling process. The tunneling becomes more efficient with P states, where

electrons find more free states to tunnel to, compared to AP state. The current I_P (I_{AP}) in

P (AP) configuration can be roughly expressed as follows:

$$I_P = N_\uparrow^1 N_\uparrow^2 + N_\downarrow^1 N_\downarrow^2 \qquad \text{(2-4)}$$

$$I_{AP} = N_\uparrow^1 N_\downarrow^2 + N_\downarrow^1 N_\uparrow^2 \qquad \text{(2-5)}$$

The superscript numbers 1 or 2 of $N_{\uparrow(\downarrow)}$ indicates the FM layers in concern. With the

definitions of spin polarization (P) **(2.2)** and magetoresistance ratio (MR) **(2.3)**, one can

easily deduce the tunnel MR for a MTJ:

$$TMR = \frac{2P_1P_2}{1-P_1P_2} \qquad \text{(2-6)}$$
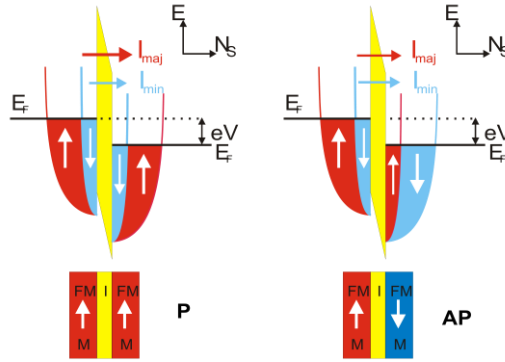
Figure 2-6 Spin dependent tunneling in Magnetic Tunnel Junctions with parallel magnetization state and antiparallel magnetization state. (adapted from lecture notes for *Spin Transport, Dynamics and Quantum Information*, Prof. Stu Wolf, UVA 2013)

2.2.3 Incoherent and coherent tunneling in MTJs

In Julliere's model, TMR is only determined by the spin polarizations of the ferromagnetic electrodes regardless of the barrier layer. However a discrepancy was noticed between the theoretical and experimental estimations for the MR ratios in MTJs with amorphous Al-O tunnel barriers[23]. The room-temperature TMR ratio hit a limit ~70% with an Al-O barrier[22] and didn't show a significant increase even with electrodes of high spin polarizations[24]. The discrepancy continued unresolved until 2001, when Butler predicted a coherent spin-dependent tunneling in MTJ with a crystalline barrier MgO(001)[25]. In 2004, giant TMR up to 220% was demonstrated by Parkin *et al*. [3] and Yuasa *et al*. [4] independently in single-crystal Fe/MgO/Fe MTJs.

In ferromagnetic electrodes Bloch states exist with various orbital symmetries. In 3d ferromagnetic electrodes such as Fe(001), the Bloch state with a Δ_1 symmetry (spd hybridized) has a large positive spin polarization while other states with a lower symmetry such as Δ_5 and $\Delta_{2'}$ have a negative spin polarization. Figure 2-7 shows the band

dispersion curve for different Bloch states in Fe in the [001] direction, which clearly indicates a fully polarized Δ_1 band at the Fermi level (P=1), even though the averaged spin polarization of Fe is relatively small[23].
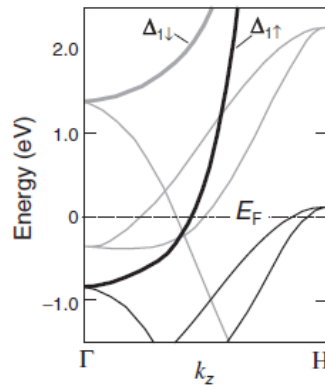
Figure 2-7 Band dispersion of Fe in the [001] direction. The grey lines stand for the minority bands and black lines for the majority bands. (adapted from Ref[23])

In fact, two different tunneling processes in MTJs are expected depending on the type of the tunnel barrier. In a fully incoherent tunneling process proposed in Julliere's Model, no crystallographic symmetry is expected in the tunnel barrier and the barrier/ferromagnet interfaces. Various Bloch states with different spin polarizations tunnel through the barrier layer by coupling with the evanescent states in it. The tunneling probabilities are equal for all the states with different symmetries thus averaging down the net spin polarization. On the other hand, coherent tunneling process can be introduced into MTJs by using a crystalline tunnel barrier such as MgO(001). Evanescent states with three kinds of symmetries Δ_1, Δ_5 and $\Delta_{2'}$ exist in the band gap of MgO(001). Given that the state symmetries are conserved during tunneling, the Bloch states couple with the evanescent states with corresponding symmetries and tunnel

though the barrier with different tunneling probabilities. Particularly, with the parallel magnetization configuration, the Δ_1 state has the slowest decay in MgO(001) and the electron tunneling with Δ_1 symmetry becomes dominant with a large positive spin polarization. Other states with a negative spin polarization such as Δ_5 and $\Delta_{2'}$ decay much faster, so a much larger spin polarization is expected after averaging. Figure 2-8 compares the tunneling processes through the amorphous Al-O and MgO(001) barriers. It should be noticed that the tunneling though the amorphous Al-O barrier is between the fully incoherent tunneling process and the coherent one.
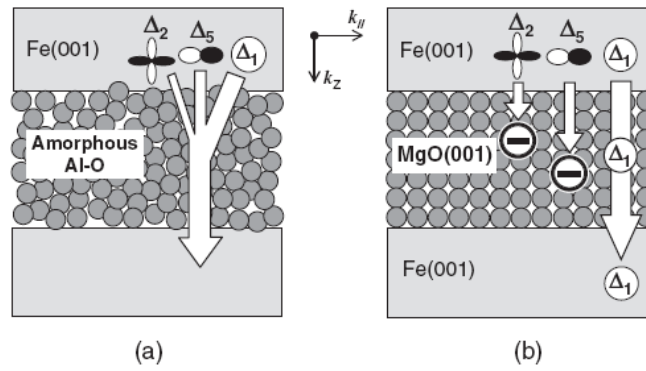
Figure 2-8 Tunneling processes in Al-O based MTJs and MgO based MTJs. (adapted from Ref[23])

To achieve the coherent tunneling process thus a giant TMR ratio in MgO-based MTJs, a MgO(001) barrier layer with an ideal oxidation condition at the barrier/electrode interfaces is used. It has been pointed out that the Δ_1 state of 3d transition metals does not couple effectively with the MgO Δ_1 state with excess oxygen at the interface[26]. Besides, given the non-*bcc* structure of the bottom antiferromagnetic layer, ferromagnetic electrodes that maintain an amorphous state before annealing but crystallize into a *bcc* structure after the heat treatment are preferred in order to suppress undesired crystal

orientations in MgO. One of the examples is CoFeB as shown in Figure 2-9. Boron functions as an 'amorphizer' and maintains the amorphous state of CoFeB even when grown on a $fcc(111)$-oriented layer such as antiferromagnetic IrMn[27]. Therefore it stops the propagation of epitaxial growth from the bottom structures. On an amorphous electrode layer, (001)-oriented polycrystallinity can be achieved in the MgO barrier. With the seeding effect from the MgO layer, a coherent bcc structured interface between CoFeB and MgO forms after annealing, resulting in a giant TMR ratio[23].
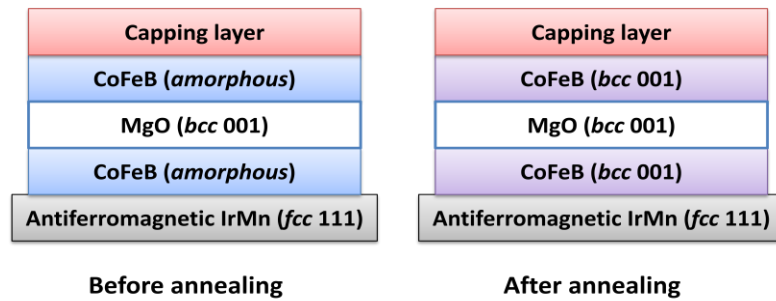
Figure 2-9 Schematic for the crystallizations of the CoFeB/MgO/CoFeB junction before and after annealing.

2.2.4   Interlayer couplings

Interlayer exchange coupling has been widely observed in stack structures with ferromagnetic layers[28, 29]. Tailoring the interlayer coupling is important to achieve ideal P or AP states in spin valves or MTJs. Specifically, one of the ferromagnetic layers is expected to be coupled to an antiferromagnetic layer through an exchange bias and switched only at a large field (pinned layer). On the other hand, the other ferromagnetic

layer is expected to be decoupled from the pinned layer and easily switched with a relatively small field (free layer) (Figure 2-4).

(i)   Exchange bias between ferromagnetic(FM) and antiferromagnetic(AFM) layers

Exchange bias can be obtained by cooling the AFM/FM bilayer in a magnetic field from a temperature above the Néel temperature of the AFM layer. The center of FM hysteresis loop is shifted to a non-zero field (H_{ex}) with an increased coercive field due to the exchange bias coupling[18]. Figure 2-10 shows an intuitive picture of the mechanism of exchange bias, which ignores practical parameters such as magnetic domain configurations of the FM and AFM layers and interface roughness. When the temperature is above the Néel temperature of the AFM layer (T_N) but below the Curie temperature of the FM layer (T_C), the magnetic moments of FM layer are aligned along the external magnetic field while those of the AFM layer stay random(i). As the temperature is decreased below T_N, the magnetic moments are aligned with an antiferromagnetic order with the interfacial spins of the AFM layer ferromagnetically aligned with those of the FM layer(ii). In other words, the AFM spins at the interface exert a microscopic torque on the FM spins. Therefore, more energy and thus a larger coercive field is required to switch the magnetization of the FM layer from the original direction to the opposite direction(iii). On the other hand, the magnetization of the FM layer can be switched at a smaller field as it is switched back to the original direction, since the AFM spins exert a torque in the same direction as the external field in this case(iv to v).
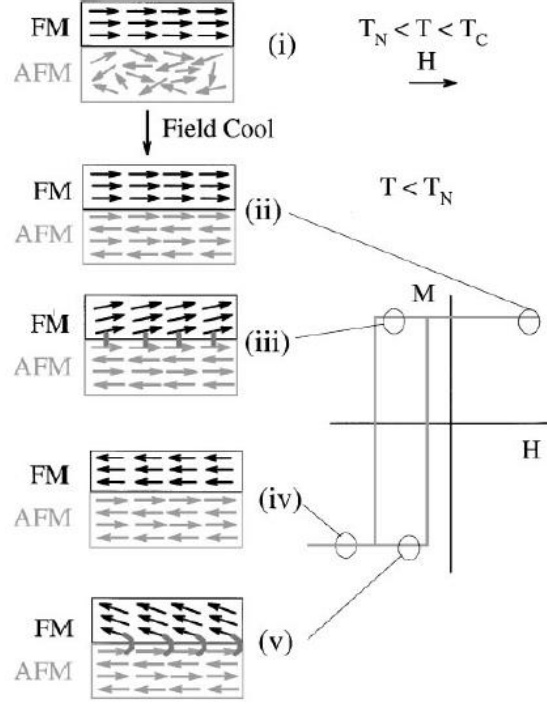
Figure 2-10 Intuitive mechanism of the exchange bias coupling in a AFM/FM bilayer structure. (i)-(ii) shows how the exchange bias is established in the structure. (iii)-(v) shows how the exchange bias affects the switching behavior of the FM layer in an external field. (adapted from Ref[18])

Under the assumption of coherent rotation of the magnetization, the energy per unit area in an AFM/FM bilayer system can be written as[18]:

$$E = -HM_{FM}t_{FM}cos(\theta - \beta) + K_{FM}t_{FM}sin^2(\beta)$$

$$+K_{AFM}t_{AFM}sin^2(\alpha) - J_{INT}cos(\beta - \alpha) \qquad (2\text{-}7)$$

Here, H is the external field, M_{FM} is the magnetization of the FM layer and t_{FM} and t_{AFM} are the thicknesses of the FM and AFM layers respectively. K_{FM} and K_{AFM} are the magnetic anisotropy of the corresponding layers. J_{INT} is the interface coupling constant. Assuming K_{FM} and K_{AFM} are in the same direction, α represents the angle between the AFM sublattice magnetization and the anisotropy direction. β represents the angle

between the FM magnetization and the anisotropy direction. $\theta - \beta$ is the angle between the external field and the FM magnetization. In the conditions of $K_{AFM}t_{AFM} \gg K_{FM}t_{FM}$, which is satisfied in most cases, one can obtain the exchange bias field by minimizing the energy with respect to α and β:

$$H_e = \frac{J_{INT}}{M_{FM}t_{FM}} \qquad \text{(2-8)}$$

with the following condition satisfied:

$$K_{AFM}t_{AFM} \gg J_{INT} \qquad \text{(2-9)}$$

The condition (2.9) indicates that in an ideal case where J_{INT} is smaller than $K_{AFM}t_{AFM}$, the AFM spins would stay in the original direction as the FM spins is rotated in an external field while. Therefore it exerts an unidirectional exchange bias on the FM spins thus leading to an non-zero H_{ex} as shown in Figure 2-10. In a less ideal case, $K_{AFM}t_{AFM}$ is comparable to or smaller than J_{INT}, H_{ex} is close to zero but the coercive field for the FM spin switching is enhanced due to the coupling with AFM spins.

(ii) Coupling between two ferromagnetic layers

The coupling between the two ferromagnetic layers is a practical concern in affecting TMR in MTJs[30, 31]. For example, ferromagnetic coupling between the free and fixed layers in a MTJ exerts an extra bias field on the free layer switching. The TMR value could be significantly reduced if the magnetizations of the free and fixed layers are coupled and switched simultaneously. Phenomenologically, the interlayer couplings can be described as:

$$E = -J_1 \, \overrightarrow{m_1} \cdot \overrightarrow{m_2} - J_2 \, (\overrightarrow{m_1} \cdot \overrightarrow{m_2})^2 \qquad \text{(2-10)}$$

The first term is called bilinear coupling because the energy is linear with the magnetizations of both layers. $0^o/180^o$ alignments are expected with a dominant bilinear coupling. Specifically, positive values of J_1 correspond to a ferromagnetic coupling (0°) while negative values correspond to an antiferromagnetic one (180°). The second term is called biquadratic coupling and induces 90° coupling with a negative J_2[29].

For an ideal homogeneous magnetic multilayer, a well known example of bilinear coupling is the Rudermann-Kittel-Kasuya-Yosida (RKKY) type coupling mediated by conduction electrons confined between the magnetic layers[32, 33]. Oscillations of the exchange coupling were observed with an increasing spacer thickness. In a general sense, the oscillation is critically determined by the sharp cut-offs in momentum space due to the Fermi surface of the spacer layer. The increase in the spacer thickness leads to an energy shift of quantum well states relative to the Fermi level, and thus $0^o/180^o$ alignments appeared alternatively for a minimum energy[29].

When it comes to the realistic case of magnetic layered structures, magnetostatic couplings are also common due to the interface roughness. Two types of coupling arise from magnetostatic interactions at a microscopic scale. The first one is Néel coupling (or orange peel coupling) in layered structures with a correlated or conformal roughness. The fringing field introduced by the rough interface can be equivalently considered as magnetic "charge"[29]. Figure 2-11 shows the magnetic "charge" distribution along the electrode interfaces. As the two ferromagnetic electrodes are close enough, a bilinear ferromagnetic coupling is induced and recognized as Néel coupling.
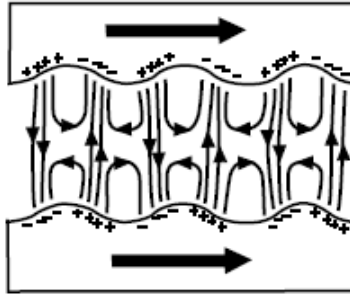
Figure 2-11 N éel coupling between ferromagnetic layers with a correlated interface. (adapted from Ref[29])

On the other hand, 90° biquadratic couplings can be induced with an uncorrelated roughness (Thickness fluctuation model)[34, 35]. In most systems bilinear interlayer coupling oscillates between positive and negative (RKKY coupling for example) within the thickness variation of one monolayer. If the interface roughness fluctuates by one monolayer and the width of the fluctuating terrace is less than the domain wall thickness, the exchange stiffness tends to resist the change of the bilinear coupling (Figure 2-12). Near-90° biquadratic couplings are thus established to minimize the total energy of bilinear interlayer coupling and stiffness energy[35].
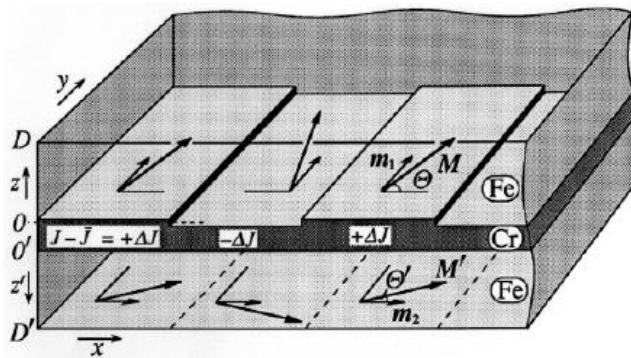
Figure 2-12 Thickness fluctuation model for the biquadratic coupling in Fe/Cr/Fe structure. The interlayer terrace fluctuates by one monolayer periodically. (adapted from Ref[34])

To minimize magnetostatic interlayer coupling in magnetic multilayer structures such as MTJs, engineering the smoothness of the interfaces becomes essential.

2.3   Challenges of conventional MRAMs

The MTJ plays a key role in Magnetic Random Access Memory (MRAM). Figure 2-13 shows the MRAM bit cell in the one transistor per magnetic tunnel junction (1T1J) design, and illustrates how it is operated in Read and Program Modes. The high resistance state (AP state) and the low resistance state (P state) correspond to information '1' and '0' respectively. In the read mode, the transistor is switched on to allow the read current to pass through the MTJ and recognize the resistance state. In the program mode, the isolation transistor is at 'OFF' position. Currents are sent through the bit line and digit line which are orthogonal to each other generating magnetic fields to manipulate the magnetization of the free electrode.
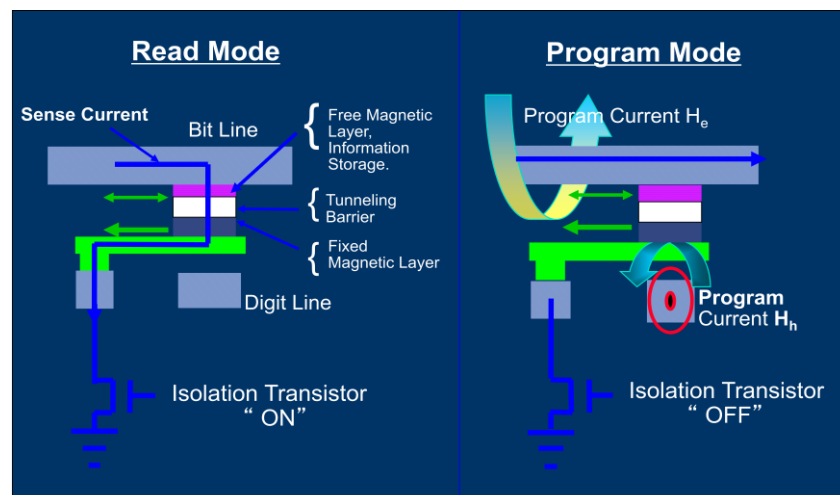
Figure 2-13 Read and Program modes in MRAM cell bit with 1T1J design. (adapted from lecture notes for *Spin Transport, Dynamics and Quantum Information*, Prof. Stu Wolf, UVA 2013)

Nonvolatile conventional MRAM has shown a high performance compared to other memories. It can become a universal memory that directly fits into a back end of line process on the CMOS module. It has a fast read and program time, high endurance and a low energy cost. However, conventional MRAM is not scalable as the memory size is scaled down beyond 65 nm. The retention time required for storage memories is 10 years. For magnetic recordings, the retention time is determined by the thermal stability Δ defined as follow:

$$\Delta = \frac{K_u V}{k_B T} \qquad \text{(2-11)}$$

K_u is the magnetic anisotropy and simply proportional to the magnetization (*m*) and the anisotropy field (H_k) of the information storage layer (free layer) and *V* is the layer volume. $k_B T$ is the thermal fluctuation energy at a temperature of *T*. A large anisotropy energy $K_u V$ is necessary to prevent the magnetization from being randomly flipped by thermal perturbation thus ensuring the reliability of the memory bit. Particularly, a thermal stability of ~60 is required for 10-year retention time of magnetic recordings. As the size of the storage layer is scaled down below 65 nm, an enhanced K_u is required to compensate the decrease of *V* to maintain the same thermal stability. However, writing becomes a major problem because the write field, thus the write current, increases proportionally with the K_u of the free layer and eventually reaches the limit placed by the matching wirings and transistors. This is a general problem in magnetic recordings not only in MRAM but also in HDD, leading to the introduction of heat-assisted magnetic recording (HAMR)[36]. For conventional MRAM, the situation becomes even worse given the much smaller dimension of the conducting lines with a strong limitation in the current density[12].

2.4   Spin Torque Transfer and STT-MRAMs

2.4.1   Spin torque transfer

Spin torque transfer (STT) was predicted by Berger[6] and Slonczewski[5] independently in 1996. It was predicted that the magnetization of a nanomagnet can be rotated by a torque carried by spin polarized current. The mechanism of STT switching from the AP state to the P state is shown in Figure 2-14. The ferromagnetic fixed layer functions as a spin polarizer aligning the spins carried by the current towards the magnetization of the fixed layer. As the polarized spins reach the free layer, the s-d exchange interaction again quickly aligns the spins towards the local magnetization[6]. On the other hand, the transverse magnetic moments lost by the spins are transferred to the free layer, aligning its magnetization towards that of the fixed layer[12]. The STT switching technique fits well into MgO-MTJs given that the spin polarization is greatly improved by coherent tunneling.
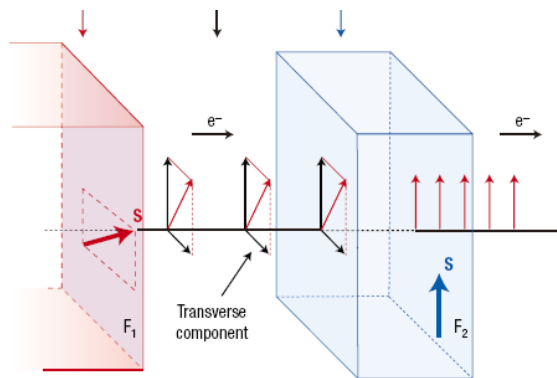
Figure 2-14 Spin torque transfer in FM/NM/FM structures. The red layer is the fixed layer while the blue layer represents the free layer. (adapted from Ref[12])

From the magnetic dynamics at a microscopic scale, the motion of the free layer magnetization is described by the Landau-Lifshitz Gilbert (LLG) equation including the spin torque transfer term [5, 37-39]:

$$\frac{d\overrightarrow{m}}{dt} = -\gamma(\overrightarrow{m} \times \overrightarrow{H}_{eff}) + \alpha\left(\overrightarrow{m} \times \frac{\partial\overrightarrow{m}}{\partial t}\right) - \beta[\overrightarrow{m} \times (\overrightarrow{m} \times \overrightarrow{p})] \qquad \text{(2-12)}$$

The first term corresponds to the field torque. $\overrightarrow{m}$ is the magnetic moment of the free layer in a single domain size, γ is the gyromagnetic factor, $\overrightarrow{H}_{eff}$ is the effective field exerted on the free layer. In an ideal MTJ (no coupling between the free layer and the fixed layer), $\overrightarrow{H}_{eff}$ includes the field applied externally $\overrightarrow{H}_{ex}$, the intrinsic anisotropy field $\overrightarrow{H}_k$ as well as demagnetizing field $\overrightarrow{H}_d$ which will be discussed in detail in Section **2.4.2**. The second term is the damping torque due to spin-orbital interaction in the free layer. α is the Gilbert damping parameter. The third term gives the spin torque exerted by the polarized current. $\overrightarrow{p}$ is the spin current polarization. β is the spin torque parameter determined by m, p, and $g(\theta)$, a function of the angle θ between the free layer magnetization vector and the polarized spin orientation:

$$\beta \propto \frac{pg(\theta)}{m} \qquad \text{(2-13)}$$

Generally $g(\theta)$ and thus β increases monotonically with θ, leading to more efficient STT-switching. Figure 2-15 illustrates the effects of the three terms during the free layer switching. The field torque causes the precession of the free layer magnetization. In devices such as spin torque oscillators it is critical to maintain a stable magnetization precession. The damping torque dissipates the precession energy and tends to restore the magnetization back to the equilibrium positions. The spin torque balances with the

damping torque, and in STT-MRAMs it switches the magnetization between two stable points when the spin current overcomes the damping effect.
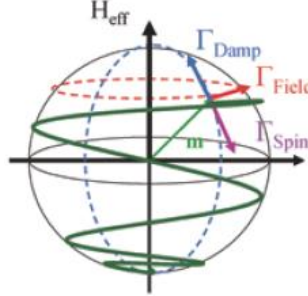
Figure 2-15 Magnetization switching under the effects of the field torque Γ_{field}, damping torque Γ_{damp}, and spin torque Γ_{spin}. (adapted from Ref[39])

Based on this model, the critical current density for free layer switching at zero temperature is given by equation **(2-14)**[38-40]:

$$J_{c0} = \left(\frac{2e}{\hbar}\right)\left(\frac{\alpha t_F m}{pg(\theta)}\right)\left(H_{eff}\right) \qquad \text{(2-14)}$$

2.4.2 Advantages and challenges of STT-MRAM

The mechanism of STT writing allows the high scalability of STT-MRAMs. One would notice that unlike in conventional MRAMs, the write current in STT-MRAMs linearly scales down with the junction size (the cross-sectional area). STT-MRAMs have a much simpler architecture without the digit lines and claddings that are utilized in conventional MRAMs. Additionally, since the memory cell is written by a localized spin current instead of an external magnetic field, the write margin problem for conventional MRAMs is eliminated and results in a better write selectivity[41]. Besides, compared to

other universal memories, STT-MRAMs have a fast read/write speed, a high endurance, and a low energy consumption because of the small write current[42].

On the other hand, to realize the STT writing in memory cells with high scalability and reliability, it is crucial to minimize the write current density while maintaining a large thermal stability. For STT-MRAMs in 1T1J design, a large write current prevents the transistor from scaling down with the MTJ because the maximum current the transistor can deliver is proportional to its size. Besides, a large voltage across the junction could induce high risk of the tunnel barrier breakdown [19]. The typical current density is ~ 5 x 10^5 A/cm^2 in practical STT-MRAM application. The write current density can be reduced from both material and device design aspects. By scrutinizing equation **(2-14)**, one would expect to lower the current density by engineering several intrinsic properties of the free layer material.

(i) Magnetization

The most explicit way to reduce the critical current density is to reduce the free layer magnetization, which is also one of the advantages of CoFeB over CoFe. The magnetization could be further reduced by introducing antiferromagnetic or non-magnetic elements into CoFeB. However, the improvement by reducing the magnetization is quite limited, considering the fact that a small magnetization also undermines the thermal stability (equation **(2-11)**).

(ii) Magnetic anisotropy field

Magnetic anisotropy field is critical to both the switching current density and the thermal stability. It is introduced to describe the 'easy' and 'hard' magnetization axis in a magnetic body. It acts as an intrinsic magnetic field tending to align the magnetization

vector along certain directions. In most of the thin film cases the magnetic anisotropy is in the film plane or perpendicular to the film plane phenomenally, but the origins can be quite different.

In free layers with an in-plane anisotropy, shape anisotropy is usually dominant due to the demagnetizing field. Generally, a demagnetizing field is always in a direction opposite to the direction of the magnetization vector. It is stronger along a short axis than along a long axis of a magnetic body[43]. In the case of plain magnetic films, the demagnetizing field is always opposite to the perpendicular component of the film magnetization, but vanishes as the magnetization vector stays in-plane, thus equivalent to an in-plane magnetic anisotropy:

$$\vec{H}_d = -4\pi\vec{M}_\perp \qquad \text{(2-15)}$$

Additional shape anisotropy along certain axes within the film plane can also be induced by patterning the MTJ nodes into an elongated shape[19]. Many Co/Fe based alloys are utilized in MTJs with in-plane anisotropy.

Free layers exhibit perpendicular magnetic anisotropy (PMA) when the shape anisotropy is overcome by other types of anisotropy. In most cases, perpendicular magnetic anisotropy arises from either magneto-crystalline anisotropy or interfacial anisotropy. Magneto-crystalline anisotropy is due to the spin-orbit coupling. The electron orbit motion is strongly coupled to the crystal lattice and thus the spin-orbit coupling becomes crystalline anisotropic[43]. Many materials with $L1_0$ structure show crystalline anisotropy perpendicular to the film plane such as FePt and CoPt. On the other hand, interfacial perpendicular anisotropy was predicted due to the lowered symmetry at the

surface or interface by Néel in 1954[44]. Interfacial PMA has been achieved at interfaces of ferromagnetic transitional metals and metal oxides such as MgO and AlO$_x$.

For the STT-MRAM application, materials with PMA showed advantages over in-plane materials in many ways. For free layers with an in-plane/perpendicular anisotropy, H_{eff} are respectively:

$$\boldsymbol{H_{eff} = H_{k\parallel} + 2\pi M_s} \text{ (in-plane material)}$$

$$\boldsymbol{H_{eff} = H_{k\perp} - 4\pi M_s} \text{ (perpendicular material)} \quad \textbf{(2-16)}$$

For both equations, the first term represents the uniaxial in-plane/perpendicular anisotropy with the shape anisotropy excluded. The second term originates from the in-plane shape anisotropy contribution[39, 40].

In in-plane materials, the first term $H_{k\parallel}$ can be introduced using an elongated shape. It is of hundreds of Oe and contributes to the thermal stability. The demagnetizing term $2\pi M_s$ can be as large as 10 kOe and it only adds up J_{c0}. For perpendicular materials, the total anisotropy $H_{k\perp} - 4\pi M_s$, which ranges from several kOe to tens of kOe, determines the thermal stability. Given the same thermal stability, a smaller switching current is thus expected in an MTJ with perpendicular anisotropy. In addition, the thermal energy barrier provided by the elongated cell shape in in-plane MTJ is quite limited. In comparison, the elongated cell shape is not required in perpendicular MTJ. A large thermal barrier can be easily achieved with the large intrinsic anisotropy of the material. The circular shape of a perpendicular MTJ also facilitates the manufacturing process[19].

(iii) Gilbert damping parameter

The Gilbert damping parameter in the damping torque of the LLG equation determines the rate at which the magnetization precession is relaxed. It is believed that

the intrinsic Gilbert damping is induced by phonon and spin-orbit interaction, which transfers energy out of the magnetic system to a thermal bath of phonons and electrons[45]. One of the models proposed by Kamberský indicated that the intrinsic Gilbert damping is proportional to the spin-orbit coupling parameter ξ and the density of states at the Fermi level $D(\varepsilon_F)$ by $\alpha \sim \xi^2 D(\varepsilon_F)$[46]. This model is widely used to explain some damping related phenomena in itinerant ferromagnetic metals and design materials with small damping parameters. On the other hand, in thin films and heterostructures, the nonlocal spin relaxation processes due to spin waves in wave theory (magnons in quantum particle theory) contribute to the damping extrinsically (such as two-magnon scattering process)[45, 47].

(iv) Spin polarization

Large spin polarization is highly desired in the STT-MRAM application both for improving the TMR of MTJs and for reducing the critical current density. From the definition of the spin polarization given previously (equation (**2-2**)), one would expect a high spin polarization in materials that have a large DOS population difference between two channels at the Fermi level. In fact, Heusler alloys trigger significant interest for application in STT-MRAMs due to this property.

2.5   Candidate materials for STT-MRAMs

2.5.1   Diluted CoFeB

As mentioned previously, CoFeB has been dominantly used in MgO-based MTJs with coherent *bcc*(001) oriented CoFeB/MgO interfaces formed after annealing. A composition $Co_{40}Fe_{40}B_{20}$ conventionally used in MTJs gives a magnetization of 1200

emu/cc. Cr has been considered as a promising substitute of Co/Fe in CoFeB to reduce the magnetization and thus the critical current density. Besides, Cr forms a *bcc* structure with a lattice parameter close to CoFeB[48]. Thus the crystal structure of CoFeB would not be affected by incorporating Cr into CoFeB. In fact, it has been shown that the magnetization of CoFeB can be reduced with Cr doping, leading to a reduced the critical switching current density[49, 50]. With a composition of $Co_{40}Fe_{32.7}Cr_{7.3}B_{20}$ J_{c0} was reduced by a factor of four to 4.9×10^5 A/cm^2 compared to MTJs with $Co_{40}Fe_{40}B_{20}$[50].

2.5.2 Heusler alloy Co_2FeAl

The other path to achieve a low critical current density is to adopt ferromagnetic materials with half-metallicity in MTJs. In the half metals, the band structure for the minority spin channel shows a semiconducting/insulating gap at the Fermi level, while it has major conducting bands in the majority spin channel thus inducing a high spin polarization. Half-metallicity in half Heusler alloy NiMnSb ($C1_b$) was first proposed theoretically by R. A. de Groot et al. in 1983[51]. The prediction was experimentally confirmed later on by positron annihilation or inverse photoemission experiments[52, 53]. In 2002, I. Galanakis et al. showed by theory a half-metallic behavior in full Heusler alloys ($L2_1$) based on Co, Fe, Rh and Ru[54]. Among the half metals, Co/Fe-based full Heusler alloys attracted more attention for applications in STT-MRAMs because they have a Curie temperature above room temperature allowing the half metallicity to be practical in STT-MRAMs. Full Heusler alloys with the stoichiometric composition of X_2YZ have a $L2_1$ crystal structure consisting of four fcc sublattices[54, 55]. Within a unit cell, species X occupies sites (0 0 0) and (½ ½ ½), while Y is located at sites (¼ ¼ ¼) and Z is at sites (¾ ¾ ¾). Atomic disordering between Y and Z results in a chemical

ordering degradation from L2$_1$ type to B2 type and the crystal structure further transforms into A2 cells if the atoms X Y Z are totally randomly arranged(Figure 2-16). The chemical ordering can affect the band structure of the Heulser alloys and thus influences other related properties such as the spin polarization and damping parameter[56].
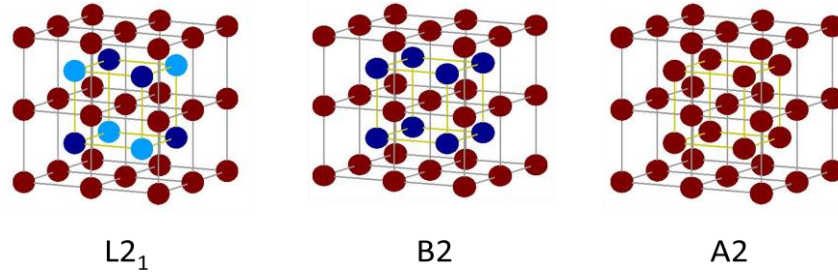
Figure 2-16 Three types of phases in full Heusler alloy associated with the degree of chemical ordering. In L2$_1$ lattice, the red atoms represent species X, the dark blue atoms corresponds to species Y and the light blue ones for species Z.

Full Heusler alloy Co$_2$FeAl is considered as one of the promising candidates for STT-MTJs. It has been shown that by adopting B2-Co$_2$FeAl as the free layer in MTJs, a high tunnel magnetoresistance (TMR) has been achieved around 330%-340% due to its half-metallicity in the Δ_1 symmetry along the [100] direction[57, 58]. An ultra low intrinsic Gilbert damping parameter ~0.001 was reported in this material[59]. In fact, it was indicated that the critical current density was lower in CoFeAl-based spin valves than that of those based on CoFe[60]. A recent study has demonstrated interfacial PMA in Co$_2$FeAl films with reduced thicknesses, indicating the possibility to further reduce J_{c0} by integrating Co$_2$FeAl in perpendicular MTJs[61].

2.5.3   L1$_0$-MnAl

The permanent ferromagnet MnAl with an uniaxial magnetic anisotropy was first reported by Kono in 1958[62], followed by extensive investigations on its structure and magnetic properties[63-69]. The metastable τ phase of MnAl is the only ferromagnetic phase of this binary intermetallic and only forms in a relatively small window of chemical composition close to Mn$_{0.5}$Al$_{0.5}$[64]. Ferromagnetic τ-MnAl has an L1$_0$ structure, which can be reduced to a tetragonally distorted B2 ordered structure with a lattice parameter c ~3.57 Å[63, 70] (Figure 2-17). The chemical ordering between Mn and Al also serves as the origin of the ferromagnetism in τ-MnAl. According to the Bethe-Slater curve, a positive exchange coupling tending to align the Mn moments ferromagnetically was induced between 3d electrons of adjacent Mn atoms at an interatomic distance only above 2.57 Å[62]. With the periodic insertions of Al plane, a high saturation magnetization of 490 emu/cc was achieved in bulk ferromagnetic τ-MnAl along with a large uniaxial magnetocrystalline anisotropy around 10^7 erg/cc[63]. Correspondingly, a perpendicular magnetic anisotropy was demonstrated in τ-MnAl thin films. In previous studies, bulk τ-MnAl was more often than not obtained after a supercooling from the high temperature ε phase (Hexagonal Close Packing) through a eutectoid at ~ 870 ˚C[62, 63]. On the other hand, ferromagnetic MnAl films have been mostly obtained by depositing Al and Mn targets simultaneously or an alloy MnAl target using different techniques, including molecular beam epitaxy (MBE)[65-67], pulsed laser deposition (PLD)[68] and magnetron sputtering[69], accompanied/followed by heat treatments.
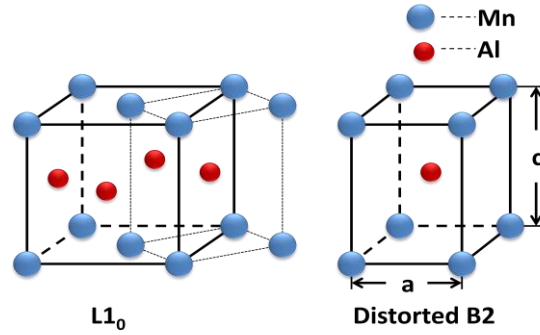
Figure 2-17 L1$_0$ structure of τ-MnAl, which can be reduced into a distorted B2 structure.

Compared to other PMA materials like FePt and CoPt, τ-MnAl does not contain any noble metals, i.e. platinum and palladium and is considered as an attractive candidate due to the lower industrial cost. Besides, it has been noticed that a large damping parameter always appears in popular PMA materials containing noble elements or rare earth elements possibly due to the large spin-orbit interaction[71-73]. However, a recent study indicated a small damping parameter ~0.008 in the manganese alloy Mn-Ga system with a L1$_0$ structure[74]. The small damping parameter is similarly expected in the Mn-Al system considering the similar lattice environment for local spins[74, 75]. Additionally, it is predicted that the crystal structure of τ-MnAl forms in a symmetry that conserves the coherence with the MgO barrier layer thus maintaining a high TMR when employed in MTJs.

3. Experiments

3.1 Synthesis of thin films

3.1.1 Magnetron sputtering system

Magnetron sputtering is one of the most commonly used physical vapor deposition (PVD) approaches for thin film fabrication. It is similar to other simple DC sputtering systems, which initiate sputtering by applying an electric field between the target (cathode metal) and the substrate (anode). Specifically, stray electrons near the cathode are accelerated toward the anode under the electric field. Process gas atoms are ionized while colliding with the electrons. Electrons are accumulated during gas atom ionizations. Meanwhile, as the ions collide with the cathode, the secondary electrons are ejected contributing to the charge multiplication. A discharge finally occurs with a large avalanche current. Stable sputtering is initiated with enough ions starting bombarding the target [76].

Unlike DC sputtering systems, a magnetic field in close proximity of the target surface is employed to achieve a better secondary electron confinement in magnetron sputtering [76, 77]. The magnetic field is roughly parallel with the target surface. The ionization of the gas atoms is greatly improved due to the hopping motion of the trapped electrons in the electric and magnetic fields during sputtering (Figure 3-1).
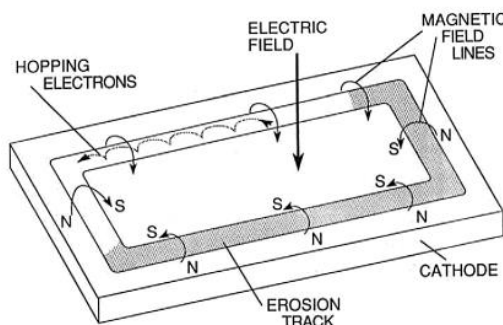
Figure 3-1 The motion of the electrons in a planar magnetron system. (adapted from Ref[76])

Compared to sputtering techniques such as simple DC sputtering, magnetron sputtering operates at a lower process pressure thus avoiding intense gas collisions and scatterings. Therefore a stable plasma and certain growth rate can be maintained with a relatively low target voltage (~500V)[77].

In our magnetron sputtering system, the main process chamber is connected to a cryopump to maintain a base pressure below 1×10^{-6} Torr. The main chamber accommodates four targets, three of which are operated with a RF bias while the fourth one can be operated with both DC and RF bias. Ar is used as the process gas and the process pressure is in the range of a few millitorr. The power of each target can be adjusted to vary the growth rate of the corresponding material or to modify the film composition in a co-sputtering process. The load lock is connected to a turbo pump. During sample loading the load lock can be isolated from the main chamber by a gate valve.

Substrates are mounted on the sample holder using silver paint or heat resistant tape. The sample holder is later fitted into a fork assembly in the load lock. After sealing and pumping down the load lock chamber, the sample holder can be transferred into the main

chamber and attached to the carousel, which allows the substrates to rotate facing down toward the targets. The folk assembly also retrieves the sample holder back to the load lock after deposition.

3.1.2 Ion beam deposition tools

(i) System overview

Ion beam deposition systems demonstrate advantages such as lower process pressure and directional sputtered flux. Reactive Biased Target Ion Beam Deposition (RBTIBD) System was co-designed by University of Virginia and 4Wave Inc. It has an improved performance compared to conventional ion beam deposition systems. RBTIBD allows a low energy ion beam deposition while keeping the overspill contamination minimized [13]. One of the drawbacks of RBTIBD is that it cannot directly sputter oxide targets. This limitation can be overcome by introducing oxygen into sputtering processes.

Similar to our magnetron sputtering system, RBTIBD has a main process chamber connected to a cyropump, maintaining its base pressure below 10^{-8} Torr. A load lock houses a substrate stage assembly, allowing sample loading and retrieving without breaking the main chamber vacuum. A rough pump is used for both primary pumping-down of the chambers and regeneration of the cryopump. Cooling water is provided to both the system and the compressor of the cryopump by a chiller.

(ii) Ion beam source

The key component of RBTIBD is a low energy ion source which combines a hollow cathode electron source (HCES) (cathode) and a Mark II end-Hall ion source (anode)[78]. Figure 3-2 shows the configuration of the ion source. Electrons are emitted from HCES as the gas flows through the cathode tube. The motion of the electrons is

constrained as they enter the magnetic field region surrounding the anode. The electrons keep colliding with the gas flowing though the anode, which leads to ionization of the gas atoms. Both the cathode and anode are connected to power supplies in a range of 0-100V and 0-12A. The power supplies are operated in constant current mode. Two gas lines of Ar are fed into cathode and anode with flow rates in the range of 0-20 sccm and 0-100 sccm respectively to generate a high density of low energy ions (5 eV -50 eV). An additional line of O_2 gas or O_2/Ar mixture with a flow rate of 0-20 sccm can be activated during sputtering for oxide deposition. The process gas pressure during sputtering can be varied from 10^{-4} Torr up to 5 x 10^{-3} Torr depending on the amount of gas fed into the chamber.
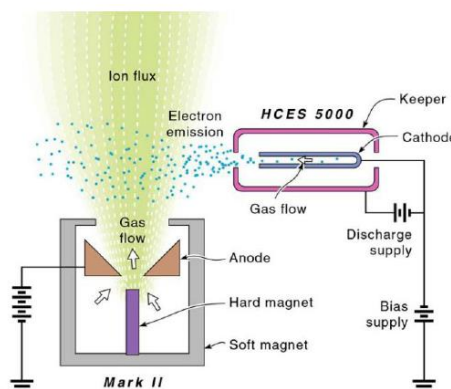
Figure 3-2 Schematics of the low energy ion source equipped in RBTIBD. (adapted from Ref[78])

(iii)   Sputtering via a biased target in the process chamber

Figure 3-3 shows the schematics of the process chamber. Six targets are accommodated in the chamber (only three of them are shown in Figure 3-3). A large negative bias (up to 2 kV) and a small positive one (up to 60 V) are applied alternatively to the target (pulsed DC bias mode). During the negative bias the ions are accelerated

toward the target, inducing sputtering. During a positive bias, no sputtering occurs, but the target poisoning in oxide depositions can be reduced effectively by discharging any dielectric material buildup during the negative bias.
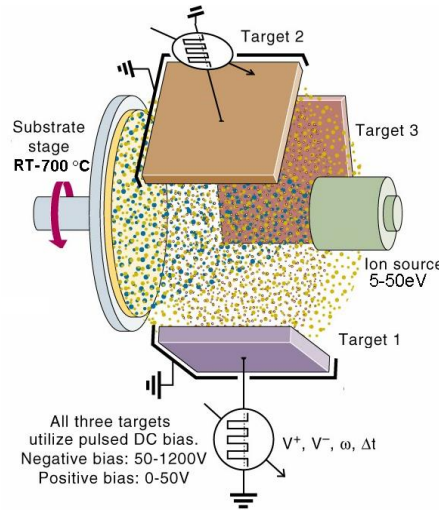
Figure 3-3 Schematics of the RBTIBD process chamber. (adapted from Ref[78])

The pulse width and frequency of the DC bias can be programmed by A Berkley Nucleonics model 565 pulse delay frequency generator. As shown in Figure 3-4, two targets are connected to a pulsar through a relay switch. The pulsars are programmed by the frequency generator through three independent channels. The two-stage target shutter exposes three targets simultaneously (1/3/5 or 2/4/6) to the ion beam but only the biased targets are sputtered. The design of the target shutter allows a co-sputtering of up to three targets. By adjusting the pulse width and frequency, one can fine tune the growth rate of certain target or change the film composition in a co-sputtering process.
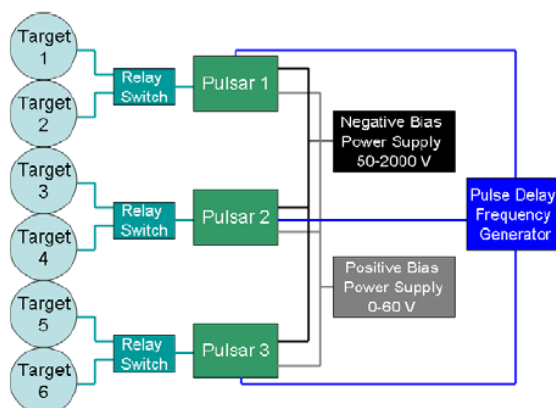
Figure 3-4 Schematics of the pulsed DC bias control. (adapted from Ref[78])

In the fabrication of multilayer samples such as MTJs, the surface roughness and interface mixing can be minimized by tuning factors such as the grow rate and the incident atom energy. Meanwhile, a part of the ion beam will directly bombard the samples on the substrate stage with an un-accelerated low energy (~40 eV), inducing additional interface mixing (Figure 3-2). To minimize this effect, a beam blocker is installed between the anode and the substrate stage, which significantly suppresses the collisions from the overspill ions. Additionally, the growth rate is greatly reduced with the beam blocker in.

(iv) Sample preparation

The sample stage can be heated using a heating lamp positioned behind the stage (Heraeus NobelLight 80mm Omega Emitter). The analog output module sends out a current of 0 to 20 mA. The temperature of the stage can be controlled by a PC through a digital to analog converter (DAC). The set point of DAC ranges from 0 to 35700, corresponding to a stage temperature from room temperature up to 550 ˚C.

Substrates are handled carefully with non-magnetic titanium tweezers before mounted to the wafer carrier. UHP N_2 flow is utilized to remove any particles on the substrates. Ultrasonic cleaning in chemicals is only introduced when necessary (such as visible contamination). The steps are as follows: the substrates are ultrasonic cleaned in an acetone solution for 2 minutes and in an isopropanol solution for another 2 minutes; then they are dried with UHP N_2 and baked on a hotplate at 100 ˚C for 2 minutes. Clean substrates are later mounted to the wafer carrier using silver paint and baked on the hotplate at 100 ˚C for 2 minutes, allowing the silver paint to cure uniformly. The substrate size in my work is ~5 mm x 5 mm. Substrates are mounted within the small center area with a radius ~ 5 mm for a uniform growth rate. In general the growth rate is quite uniform within the whole wafer carrier if the beam blocker is not in use. However it is observed that with the beam blocker, the growth rate could vary radially depending on where the sample is positioned. The degree of the nonuniformity depends on the sputtered species and growth conditions. Figure 3-5 shows the radial thickness distribution of Mg deposited with the beam blocker in. After the sample mounting, the wafer carrier is fixed on the substrate stage assembly. The load lock is sealed and pumped down below 90 millitorr before it is connected to the main chamber.
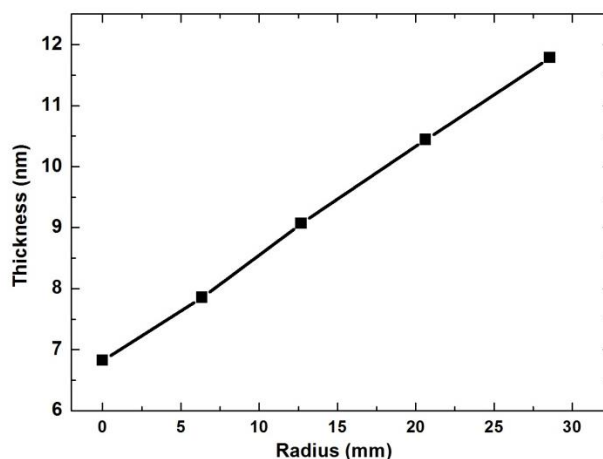
Figure 3-5 Mg thickness distribution under the impact of the beam blocker.

The base pressure is pumped down below 8×10^{-8} Torr before sputtering. The HCES is purged with 10 sccm of UHP Ar gas for 30 minutes and degassed for another 30 minutes before the ion source is turned on. The purpose is to purge and outgas contaminations, mostly O_2 absorbed by the tungsten filament in HCES. After the degassing procedure the ion source can be powered on. The substrates are exposed to the low energy un-accelerated ions for 5 minutes to remove the surface contamination. In particular, MgO substrates are *in-situ* annealed in the main chamber at 500 ˚C for 30 minutes and pre-cleaned for 5 minutes with Argon/Oxygen plasma with an energy of ~35 eV, to remove contaminations such as H_2O and improve the surface crystallinity. Before the film depositions, the desired targets are pre-sputtered with the ion beam to remove any contamination. For the films grown at high temperatures, the current of the stage heater is ramped up at a rate of 5000/minute (DAC). Normally the substrate temperature reaches equilibrium within ~ 45 minutes (Figure 3-6). The film deposition can be performed manually or through the automated recipe control system incorporated in the RBTIBD system. After metal films are deposited, the power on the target and the ion

source is turned off while HCES is purged for another 30 minutes, allowing the filament to cool down in a non-oxygen ambient. In the case of oxide depositions in which oxygen is fed in on purpose, the ion source is kept on for 30 minutes with no oxygen flow. It is then followed by the standard purging process to reduce the risk of oxidation and maximize the filament life time.
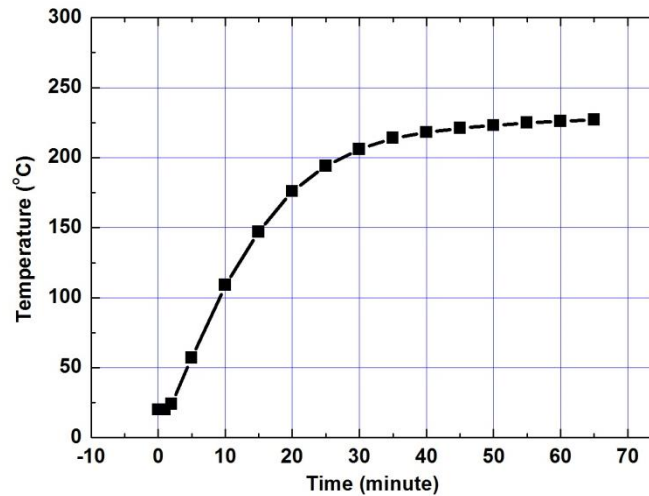
Figure 3-6 Example showing the substrate temperature reaches equilibrium in ~45 minutes. The DAC value is set at 15000.

3.1.3   Annealing process

Post-annealing treatments are used to improve the crystallinity of the thin films in this work. Besides, annealing processes in an external magnetic field are also critical to introduce magnetic anisotropy and establish exchange bias in spintronic devices such as MTJs. Two annealing furnaces equipped with magnets are built in our lab. The first one is a vacuum furnace which can reach a pressure of ~ 10^{-5} Torr. A magnetic field ~ 400 Oe is provided by two permanent magnets. The temperature is ramped up at a rate of 5 ˚C / minute with a PID control and can reach a temperature up to 450 ˚C. The annealing process is usually kept for 1 hour. The other furnace uses forming gas (95% Ar and 5% H_2) to

suppress oxidation during annealing. The magnetic field can be adjusted up to 3000 Oe using an electromagnet. The annealing temperature is ramped up at a higher rate ~ 25 $^{\circ}$C / minute[13]. The real-time temperature can be read out from a thermocouple and the annealing time ranges from several minutes to 1 hour.

The third type of annealing process is rapid thermal annealing (RTA) which allows a much faster heating and cooling process (~20 $^{\circ}$C/s). In the RTA instrument As-One100, an array of infrared lamps ramps up the sample temperature up to over 1000 $^{\circ}$C. Pyrometer or thermal couple is used to monitor and control the temperature. No magnetic field is provided in the RTA instrument. In this work, the RTA process was controlled by a thermocouple in a vacuum ~ 10^{-5} Torr. The annealing temperature ranged from 350 $^{\circ}$C up to 600 $^{\circ}$C with an annealing time from 10 seconds to 300 seconds.

3.2 Thin film characterization

3.2.1 Structure and chemical ordering parameter

The crystal structures in this work are characterized using X-ray diffraction techniques. Using Bragg's law, one can determine the crystal structure and lattice parameters according to the diffraction angles of the Bragg peaks, or predict the positions of the Bragg peaks with knowledge of the crystal structure[79]. Besides, one can determine the chemical ordering type and the degree of certain chemical ordering based on the diffraction patterns, which is important for ordered alloys such as Co_2FeAl and MnAl.

The structure factor F_K describes how the interference of the waves scattered from identical ions affects the intensity of the Bragg peaks in X-ray diffraction[79]. F_K is defined as:

$$F_K = \sum_{j=1}^{n} f_j e^{i\vec{K}\cdot\vec{d_j}} \qquad \text{(3-1)}$$

in which $\vec{d_j}$ represents the scattering position within a cell while f_j is the atomic form factor of the atom at $\vec{d_j}$. The atomic form factor is related to the internal structure of the ion and the incident X-ray wavelength. $\vec{K}$ is the change between the incident and scattered wave vectors, and thus is a reciprocal lattice vector associated with the Miller index of certain lattice plane. According to the lattice symmetry, F_K associated with certain reciprocal lattice vectors could be canceled out and the corresponding diffraction peak is forbidden. By definition, the structure factor F_K for diffraction of lattice plane (khl) in the case of a Co_2FeAl lattice can be written as:

$$F_K = \left(f_{(000)} + f_{(½ ½ ½)}e^{i\pi(k+h+l)}\right) + e^{\frac{i\pi}{2}(k+h+l)}\left(f_{(¼ ¼ ¼)} + f_{(¾ ¾ ¾)}e^{i\pi(k+h+l)}\right) \qquad \text{(3-2)}$$

where $f_{(a\,b\,c)}$ is the atomic form factor for the atom sitting at site *(a b c)*. With the expression of F_K one can predict the diffraction patterns with different types of chemical ordering. Particularly the structure factors of peak (004) and peak (002) are given by:

$$F_{(004)} = \left(f_{(000)} + f_{(½ ½ ½)}\right) + \left(f_{(¼ ¼ ¼)} + f_{(¾ ¾ ¾)}\right) \qquad \text{(3-3)}$$

$$F_{(002)} = \left(f_{(000)} + f_{(½ ½ ½)}\right) - \left(f_{(¼ ¼ ¼)} + f_{(¾ ¾ ¾)}\right) \qquad \text{(3-4)}$$

One can deduce that peak (004) always exists in a crystallized Co_2FeAl lattice regardless of the types of the chemical ordering and thus is known as the fundamental peak. The superlattice peak (002) is forbidden in an A2 lattice because the atomic form factor *f* at each site is averaged out and leads to a vanishing $F_{(002)}$. However, in a B2/L2$_1$ ordered

lattice, the (002) peak is allowed due to the ordering between sites (000)/(½ ½ ½) and (¼ ¼ ¼)/(¾ ¾ ¾), which are occupied by Co and Fe/Al respectively.

On the other hand, the diffraction peak (002) cannot distinguish the B2 type ordering from L2$_1$ type. It gives no information about the extra ordering between Fe and Al sitting at sites (¼ ¼ ¼) and (¾ ¾ ¾). Instead, the structure factor of peak (111) is given by:

$$F_{(111)} = e^{\frac{3i\pi}{2}}\left(f_{(¼¼¼)} - f_{(¾¾¾)}\right) \qquad \text{(3-5)}$$

Therefore it appears only in L2$_1$ ordering phase in which the averaged atomic form factor f is different for sites (¼ ¼ ¼) and (¾ ¾ ¾) [80-82]. Generally when Co$_2$FeAl transforms from A2→B2→L2$_1$, more diffraction peaks appear as the symmetry is broken by introducing chemical ordering into the lattices.

Additionally, the B2 type ordering parameter is defined as[83]:

$$S = \frac{(\sqrt{I_{002}/I_{004}})_{Exp}}{(\sqrt{I_{002}/I_{004}})_{Cal}} \qquad \text{(3-6)}$$

The numerator is the square root of the peak intensities I_{002}/I_{004} obtained experimentally. The denominator is the calculated value for the ideal L2$_1$/B2 structure, which can be estimated in a manner mentioned by K. Barmak et al[84, 85].

$$\left(\frac{I_{002}}{I_{004}}\right)Cal = \frac{F_{(002)}^2 (LPe^{-2M})_{002}}{F_{(004)}^2 (LPe^{-2M})_{004}} \qquad \text{(3-7)}$$

Here L is the Lorenz factor given by $1/(\cos\theta\sin\theta)$ in epitaxial films; P is the polarization factor related to the diffraction angle and XRD set-up; M is the Debye-Waller factor determined by the displacement amplitude and scattering vector.

A Rigaku Smart lab XRD system performed all the structure characterizations of this work. The X-ray source is operated at an accelerating voltage of 44 keV and 40

Amps. Cu Kα radiation is used with a wavelength ~ 1.54 Å. A Ge(2x220) mirror monochromator was used for high resolution X-ray experiments.

3.2.2 Magnetic characterization

The magnetic hysteresis loops were characterized using a Vibrating Sample Magnetometer (VSM). Additionally the magnetic anisotropy between two orthogonal directions can be estimated using the magnetization method[86]. In particular, the perpendicular magnetic anisotropy (PMA) in this work was estimated by characterizing the hysteresis loops in magnetic fields along directions in the film plane and perpendicular to the film plane. Based on the energy consumption to change the magnetization in an applied magnetic field, the total effective anisotropy energy K_{eff} can be calculated by evaluating the area enclosed between the in-plane and perpendicular hysteresis loops[86, 87]. In the cases where magnetic domains are switched coherently with few pinning sites, K_{eff} can be equivalently obtained by [43, 86]:

$$K_{eff} = \frac{H_K M_S}{2} \qquad \text{(3-8)}$$

where the anisotropy field H_K equals to the saturation field along the hard axis. In other cases where a considerable hysteresis is shown, one has to first remove the hysteresis by averaging the hysteresis loop branches and then estimate the enclosed area. Besides, in the PMA case, the total effective magnetic anisotropy energy can be written as:

$$K_{eff} = K_u - 2\pi M_S^2 \qquad \text{(3-9)}$$

K_u is the uniaxial magnetic anisotropy that possibly originates from perpendicular crystalline anisotropy or interfacial anisotropy. $2\pi M_S^2$ represents the in plane shape

anisotropy energy. Thus K_u can be obtained by subtracting the contribution of shape anisotropy $2\pi M_S^2$ from K_{eff}.[88]

The magnetic hysteresis loops are measured using the VSM option in a Physical Properties Measurement System (PPMS) model 6000 (Quantum Design) and Versalab (Quantum Design). Both systems are equipped with a superconducting magnet providing a maximum field up to 70000 Oe for PPMS and 30000 Oe for Versalab. The measurement temperature can be lowered to below 2 K in the PPMS and to 50 K in the Versalab. To avoid any magnetic contamination, the samples were cleaned with acetone and isopropanol, dried using UHP N2 and baked on a hot plate at 100 ˚C for 2 minutes. The samples holders were cleaned with acetone and isopropanol for the same reason. The temperature is kept constant with a slow field sweep rate to maintain isothermal conditions during the measurements.

3.2.3   Gilbert damping constant characterization

One of the most commonly used methods to characterize the Gilbert damping constant is through ferromagnetic resonance (FMR). Ferromagnetic resonance originates from the precession of the magnetization of a ferromagnet body that can be well-described by Landau–Lifshitz–Gilbert equation (equation **2-9**). The precession frequency held by the external field is given as $\omega = \gamma|H_{ex}|$. But it can be better described by Kittel formula in the case of thin films where the impact of anisotropy fields and demagnetizing fields on the precession frequency is taken into account[89]:

$$\boldsymbol{\omega = \gamma\sqrt{(H_{ex} + H_k)(H_{ex} + H_k + \mu_0 M_{eff})}} \quad \text{(3-10)}$$

H_k is the magnetic crystalline anisotropy field, and M_{eff} is the effective magnetization which is the saturation magnetization reduced by surface anisotropy. Parameters γ, H_k and M_{eff} can be obtained by fitting the dependence of ω on H_{ex}. The precession is eventually relaxed due to the damping torque. However, a forced ferromagnetic resonance happens when a RF magnetic field with a frequency same as magnetization precession frequency is applied to the system. With the RF field frequency fixed, an absorption line can be detected during a H_{ex} sweep, indicating a ferromagnetic resonance with which the energy from the RF field is absorbed by the system most effectively. The linewidth ($\Delta \boldsymbol{H_{ex}}$) due to the magnetization relaxation consists of two terms,

$$\Delta \boldsymbol{H_{ex}} = \Delta \boldsymbol{H_0} + \frac{2}{\sqrt{3}} \frac{\alpha}{\gamma} \boldsymbol{\omega} \qquad \text{(3-11)}$$

The first term is the ΔH_0 relaxation that is complicated and not necessarily a constant. One of the examples is the two-magnon scattering process. It is the lowest order magnon coupling process which relaxes the procession by redistributing energy within the magnetic system[45, 90, 91]. The second term arises from the intrinsic Gilbert damping (α) that transforms energy to a thermal bath of phonons or conducting electrons. In the case of a constant ΔH_0, the Gilbert damping parameter can be obtained from the slope of a linear fitting of ω versus ΔH_{ex}.

The FMR measurements for this thesis work were performed by T. Mewes' group at Univeristy of Alabama. The FMR spectra were obtained by a broadband coplanar waveguide field-swept FMR setup, with a frequency limit up to 50 GHz. The details of the setup can be found in Ref. [92].

3.2.4　Spin polarization

The spin polarization was estimated using point contact Andreev reflection (PCAR)[14, 93]. A ballistic Ferromagnetic/Superconductor (F/S) point contact was made to obtain PCAR spectra. With a small voltage applied (smaller than the superconducting gap), electrons with certain spin direction from the ferromagnetic sample are Andreev reflected into holes with the opposite spin direction, accompanied by a cooper pair away into the superconductor carrying the tunnel current. Given the different densities of states in the two spin bands, the conductance of F/S contacts significantly depends on the spin polarization of the ferromagnetic samples (Figure 3-8). Our collaborator Mike Osofsky at NRL carried out all the PCAR measurements and spin polarization estimations. Niobium contacts were made on sample surfaces to acquire the PCAR spectra. The measurements were performed at temperatures between 1.4 K ~ 1.6 K.
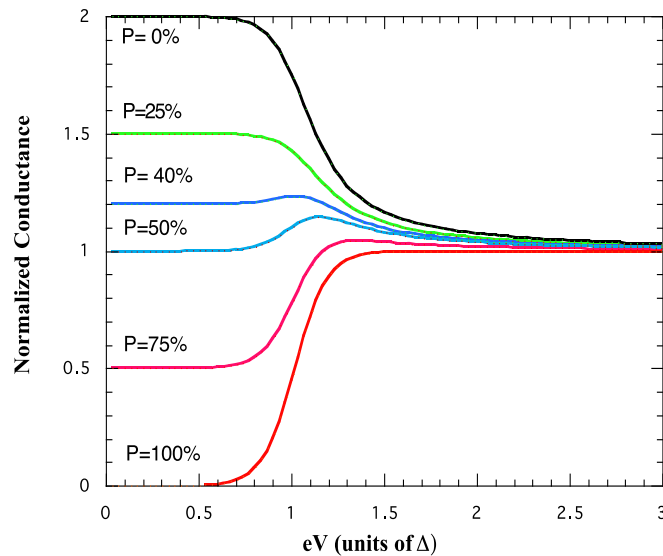
Figure 3-7 The PCAR spectra in samples with different spin polarizations. (adapted from lecture notes for *Spin Transport, Dynamics and Quantum Information*, Prof. Stu Wolf, UVA 2013)

3.2.5 Transport characterization

The *Van der Pauw* method is used to determine the magnetoresistance of spin valves[94]. Four electrical contacts are arranged at the corners of the square shaped samples as shown in Figure 3-7.
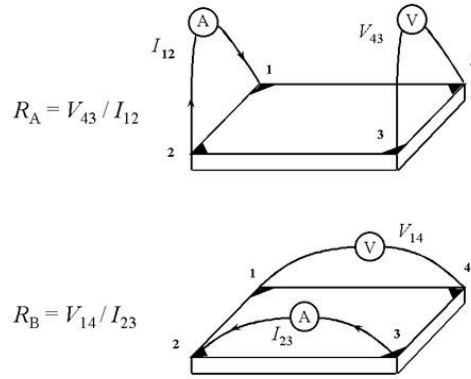
Figure 3-8 Configurations used in the *Van der Pauw* method to determine the sample sheet resistance. (adapted from Ref[95])

By measuring the resistances R_A and R_B in the two symmetric configurations, the sheet resistance R_S of the sample can be determined using equation **3-12**:

$$exp\left(-\pi \frac{R_A}{R_S}\right) + exp\left(-\pi \frac{R_B}{R_S}\right) = 1 \qquad \text{(3-12)}$$

For single layer thin films, the bulk resistance is thus given by $R_S d$, while d represents the film thickness. The indium ohmic contacts on the samples are connected to the channels of a resistivity puck, which can be inserted into the Versalab system. A constant current ~10 mA is applied during measurements. The Versalab system also allows resistance measurements at low temperature with different magnetic field configurations.

3.2.6 Surface roughness

The surface roughness is determined by Atomic force microscopy (AFM). As the silicon tip on a cantilever approaches the proximity of the sample surface, the force between the tip and the sample bends the cantilever. The surface morphology is thus determined by detecting the laser deflection reflected from the cantilever surface. An Asylum Cypher high resolution AFM was used in Topology Air mode (tapping mode) to determine the film roughness in this work.

4. Cr diluted CoFeB

4.1   Introduction

CoFeCrB based MTJs have demonstrated a reduced critical current density due to its diluted magnetization[49, 50]. Besides, the crystallization process of CoFeCrB ribbons has been well studied by our collaborators M. Ding and J. Poon. *α-bcc* crystallization followed by boron segregation was observed at different temperatures depending on the contents of Cr and B. This chapter is aimed at engineering the structural and magnetic properties of CoFeCrB thin films for the STT-MRAM applications by varying the composition and annealing conditions. The same two-stage crystallization process occurs in thin film samples. The impact of Cr concentration on the magnetic properties is investigated. The damping constant of CoFeCrB is also discussed in the last section.

4.2   Sample preparation and Characterization

CoFeCrB films were deposited on thermally oxidized silicon substrates at room temperature using our magnetron sputtering system. Two targets with different compositions ($Co_{43}Fe_{29}Cr_{10}B_{18}$ and $Co_{40}Fe_{18}Cr_{30}B_{12}$) were co-sputtered with different power ratios. The combinatorial sputtering method was used to change the content of Cr. By varying the powers applied to the two targets, the Cr content can be systematically changed from 10% to 30 %, along with a reducing Fe content (Table 4-1).

Table 4-1 Five samples with different CoFeCrB compositions

Sample ID	*Co* content *(%)*	*Fe* content *(%)*	*Cr* content *(%)*	*B* content *(%)*
Cr10	43	29	10	18
Cr16	44.8	24.3	16.1	14.7
Cr20	44.6	21.7	20.8	12.9
Cr22	44.6	20.8	22.1	12.4
Cr30	40	18	30	12

The structure of all the thin film samples was $Si/SiO_2/Ta$ (7nm)/CoFeCrB (30nm)/Ta (7nm). Ta film was used as a seeding layer to improve the surface smoothness and as a capping layer to protect CoFeCrB films from oxidation. The films were annealed at temperatures from 350 ˚C to 450 ˚C in vacuum for one hour.

Chemical compositions were determined using inductively coupled plasma-mass spectroscopy by our collaborator T. Paul Adl from Micron Technology. The crystallization phase was determined using XRD. VSM and FMR techniques are used to characterize the magnetization and the damping parameter of thin films respectively.

4.3   Previous results from CoFeCrB ribbons

$Co_{40}Fe_xCr_yB_z$ ribbons were prepared with *x + y + z = 60* and characterized by our collaborators J. Poon and M. Ding at the University of Virginia. An amorphous structure was observed in as-spun ribbons using both XRD and transmission electron microscope (TEM). The amorphous feature without a long-range crystalline order is due to the high B content, which was also observed in as-spun $Co_{40}Fe_{40}B_{20}$ ribbon samples in previous

studies[96]. The amorphous precursor in CoFeCrB facilitates the formation of a coherent *bcc* (001)-oriented interface with MgO in MTJs.

As the annealing temperature was ramped up, a two-stage crystallization process was observed in as-spun ribbons. Figure 4-1(a) shows the *2θ* scans of $Co_{40}Fe_{32}Cr_{10}B_{18}$ ribbons annealed at 417 ˚C and 508 ˚C respectively. A *bcc* phase with diffraction peaks at 44.95°, 65.56° and 82.94° were observed in samples annealed at 417 ˚C, corresponding to peaks (110), (200), (211). As the annealing temperature increased to 508 ˚C, additional peaks were observed, which could be indexed as the boride-type phase $(FeCo)_3B$[96, 97]. The DSC measurements for the same composition showed a good agreement with the XRD scans (Figure 4-1(b)). For as-spun $Co_{40}Fe_{32}Cr_{10}B_{18}$ ribbons, a primary crystallization of *bcc* occurred at ~ 421 ˚C, followed by the boride phase crystallization at a higher temperature of ~ 518 ˚C.
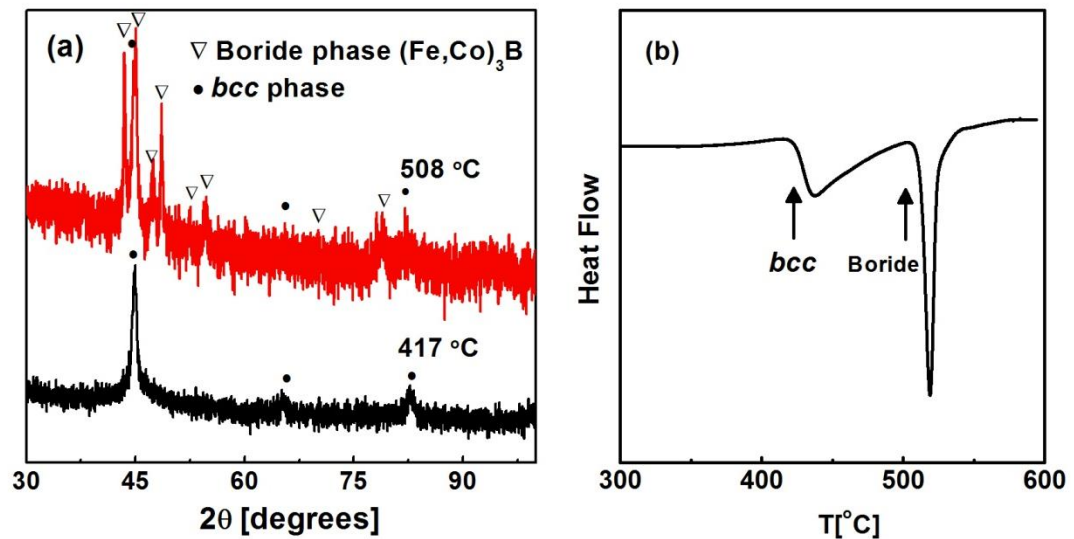
Figure 4-1 (a) *2θ* scans of $Co_{40}Fe_{32}Cr_{10}B_{18}$ ribbons annealed at 417 ˚C(*bcc* phase) and 508 ˚C(boride phases) . (b) DSC curves of $Co_{40}Fe_{32}Cr_{10}B_{18}$ ribbons with the measurement temperature ramped from 50 ˚C to 600 ˚C. Courtesy of Manli Ding et al. (University of Virginia).

Additionally, it is worth noting that in ribbon materials the onset crystallization temperature of *bcc* phase determined by DSC measurements increased from 421 ˚C with 10% of Cr to 456 ˚C with 30% of Cr, indicating that the *bcc* phase formed at higher temperature with an increased Cr content (Table 4-2).

Table 4-2 Two onset crystallization temperatures for samples with different Cr content and B content. Courtesy of Manli Ding et al. (University of Virginia).

Ribbon Composition	Cr content (%)	B content (%)	T_{x1} (˚C) bcc	T_{x2} (˚C) Boride
$Co_{40}Fe_{32}Cr_{10}B_{18}$	10	18	421	518
$Co_{40}Fe_{27}Cr_{16}B_{17}$	16	17	426	541
$Co_{40}Fe_{24}Cr_{22}B_{14}$	22	14	437	560
$Co_{40}Fe_{20}Cr_{30}B_{10}$	30	10	456	573

On the other hand, the crystallization temperature for the boride phases was decreased with an increasing B content. This indicated that with a high B content, the limited solubility of B in the *bcc* phase saturated at a relatively low temperature, and thus promoted the boron segregation. In general a reduced B content is required when increasing the Cr content, to avoid the overlapping of the onset crystallization temperatures for the *bcc* and boride phases.

4.4   CoFeCrB thin films

4.4.1   Structure properties in CoFeCrB films

A similar crystallization process was observed in CoFeCrB films, as in the ribbon materials aforementioned. Figure 4-2 shows the *2θ* scans taken in sample Cr30 annealed at a temperature ranging from 350 ˚C to 450 ˚C. The as-deposited film showed an

amorphous feature, which is desired in MTJ fabrication for the formation of a coherent MgO *bcc* interface. The *bcc* phase emerged from the amorphous matrix at a temperature of 400 ˚C. The peak at around 44.94^o indicated that the *α-bcc* structure in thin films was textured in (110) orientation. The crystallization orientation should depend on the template effect from the Ta seeding and capping layers. As the annealing temperature was raised up to 450 ˚C, a small peak corresponding to a boride-type phase was detected around 42.9^o, which also appeared in the XRD patterns of boride phased ribbon materials. The lattice constant *a* of sample Cr30 was estimated to be ~ 2.86 Å using Bragg's law, which is close to the reported value for CoFeB[96] and FeCr[98]. The mismatch between $Co_{40}Fe_{18}Cr_{30}B_{12}$ and the MgO barrier was ~3.9%, comparable with CoFeB/MgO[96]. A coherent *bcc* structured interface between CoFeCrB and MgO is thus expected when incorporated into a MTJ. It is also worth noting that the two onset crystallization temperatures for *bcc* and boride phases were lowered in thin film samples compared to the ribbon samples with the same composition.
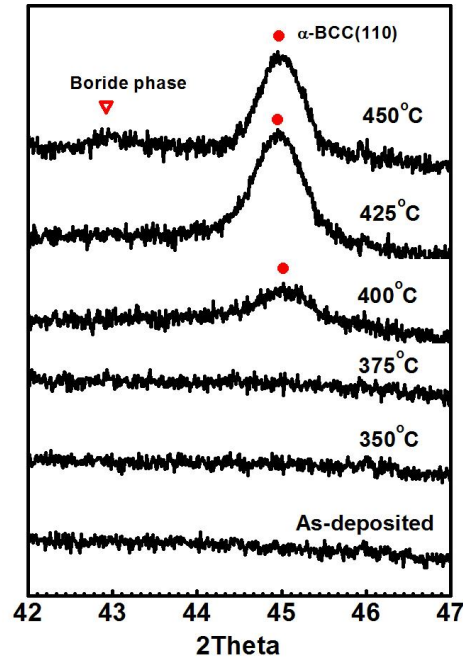
Figure 4-2 *2θ* **scans of Co$_{40}$Fe$_{18}$Cr$_{30}$B$_{12}$ films annealed at a temperature ranging from 350 ˚C to 450 ˚C. Boride phase was observed in the sample annealed at 450 ˚C.**

4.4.2 Impact of Cr content on magnetic properties

The Cr substitution plays the key role in the change of the magnetization. Figure 4-3 shows the impact of Cr content on the film magnetization. For each composition, the magnetization was characterized for both as-deposited films and films annealed at 350 ˚C - 400 ˚C.
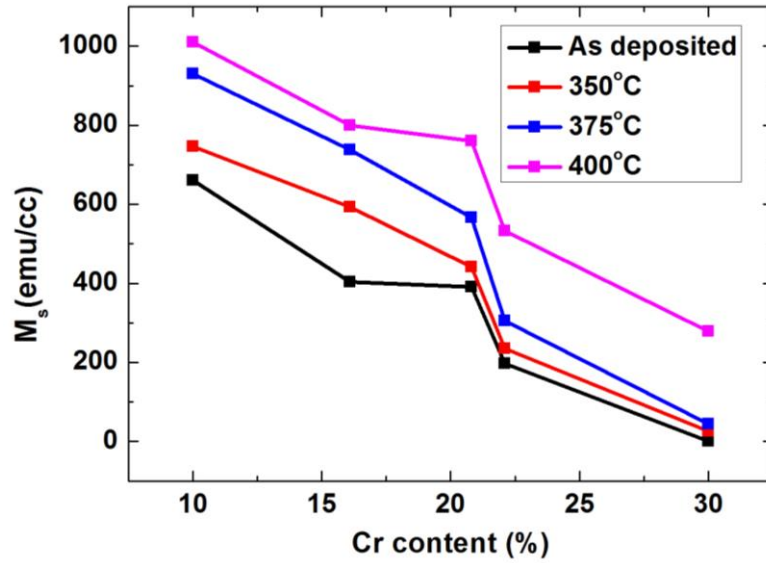
Figure 4-3 Magnetizations of CoFeCrB varied as a function of the Cr content. For each composition, magnetizations were characterized for as-deposited samples and samples annealed at 350 °C - 450 °C.

The magnetization was reduced with an increased Cr content, consistent with previous reports[49, 50]. In as-deposited Cr10 films, the magnetization was ~ 651 emu/cc, which is lower than the value obtained in $Co_{40}Fe_{40}B_{20}$ (1184 emu/cc). As the Cr content was increased to 30%, the magnetization was close to 0 in as-deposited films. The dependence of magnetization on the CoFeCrB composition has been estimated using the generalized Slater-Pauling curve with which one can calculate the magnetization of Co, Fe, Ni based alloys [43, 50, 99]. The main contribution to the magnetic moment is from d electrons, which can be described using the integer magnetic valence of d band Z_m. It is estimated by:

$$Z_m = 2N_d^{\uparrow} - Z \; (N_d^{\uparrow} = 5 \; for \; Co, Fe, Ni \; columns; 0 \; for \; others) \qquad \text{(4-1)}$$

Z is the number of the valence electrons. The average magnetic moment per atom is thus given by:

$$\langle\mu\rangle = \left(Z_m + N_{sp}^{\uparrow}\right)\mu_B \qquad \textbf{(4-2)}$$

$N_{sp}^{\uparrow}$ is the contribution from *sp* electrons which is assumed as a constant. Using Nickel as a standard material, which has a magnetic valence Z_m equal to 0 and an experiment $\langle\mu\rangle \sim$ 0.6 μ_B, one can obtain a $N_{sp}^{\uparrow}$ of 0.6. The magnetic valences of the elements Co, Fe, Cr, and B used in reference [50] were 2, 1, -6, and -3 according to equation **(4-1)**. As shown in Figure 4-4, the generalized Slater-Pauling curve describes well the trend of the magnetization as a function of the Cr content in my study. However, a large divergence was observed between the absolute values of the experiment magnetic moment and the calculated one. For sample Cr30, the calculated magnetic moment per atom is -0.8 μ_B, which also indicates significant shortcomings of the generalized Slater-Pauling curve.
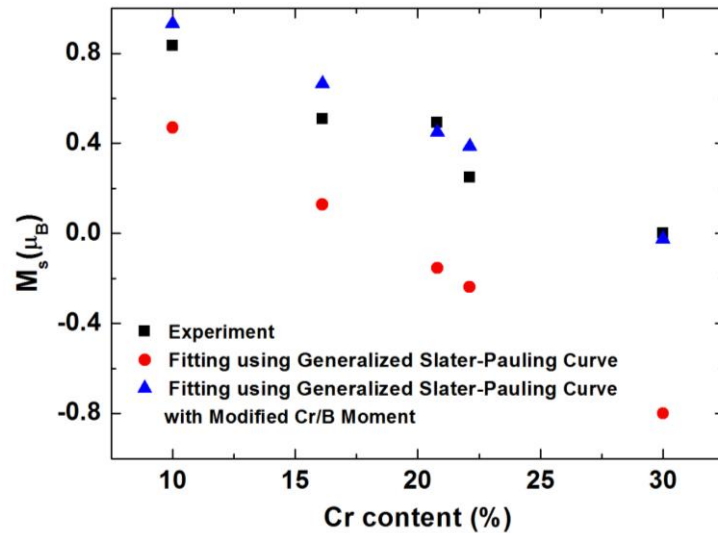
Figure 4-4 Magnetizations of as-deposited films varied with the Cr content. The black squares stand for experiment values, the red dots for the calculated values using the generalized Slater-Pauling curve, and the blue triangles for the calculated values using the same method but with modified magnetic moments for B and Cr.

In fact, the generalized Slater-Pauling curve shows fairly good agreement with experiment for the magnetic moment of elements Fe and Co. But it fails when it comes to certain elements such as metalloids[100]. In the metalloid element B, the contribution from sp electrons $N_{sp}^{\uparrow}$ is much larger than that in $3d$ transition metals. In this study, $Co_{40}Fe_{40}B_{20}$ is used as a standard sample to estimate $N_{sp}^{\uparrow}$ of B. Our ribbon sample $Co_{40}Fe_{40}B_{20}$ gave a magnetization of 1.49 μ_B. Based on this result, an effective $N_{sp}^{\uparrow}$ was obtained around 2.06 for B, larger than the value 0.6 used in the theory. However the value is close to the experimental value (1.85) reported in reference[100]. The average magnetic moment of B is thus -0.94 μ_B. The negative magnetic contribution of B is expected given its diamagnetism due to the electron orbital motion[101].

To improve the fitting, the Cr magnetic moment was tuned down to ~ -3.4 μ_B, corresponding to a magnetic valence -4, instead of -6 as predicted in the curve. The calculated data using the modified magnetic moments for B and Cr atoms were demonstrated in Figure 4-4 in blue triangles, which showed a good agreement with the experiment data. A less drastic magnetic valence of Cr at -5 was also required in reference[50] to better reproduce the experiment magnetization of CoFeCrB films, indicating additional factors such as local magnetic environment have to be taken into account to explain the effective magnetic moment of Cr. One of the speculations is that the antiferromagnetic coupling between Co/Fe atoms is mediated through the Cr. This effect can be equivalently viewed as a negative moment of Cr (or a negative magnetic valence). The much larger magnitude of the Cr magnetic moment compared to that of B also indicated the dominant contribution of Cr to the decrease of the film magnetization.

On the other hand, as shown in Figure 4-3, the saturation magnetization was increased by elevating the annealing temperature. This could be attributed to the B diffusion into the adjacent Ta layers[102]. The smaller size of B atoms led to a more efficient diffusion compared to that of other atoms. The reduction of the B content resulted in an improved film magnetization as observed in CoFeB[102, 103]. To understand the B behavior as a function of the annealing temperature, further investigations using high-resolution TEM are required.

Figure 4-5 demonstrates the change of the coercive field in CoFeCrB films with an increased Cr content. With a Cr content ~ 10%, the coercive field was slightly increased up to ~ 70 Oe as the annealing temperature was elevated. In samples with a 30% Cr content, the enhancement of the coercive field became significant from ~0 to ~519 Oe after annealed at 425 ˚C. The main enhancement of the coercive field cannot be attributed to boron segregation at high annealing temperatures. In the previous study by J. Poon and M. Ding, the boride phase was observed in $Co_{40}Fe_{40}B_{20}$ ribbon samples annealed above 430 ˚C, but the coercive field only increased up to ~40 Oe after annealing at 450 ˚C. Instead the mechanism of the coercive field could be similar to Co-Fe-Cr systems[104-107]. The Kaneko alloy Co-Fe-Cr with Cr ranged from 10% to 40% has a spinodal decomposition from a *α-bcc* solid solution into a two-phase structure, in which the Fe rich α_1-phase clusters were magnetically isolated in Cr rich α_2-phase matrix. The high coercive field could be ascribed to the domain wall pinning effect or incoherent rotation among the α_1-phase clusters[104, 105, 107, 108]. Besides, it is worth noting that the coercive field showed a significant dependence on the annealing temperature. In reference[109], the coercive field of alloy CoFeCrV remained below 80 Oe at 630 ˚C and

was increased to 520 Oe at 650 ˚C. Bright field TEM studies indicated that spherical α_I particles at 630 ˚C evolved into elongated ones at 650 ˚C, and the shape anisotropy contributed to the dramatic increase of H_c[105, 107, 109]. This mechanism could be similarly applied to the Co-Fe-Cr-B system. More TEM characterizations are needed to confirm this speculation.
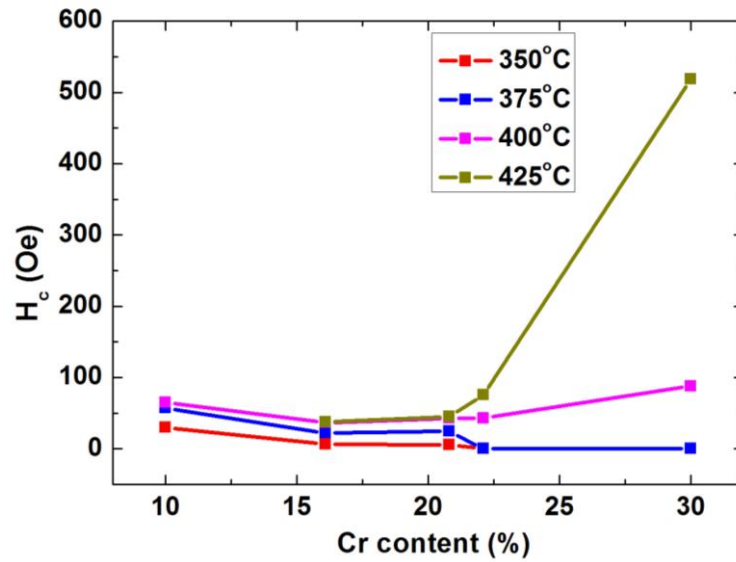
Figure 4-5 Coercive fields of CoFeCrB varied as a function of the Cr content. For each composition, coercive fields were characterized for as-deposited samples and samples annealed at 350 ˚C - 450 ˚C.

4.4.3　Damping parameter characterization

The Gilbert damping parameter was characterized for $Co_{43}Fe_{29}Cr_{10}B_{18}$ films. In as-deposited samples the damping parameter was ~ 0.0085, and it was reduced to 0.006 after annealing at 450 ˚C (no boride phase was detected at this temperature). The value was comparable with the value obtained in $Co_{40}Fe_{20}B_{20}$ films[110, 111]. Besides, it was much lower than previously reported values (~0.02) for $Co_{40}Fe_{40-x}Cr_xB_{20}$ films[50]. It was also

indicated in reference [50] that the damping parameter remained as a constant regardless of the change of the Cr content x in the range of 0 to ~18%.

4.5 Summary

A two-stage crystallization was observed in CoFeCrB ribbons. A *bcc* phase was formed at a relatively low annealing temperature followed by boron segregation at a higher annealing temperature. The onset temperature for the *bcc* phase was raised with a higher Cr content. Besides, as the B content was increased, the limited solubility of B in the *bcc* phase saturated at a lower annealing temperature, leading to a lower onset temperature for the boride phase. A careful control of the composition and annealing temperature is thus required to achieve a pure *α-bcc* phase in CoFeCrB.

A similar crystallization process was observed in CoFeCrB thin films. The magnetic behaviors of CoFeCrB thin films were characterized as a function of the Cr content. The magnetization was significantly reduced as the Cr content increased in the films, that can be well described using the generalized Slater-Pauling curve with modified magnetic moments for B and Cr. Cr substitution also largely enhanced the coercive field of CoFeB. This could be ascribed to the spinodal decomposition of Fe-rich α_1-phase clusters from the Cr-rich α_2-phase matrix. The domain wall-α_1 particle interaction results in a high coercive field. The Gilbert damping parameter was estimated around 0.006 in $Co_{43}Fe_{29}Cr_{10}B_{18}$ films, which is comparable with $Co_{40}Fe_{20}B_{20}$ films.

5. Full Heusler Co$_2$FeAl

5.1   Introduction

The Heusler alloy Co$_2$FeAl has attracted interests for in application to STT-MRAM due to the high spin polarization and low damping parameter[59, 112]. It was also considered as a promising candidate free layer in p-MTJ by inducing PMA at Co$_2$FeAl/MgO interfaces[61]. In this chapter, I describe the epitaxial growth of Co$_2$FeAl films (~50 nm) on MgO(001) substrates using Biased Target Ion Beam Deposition. Growth parameters and post-annealing conditions were optimized to improve the L2$_1$/B2 chemical ordering in samples. The impacts of the chemical ordering were systematically studied on magnetization, Gilbert damping parameter and spin polarization efficiency, which were key parameters for the STT-MRAM application.

Interfacial perpendicular magnetic anisotropy (PMA) was established at the Co$_2$FeAl/MgO interface as the Co$_2$FeAl thickness was reduced. Annealing conditions were carefully adjusted to maximize the interfacial PMA. Concurrently, the reduction in both film thickness and annealing temperature to achieve the interfacial PMA introduces extrinsic factors enhancing the Gilbert damping parameter. Therefore the damping parameters of the perpendicularly magnetized Co$_2$FeAl films were carefully investigated, and were compared to those of Co$_{60}$Fe$_{20}$B$_{20}$ films to evaluate its practical advantage over CoFeB in p-MTJs.

5.2 Development of B2-Co$_2$FeAl

5.2.1 Synthesis of crystallized Co$_2$FeAl films

Co$_2$FeAl films were deposited by sputtering a single Co$_2$FeAl alloy target. The samples had a structure of Co$_2$FeAl(50)/Al(5). An Al film was deposited on top as an oxidation barrier. Three Series were prepared for the growth optimization (see Table 5-1 for details). Series 5-A-1 and 5-A-2 were deposited at ambient temperature without any intentional heating. Post-annealing treatments at 350°C to 450°C for one hour were applied to Series 5-A-1 in the conventional vacuum furnace, while Series 5-A-2 were heated up by RTA in vacuum (~1.5 x 10^{-5} Torr) for 30 seconds, at higher temperatures ranging from 500°C to 650°C. Series 5-A-3 were deposited at elevated temperatures. At the same time, parameters including target bias, cathode/anode currents, processing pressure, etc. were adjusted to improve the crystalline quality. The film compositions were determined by Energy-dispersive X-ray spectroscopy (EDX), which was around 0.493:0.254:0.252 for Co:Fe:Al, close to the expected Heusler ratio. AFM, XRD, VSM, FMR characterization techniques were employed to determine the surface morphology, crystal structure, magnetic hysteresis and damping parameter. The transport spin polarization was determined by PCAR measurements.

Table 5-1 Growth temperatures and annealing conditions for Co$_2$FeAl films.

Series	Sample ID	Substrate Temperature	Post-annealing Temperature
5-A-1	a	No *in-situ* heating	350˚C for 1 hour
	b		400˚C for 1 hour
	c		450˚C for 1 hour
5-A-2	a	No *in-situ* heating	500˚C for 30 seconds
	b		550˚C for 30 seconds
	c		650˚C for 30 seconds
5-A-3	NA	150˚C to 550˚C	NA

5.2.2   Structure and chemical ordering characterization

As aforementioned, a full Heusler alloy has three types of chemical ordering depending on the atomic arrangement. Atomic disordering between Fe and Al results in a crystalline degradation from L2$_1$ ordering to B2 ordering. B2 phase is further transformed into the A2 structure if the atoms are fully randomized. The peak (004) always exists in a crystallized Co$_2$FeAl lattice regardless of the type of chemical ordering thus is known as the fundamental peak. The supperlattice peak (002) is allowed in a B2/L2$_1$ ordered lattice and peak (111) distinguishes L2$_1$ type ordering from B2 ordering[80-82].

To determine the type of chemical ordering, XRD diffraction scans were taken for the Co$_2$FeAl samples. Figure 5-1 shows the typical *2θ* scans for as-deposited films and Series 5-A-2, which were post-annealed at temperatures of 500˚C, 550˚C and 600˚C for 30 seconds respectively(sample 5-A-2-a to 5-A-2-c). The A2 phase was dominant in the as-deposited sample with only a small (002) diffraction peak observed. After annealing treatments the intensity of peak (002) was significantly improved (sample 5-A-2-a to 5-A-2-c), implying the B2 ordered crystal structure formed in Co$_2$FeAl. Peak (002) and

peak (004) were observed at ~31.19^o and ~65.09^o respectively. The lattice parameter is 5.738 Å, consistent with previous reports[80, 113, 114]. The intensity ratios of these two peaks varied as function of the post-annealing temperature, indicating the B2 chemical ordering was enhanced by elevating the annealing temperature.
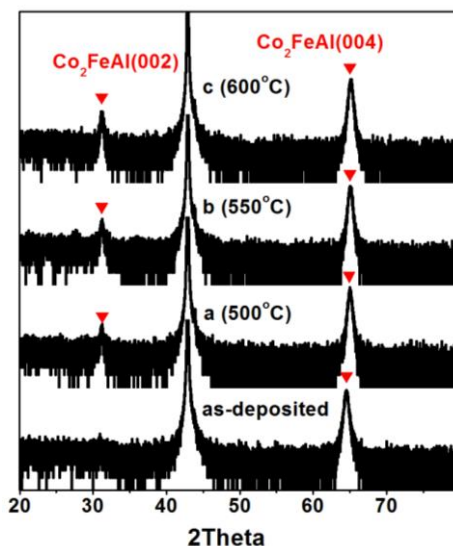
Figure 5-1 *2θ* **scan of the as-deposited Co$_2$FeAl film and Series 5-A-2 annealed at 500°C, 550°C and 600°C, respectively.**

Figure 5-2 showed the in-plane *θ-2θ* scan with χ fixed at 54.7^o and φ at 0° on sample (5-A-2-c), where only diffractions along the Co$_2$FeAl (111) direction would be seen. One would again notice that peak (444) corresponded to the A2 phase, while peak (222) indicated a certain degree of B2 ordering occurred in the film. However, peak (111) was absent due to a lack of the ordering between species Fe and Al, thus the B2 phase was dominant in the Co$_2$FeAl samples instead of the L2$_1$ type.
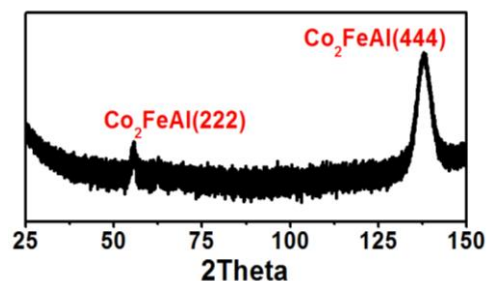
Figure 5-2 In-plane θ-2θ scan with χ fixed at 54.7$^\text{o}$ and φ at 0$^\text{o}$ for sample 5-A-2-c annealed at 600 ˚C for 30 seconds to observe diffractions along Co$_2$FeAl (111).

To investigate the epitaxial growth of the Co$_2$FeAl films on MgO, φ scans (Figure 5-3) were taken with 2θ positioned at 44.65$^\text{o}$ and 62.45$^\text{o}$ corresponding to the Co$_2$FeAl (022) peak and the MgO (022) peak respectively. The offset of 45$^\text{o}$ between the Co$_2$FeAl peak and the MgO peak in φ scans revealed that highly-textured Co$_2$FeAl grew on MgO with (001)$_{Co2FeAl}$// (001)$_{MgO}$ and (110)$_{Co2FeAl}$// (100)$_{MgO}$. The same type of chemical ordering and epitaxial relationship were observed in Series 5-A-1.
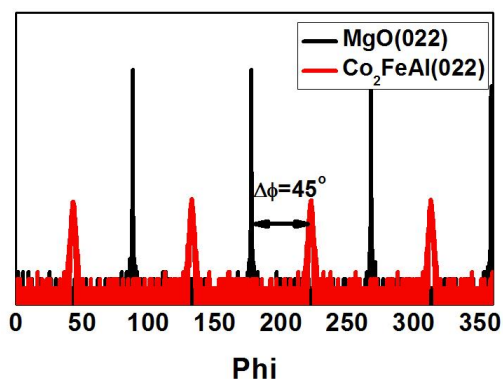
Figure 5-3 φ scans on the same sample with 2θ angle fixed. The red line represents data taken at 2θ of 44.65$^\text{o}$ (Co$_2$FeAl (022) peak) and the black one represents data taken at 62.45$^\text{o}$ (MgO (022) peak).

The B2 chemical ordering was estimated and was plotted as a function of the annealing temperature for Series 5-A-1 and 5-A-2as shown in Figure 5-4. By increasing

the annealing temperature, B2-type ordering was improved and the highest B2 ordering parameter reached ~82.1% in the sample annealed at 600˚C for 30 seconds (5-A-2-c). Annealing treatments at higher temperature ~650˚C led to additional diffraction peaks possibly indicating multi-oriented crystalline Co_2FeAl. It is worth noting that the sample annealed at 450˚C for one hour (5-A-1-c) from Series 5-A-1 gave the same B2 ordering parameter ~66.6%, as the sample annealed at 500˚C for 30 seconds (5-A-2-a) from Series 5-A-2, possibly indicating with an increased annealing temperature the annealing time can be significantly shortened to achieve a highly ordered Co_2FeAl films.
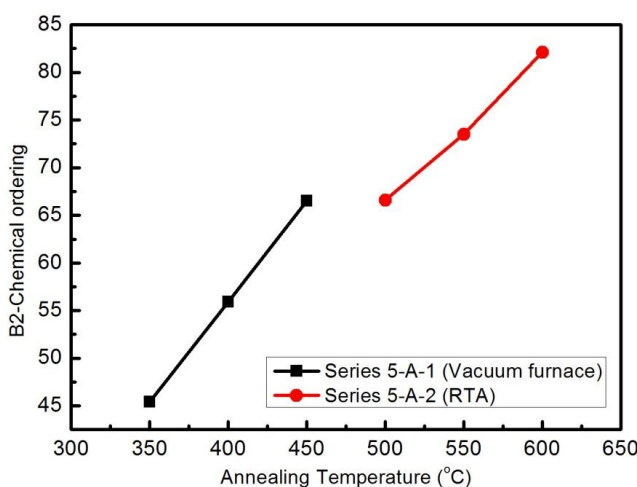
Figure 5-4 B2 ordering parameter as a function of the annealing temperature in Series 5-A-1 (black squares) and 5-A-2 (red circle).

In previous studies $L2_1$ ordering was observed in Co_2FeAl grown at a high temperature around 500˚C [80, 81]. However it was also noticed that Co_2FeAl always tended to form single B2 phase due to the low driving force for an $L2_1$ phase[112]. In this work, Series 5-A-3 grown with intentional heating only showed the B2 chemical ordering. Table 5-2 shows how the growth parameters including growth temperature, target bias, anode/cathode currents, and processing pressure affected the chemical

ordering *S*. At a substrate temperature of 150˚C, *S* remained low regardless of the choice of growth parameters. When the temperature was increased to 500˚C, S was optimized up to 87.06% and even improved to 94.25% as the growth temperature was elevated to 550˚C. On the other hand, it was found the film surface was significantly sacrificed in Series 5-A-3 ranged from 1.5 nm to 7.0 nm depending on the growth parameters. For comparison, the roughness was very small in Series 5-A-1 and 5-A-2 (~ 0.1nm). Film surface smoothness is very important for STT-MTJ stacks. Therefore, the following characterizations were mainly focused on the first two series.

Table 5-2 Effect of the growth parameters on the B2 chemical ordering *S* in Series 5-A-3. The maximum of *S* for each growth temperature was highlighted with font color in red.

Growth temperature (˚C)	Cathode/ Anode Ar flow (sccm)	Cathode/ Anode Current (A)	Negative target bias (V)	*S*
500	10/90	3/2.5	300	72.79
	10/70	7/6.5	300	**87.06**
	10/70	7/6.5	500	77.46
	10/70	7/6.5	900	79.57
550	10/90	3/2.5	300	51.58
	10/70	7/6.5	500	**94.25**
	10/70	7/6.5	900	92.00

5.3   Magnetization, Gilbert damping, spin polarization in Co_2FeAl

5.3.1   Magnetization characterization

VSM measurements were carried out along directions in the film plane and perpendicular to the film plane respectively. A typical hysteresis loop was given in Figure 5-5 for the sample (5-A-1-c), which was post annealed in the conventional vacuum furnace at 450˚C for 1 hour. A dominant in-plane anisotropy was observed in the sample,

thanks to the shape anistropy. The in-plane coercivity field is 40 Oe, and the saturation magnetic moment is ~ 1010 emu/cc which was comparable with the previous reported values[59, 80, 81, 113].
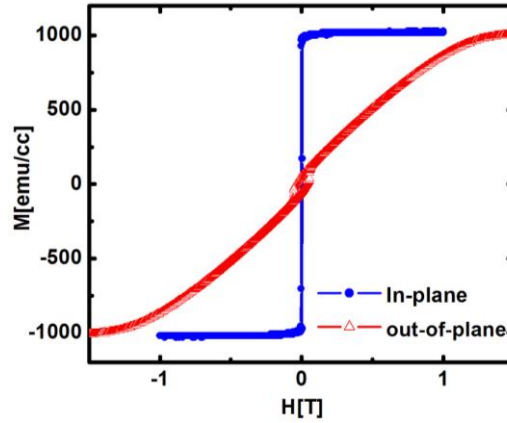
Figure 5-5 Magnetic hysteresis loops for Co$_2$FeAl (50 nm) annealed at 450°C for 1 hour.

The annealing temperature and the chemical ordering have little effect on the magnetization of Co$_2$FeAl films(Figure 5-6). For the annealed samples of Series 5-A-1, the magnetization exhibited a very small reduction by 5% as the annealing temperature increased, although the annealing temperature on the other hand largely improved the chemical ordering from ~45.4% for sample 5-A-1-a to ~66.6% for sample 5-A-1-c. The magnetic moments mostly carried by Co/Fe atoms tend to be aligned similar to the case of CoFeB, therefore little correlation is expected between the film magnetization and the chemical ordering.
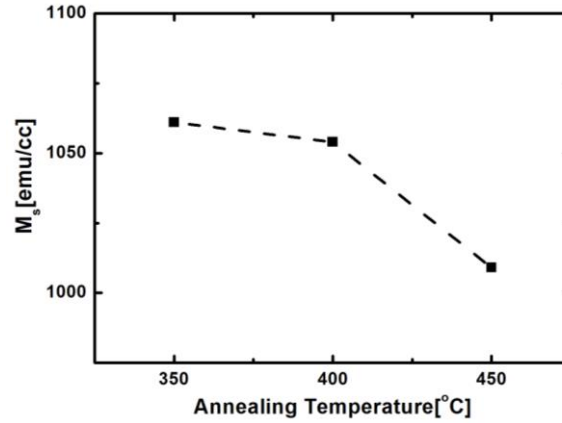
Figure 5-6 Magnetic moment (M_S) vs. the annealing temperature characterized in Series 5-A-1.

5.3.2   Correlation between Gilbert damping parameter and chemical ordering

A low Gilbert damping parameter is one of the attractive properties of Co_2FeAl that has been reported in previous literature[59]. A typical FMR spectrum for the Co_2FeAl samples is shown in Figure 5-7. Two adsorption peaks were observed. The low field mode corresponded to a perpendicular standing spin wave (PSSW) mode, while the high field mode was identified as the FMR signal to determine the damping parameter α.
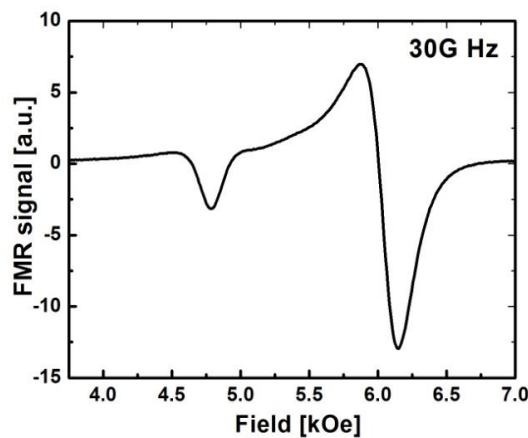
Figure 5-7 In-plane FMR spectrum for sample(a) from Series 5-A-1, annealed at 350 °C for 1 hour. The frequency of the applied AC field was 30G Hz. Courtesy of T. Mewes et al. (University of Alabama).

Figure 5-8 shows a non-linear behavior observed in the linewidth (ΔH) and frequency(f) relationship. This was also reported in a previous study on Co_2FeAl films and was ascribed to the two-magnon scattering effect[59]. Besides, they demonstrated that the two-magnon scattering effect mostly contributed to the non-linear behavior of the linewidth in the low frequency region. But for the high frequency range, the dominant contribution was intrinsic Gilbert damping. Therefore, in the discussion below, the Gilbert damping parameter was estimated by linearly fitting ω verse $ΔH_{ex}$ in the high frequency range. One should notice that the Gilbert damping parameter analysis is under the assumption of two-magnon scattering effect, but it doesn't necessarily exclude other factors leading to the non-linear behavior of the linewidth. For example, the non-linear dependence could be introduced by modes that are not resolvable from the FMR line.
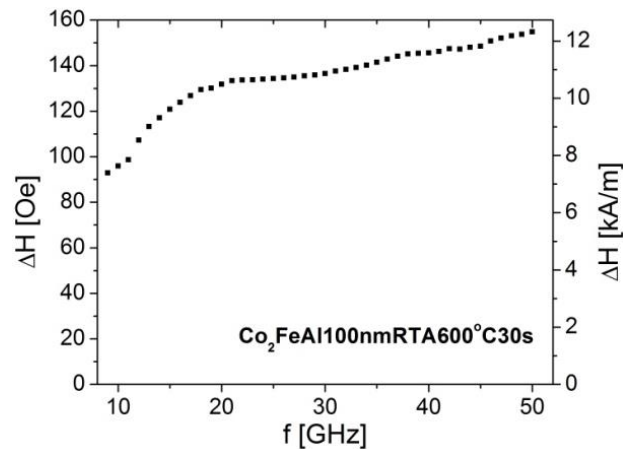
Figure 5-8 Nonlinear dependence of the absorption linewidth on the resonance frequency. Courtesy of T. Mewes et al. (University of Alabama).

The lowest damping parameter among Series 5-A-1 and 5-A-2 was obtained ~0.002 in the sample post-annealed at 600°C for 30 seconds, comparable with the previously reported value[59]. A low damping parameter is generally expected in Heusler alloys by

theory. The Gilbert damping parameter α is simply related to the relaxation frequency G by the formula: $G = \alpha\gamma M_s$. On the other hand, It was indicated by Kamberský's torque-correlation model that G is proportional to the spin-orbit coupling parameter ξ and the density of states (DOS) at the Fermi level $D(\varepsilon_F)$ by $G \sim \xi^2 D(\varepsilon_F)$[46, 59, 115]. According to I. Galanakis, in half-metallic Heusler alloys orbital moments are nearly completely quenched and negligible with respect to the spin moments[116]. Therefore a small spin-orbit coupling parameter ξ is expected. Secondly, the calculated band structure for the minority spin channel shows a semiconducting/insulating gap at the Fermi level for a Heusler structure, as introduced in Chapter 2. Therefore, the $D(\varepsilon_F)$ is minimized compared to other conventional ferromagnetic materials. Low damping parameters were also experimentally achieved in many Heusler alloys such as Co_2MnAl and Co_2MnSi. It was found that Co_2FeAl possessed the lowest damping parameter among these Heusler alloys[117].
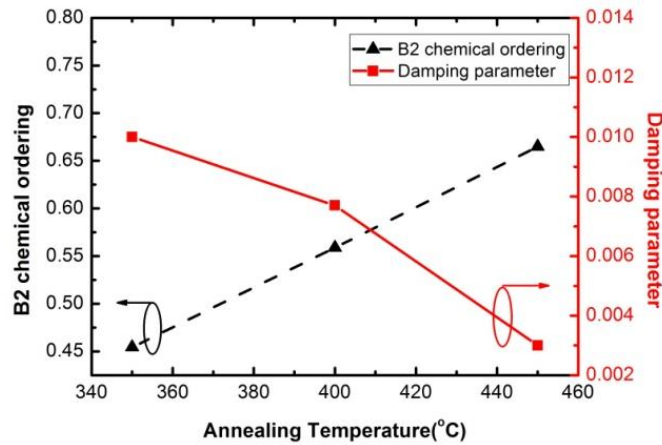
Figure 5-9 Dependences of the damping parameter and the B2 chemical ordering on the annealing temperature observed in Series 5-A-1.

The correlation between Gilbert damping parameter and the B2 chemical order parameter was studied in as-deposited samples and Series 5-A-1. The as-deposited sample yielded no reliable damping parameter due to the lack of uniformity in the film. It was shown in Figure 5-9 that the Gilbert damping parameter was reduced from 0.01 to 0.003 as the annealing temperature increased from 350 ˚C to 450 ˚C, accompanied by an increasing trend of the B2 order parameter. The correlation between Gilbert damping parameter and the chemical order parameter was within expectation theoretically. In reference [59], it was shown as the B2 order parameter deteriorates from 1 to 0, $D(\varepsilon_F)$ was increased by a factor of three due to the A2 disordering, resulting in an elevated damping parameter α. The dependence of the Gilbert damping parameter on $D(\varepsilon_F)$ was also observed in the previous work on Heusler alloy $Co_2Fe_xMn_{1-x}Si$, in which the Gilbert damping parameter varied with Fe concentration x due to the fact that $D(\varepsilon_F)$ was altered by varying x[118] (Figure 5-10).
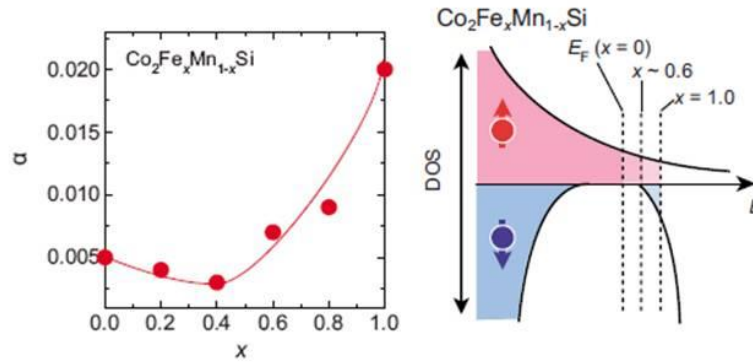
Figure 5-10 Dependence of the damping parameter on Fe concentration x through $D(\varepsilon_F)$. (adapted from Ref [118])

It is worth mentioning that in most Heusler alloys, $D(\varepsilon_F)$ could be also modified as the chemical ordering is improved from $L2_1$ into B2 type thus affecting the damping

parameter. In Heusler alloys such as Co_2CrAl, $D(\varepsilon_F)$ could be significantly changed as B2 phase was transferred into the $L2_1$ phase[56]. By scrutinizing the DOS in Co_2FeAl, one would notice the shape at Fermi level was barely modified as the lattices transform from B2 phase to $L2_1$phase[56](Figure 5-11). Therefore, the B2 phase was sufficient to achieve a low damping parameter for STT-MRAM application. In fact, in my research a low damping parameter has been achieved with no $L2_1$ crystallization. This largely facilitates the manufacturability of Co_2FeAl when integrated in STT-MRAMs. As discussed previously, it is difficult to obtain stable $L2_1$ Heusler phase in Co_2FeAl for which a high growth temperature is required[80, 81]. Instead, single B2-phase could be easily obtained in Co_2FeAl by applying conventional post-annealing treatments without sacrificing the film smoothness as shown in my study and other literature[57, 59, 112], which indicated the possible adoption of Co_2FeAl in STT-MRAMs.
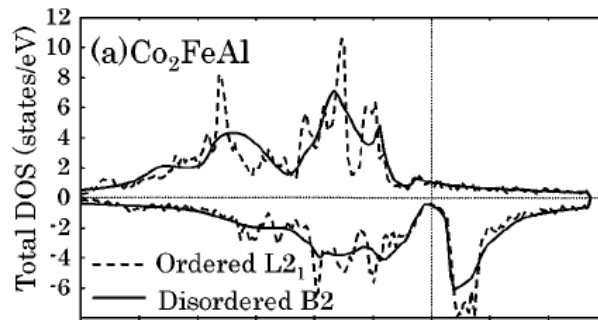
Figure 5-11 The comparison of the DOS for Co_2FeAl in $L2_1$ phase and B2 phase. (adapted from Ref[56])

5.3.3 Correlation between transport spin polarization and chemical ordering

Spin polarization efficiency was predicted ~ 100% in ideal $L2_1$-type Heusler alloys with minority energy gap. However, Co_2FeAl is not considered as an "ideal" half metal.

It was indicated in Ref [56] that the charge transfer from the Co minority spin states to the Fe minority spin states results in the Fe 3d minority conduction band shifting towards the Fermi level and brings in additional states, thus destroying the half metallicity. The theoretical calculation yielded a spin polarization in this compound as low as 30% by KKR method[56] and 38% by SPD method[119].

Experimentally spin polarization can be determined by indirect ways such as estimating the demagnetization time[120], or characterizing the buck scattering parameter based on a two-current model in spin valve/MTJ structures[60]. In my study PCAR spectra were acquired to determine spin polarization efficiency. The results were fit using a modified Blonder–Tinkham–Klapwijk (BTK) model[121] to obtain P and Z, which stand for the polarization and the tunneling parameter characterizing the interface tunneling barrier respectively (Figure 5-12). Plots of P vs. Z for each sample showed virtually no dependence of the polarization on the tunneling parameter. The spin polarization was estimated for each sample in Series 5-A-2 annealed at temperatures from 500˚C to 600˚C for 30 seconds.
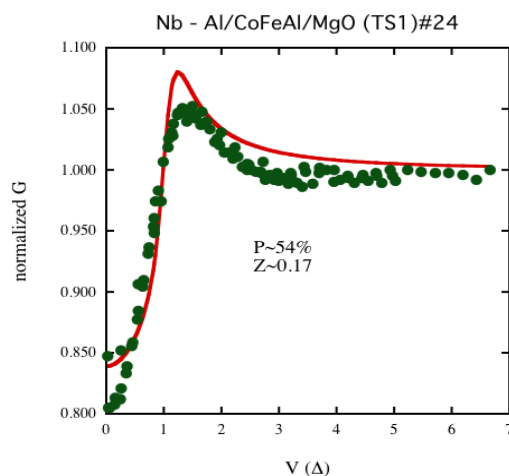
Figure 5-12 Typical PCAR spectra and the BTK fitting of P and Z. Courtesy of M. Osofsky (Naval Research Laboratory)

The spin polarization and B2 chemical ordering were plotted as function of annealing temperatures in Figure 5-13. The typical spin polarization efficiency around 53% in the B2-Co_2FeAl thin films was close to the bulk value ~56% by PCAR measurements[112], higher than the theoretical estimation in references [56] and [119]. Another study on the electronic structure of the compound $Co_2Cr_{1-x}Fe_xAl$ might shed some light on the discrepancy[122]. The authors indicated that although the Fermi level was still close to the bottom of the valence band, the band gap was not fully destroyed. A pseudo band gap of ~0.1 eV was observed in the minority channel of Co_2FeAl. On the other hand, the spin polarization given by PCAR measurements depends not only on the DOS of the majority and minority channels at the Fermi level, but also the Fermi velocities of two channels. The modification from the Fermi velocities could also contribute to the divergence between theoretic and experimental values[123].
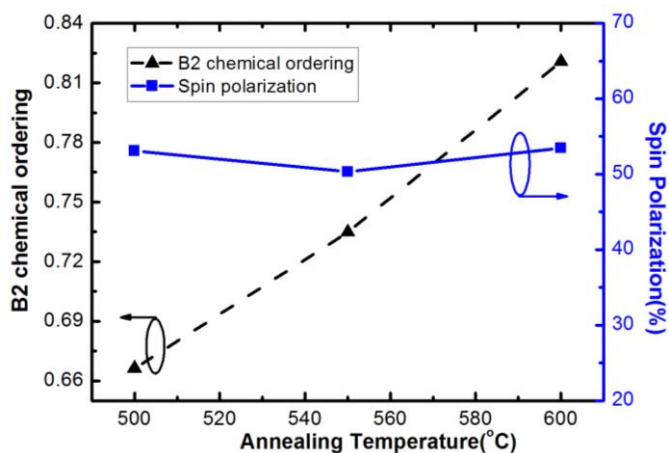
Figure 5-13 Variation of the spin polarization and the B2 chemical ordering as a function of the annealing temperature observed in Series 5-A-2.

Additionally, Figure 5-13 shows the spin polarization was barely affected by the B2 chemical ordering. The ordering parameter was enhanced from 66.6% to 82.1% as annealing temperature was increased from 500˚C to 600˚C, while the spin polarization showed very little response to the change of the chemical ordering. As more A2 disorder occurred in Co_2FeAl lattices, additional minority states at Fermi level were expected thus undermining the spin polarization. However, in my study this dependence appears to be insignificant. The dependence could be compensated by the change of the Fermi velocities or obscured by the extrinsic factors such as film defects and surface modification during the PCAR measurement. The result showed consistency with previous studies on A2-Co_2FeAl and B2-Co_2FeAl based MTJs, in which the TMR value thus the spin polarization was comparable to each other[81, 124]. However, to confirm the impact of B2 disorder on the DOS and Fermi velocity of each channel, and thus on the spin polarization, it is necessary to carry out first principles calculation of the disordered lattice in detail.

The spin polarization is also independent of the $L2_1$ or B2 ordering types according to previous studies. In Ref [56] the *ab initio* calculation suggested that the spin polarization difference between $L2_1$ and B2 crystal types was less than 0.05 in Co_2FeAl. On the other hand, it was reported that the $L2_1$ ordered and B2 ordered Co_2FeAl films gave almost the same spin polarizations ~54% derived from the TMR values in Co_2FeAl-based MTJs[81]. The reason could be partially ascribed to the fact that $D(\varepsilon_F)$ of majority channel and minority channel was not altered as the $L2_1$ ordering transformed into the B2 ordering. In this sense, B2 ordering also satisfied the demand for an optimal spin polarization in Co_2FeAl.

5.4   Interfacial PMA in Co₂FeAl/MgO

5.4.1   Cr seedling layer

A smooth seeding layer was essential in order to induce interfacial PMA in Co$_2$FeAl[61]. Cr is considered as a proper candidate as the seeding layer for Co$_2$FeAl considering the lattice mismatch between the lattice parameters a$_{Cr}$ and a$_{Co2FeAl}$/2 is quite small ~0.7%. On the other hand, the mismatch between a$_{Cr}$ and a$_{MgO}$/√2 is a little larger ~2.8% but can be relaxed as the Cr thickness increases. This section focuses on developing smooth Cr seeding layers on MgO with (100) orientation first.

40 nm of Cr was deposited on MgO substrates at temperatures from 200˚C to 300˚C. The XRD pattern showed that a high crystallinity has been achieved with the growth temperature at 200˚C (Figure 5-14). The peak ~64.25^o was indexed as Cr(002), indicating the epitaxial growth of cubic Cr lattices along MgO (001). A lattice parameter of ~2.89 Å was obtained. The roughness of the surface is only 0.145 nm in a scan range of 1 μm^2 by AFM.
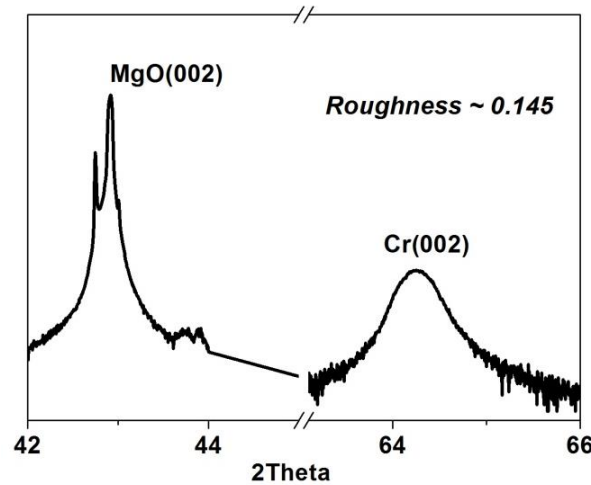
Figure 5-14 *2θ* **scan for MgO/Cr(40 nm) grown at a temperature of 200˚C.**

The dependences of the grain size and the surface smoothness on the growth temperature were characterized, shown in Figure 5-15. The grain size was roughly calculated from the full width at half maximum (FWHM) of the Cr peak using the Scherrer formula[125]. One can see that as the grain size of the Cr layer was slightly improved with an increased temperature, the surface smoothness was significantly sacrificed. Therefore, the growth temperature was selected as 200˚C for the Cr seed layer to establish interfacial PMA in Co_2FeAl.
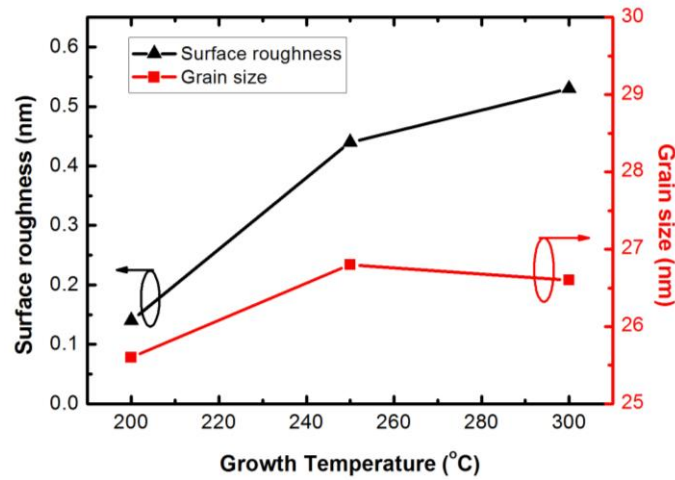
Figure 5-15 Impact of the growth temperature on the crystallinity and the surface smoothness for Cr deposited on MgO(001).

5.4.2 Preparation of perpendicularly magnetized Co_2FeAl

To establish perpendicular magnetic anisotropy (PMA) in Co_2FeAl ultra thin films, stacks of a structure Cr(40)/ $Co_2FeAl(t)$/ Mg(x)/ MgO(2.3-x))/ Ru(5) were deposited on MgO substrates, where t is the nominal thickness of Co_2FeAl (Figure 5-16). MgO was synthesized by sputtering metallic Mg in an oxygen ambient, which is described in

Chapter 7 in detail. To prevent the over-oxidation of Co_2FeAl underneath the MgO layer, a thin protective Mg layer with a thickness of x was inserted before the MgO deposition.
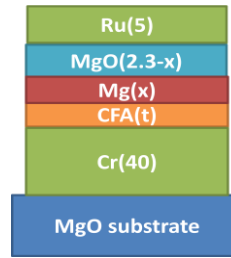
Figure 5-16 Schematics of stacks to achieve perpendicular magnetization in Co₂FeAl.

The Mg thickness x varied from 0 to 1.3nm, accompanied by the thickness change of the MgO layer thus keeping the total thickness at a constant of 2.3 nm. Therefore, the degree of oxidation at the Co_2FeAl/MgO interfaces can be controlled by accurately tuning the parameter x. To investigate the dependence of PMA on annealing conditions, the annealing temperature was changed from 300˚C to 450˚C with the annealing time varied from 10 seconds to 300 seconds. No external magnetic field was applied during annealing treatments. Table 5-3 shows the details about the oxidation and annealing conditions of each sample series.

Table 5-3 Four sample series to exam the dependence of PMA on oxidation and annealing conditions.

Series	Protective Mg thickness	Co₂FeAl thickness t	Annealing treatment
5-B-1	0.7nm	0.57nm~1.90nm	As-deposited
5-B-2	0~1.3nm	0.57nm	As-deposited
5-B-3	0.7nm	0.57nm	As-deposited/350˚C-450˚C
5-B-4	0.7nm	0.57nm	400˚C for 10-300 seconds

5.4.3   Optimization of the interfacial PMA

5.4.3.1   PMA vs. Co$_2$FeAl thickness

In Series 5-B-1, the saturation magnetization M_s was reduced as the thickness was reduced. It implied the existence of a 'magnetically' dead layer, which is inactive magnetically and is likely due to the intermixing occurred at the interface between Co$_2$FeAl and the Cr seeding layer. The thickness of the dead layer t_D and the extrapolated magnetization M_0 for Co$_2$FeAl could be determined by linearly fitting the magnetization per unit area, m_s, as a function of the total thickness t_T [88]:

$$m_s = M_0 \cdot (t_T - t_D) \qquad \text{(5-1)}$$

$$\text{where } m_s = M_s \cdot t_T \qquad \text{(5-2)}$$

Using this method, the dead layer thickness was found around 0.9 nm, while the effective magnetization M_0 of ~731 emu/cc. The nominal film thickness t (hereinafter will be referred to as film thickness) varied from 0.57 nm to 1.90 nm after excluding the dead layer.

Figure 5-17(a) shows the M-H loops of selected samples from Series 5-B-1 measured in a perpendicular magnetic field, indicating the crossover from in-plane anisotropy to perpendicular anisotropy as the thickness was reduced. The interfacial perpendicular anisotropy between a Co/Fe based ferromagnetic layer and a properly oxidized MgO layer has been well-explained using first-principles calculations. As a weak spin-orbit interaction (SOI) is involved, hybridizations within Co/Fe-3d orbits and between Co/Fe-3d and O-2p orbits lift the degeneracy around the Fermi level. The energy

level for out-of-plane orientation of the magnetization is lowered; therefore the interfacial perpendicular anisotropy is switched on[126].
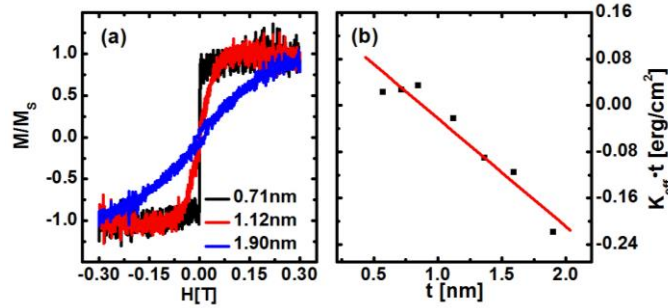
Figure 5-17 (a) Out-of-plane hysteresis loops of the as-deposited Series 5-B-1. The selected film thicknesses are 0.71 nm (black), 1.12 nm (red) and 1.90 nm (blue). (b) Product of total perpendicular anisotropy and thickness ($K_{eff} \cdot t$) vs. the film thickness (t) for Series 5-B-1.

The bulk and the interfacial contribution to the total film anisotropy can be extracted from the phenomenological equation:

$$K_{eff} = K_V + K_S/t \qquad \text{(5-3)}$$

in which K_{eff} stands for the total effective anisotropy that can be estimated using the area method, K_V is the bulk anisotropy, K_s is the surface anisotropy and t represents the film thickness[61, 86]. The total film anisotropy becomes perpendicular as K_s/t exceeds K_v. K_s can be estimated by linearly fitting the relation between $K_{eff} \cdot t$ and t as shown in Figure 5-17(b). In the as-deposited Series 5-B-1 the surface anisotropy K_s was ~0.16 erg/cm^2.

5.4.3.2   PMA vs. MgO oxidation condition

The oxidation condition of the Co_2FeAl/MgO interface plays a significant role for establishing interfacial PMA[126, 127]. Figure 5-18 shows the impact of the protective Mg layer thickness x on the total anisotropy K_{eff} of Series 5-B-2, in which the Co_2FeAl

thickness was fixed at 0.57 nm while the protective Mg thickness x was varied from 1.3 nm to 0. The oxidation condition was optimized with a 0.7 nm thick Mg layer which yielded a maximized interfacial PMA. As x is increased up to 1.3nm, an interface of Co_2FeAl/Mg was expected instead of Co_2FeAl/MgO. For an under-oxidized MgO interface, it has been predicted that orbits $Co/Fe-d_{z2}$ and $O-p_z$ are absent at the Fermi level thus only the energy splitting of $Co/Fe-d_{xz,yz}$ contributed to the interfacial PMA[126]. When x was reduced to 0.4nm, it was suspected that the protective Mg layer has been naturally oxidized and oxygen interacted with Co/Fe atoms forming a Co/Fe oxide at the Co_2FeAl/MgO interface. Excess oxygen atoms induced a local charge redistribution eliminating the energy splitting for orbits $Co/Fe-d_{z2}$ and $O-p_z$ thus suppressing the interfacial PMA[126, 128, 129]. For the sample without the protective Mg layer ($x=0$), no magnetic signal was detected indicating the Co_2FeAl layer was fully oxidized. I will stick with the optimized Mg thickness ~0.7 nm for the following optimization of annealing conditions. But it should be pointed out that the PMA of the over-oxidized samples (x ~0.4 nm) could also be improved with proper annealing treatments, provided that Co/Fe oxides in as-deposited films can be reduced to some extent after heat treatments[129].
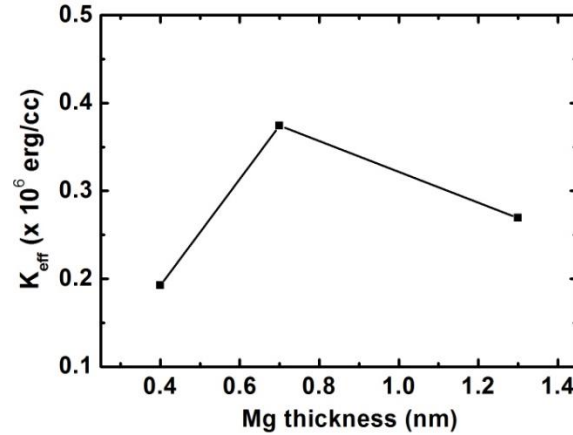
Figure 5-18 Effect of the protective Mg thickness on the total K_{eff} of as-deposited Co$_2$FeAl films.

5.4.3.3   PMA vs. post annealing conditions

The Co$_2$FeAl film thickness was fixed at ~0.57 nm to investigate the impact of the annealing conditions on the total anisotropy K_{eff} (Series 5-B-3). Figure 5-19 shows the dependence of K_{eff} on the annealing temperature. As a baseline, the interfacial PMA was ~ 0.38 x 10^6 erg/cc in as-deposited films, and reached 1.9 x 10^6 erg/cc at a temperature 350˚C, which was consistent with the value for Co$_2$FeAl/MgO reported in Ref [61] and comparable to that of other perpendicular anisotropy systems such as CoFeB/MgO[130] and CoFeGe/MgO[131]. At 450˚C, K_{eff} changed orientation from out-of-plane to in-plane. In the as-deposited sample, both Co$_2$FeAl and MgO layers were likely amorphous so that there was a lack of long range ordering at the interface. In addition, presumably the PMA was suppressed due to the excess Co/Fe oxide at the Co$_2$FeAl/MgO interfaces which has been discussed in detail in last section. After annealing treatments, Co/Fe oxide was likely reduced while the crystallinity was improved at the interfaces leading to an increasing PMA. When the temperature exceeded 350 ˚C, the interfacial PMA started

deteriorating possibly due to the reduction of proper Co/Fe-O bonding at the Co_2FeAl/MgO interfaces[129]. This was also evident in Series 5-B-4 when the impact of annealing time on K_{eff} was studied with the annealing temperature fixed at 400 ˚C. The annealing time of ~10 seconds yielded an interfacial PMA with K_{eff} of 0.8 x 10^6 erg/cc. When the annealing time exceeded 30 seconds, the in-plane magnetic anisotropy exceeded the interfacial PMA.
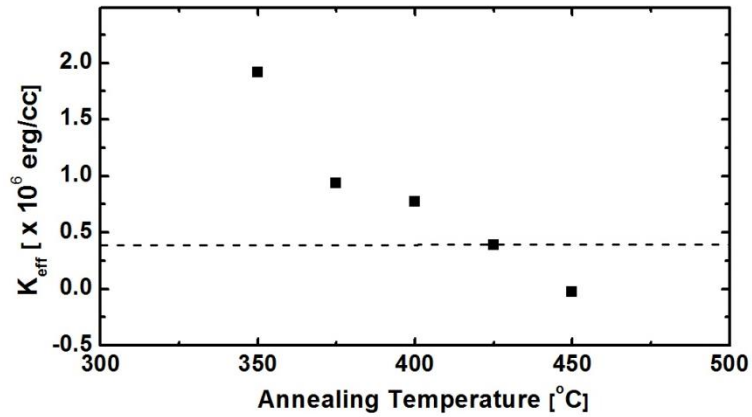
Figure 5-19 Total film anisotropy (K_{eff}) as a function of the annealing temperature in Series 5-B-3 (CFA thickness ~ 0.57 nm). The dash line indicates the value of K_{eff} for the as-deposited film. The magnetic anisotropy is perpendicular to the film plane with a positive K_{eff} while in-plane with a negative one.

5.4.4   Damping parameters of perpendicularly magnetized Co_2FeAl

One should notice that the annealing temperature for STT-MRAMs is still quite limited (below 400 ˚C), compared to the temperature for achieving a low damping parameter (~600 ˚C). Hereby the damping parameters of ultra thin Co_2FeAl annealed between 350 ˚C to 400 ˚C were investigated to estimate the practical advantage of Co_2FeAl for STT-MRAM applications. Figure 5-20 shows the damping parameters for films of Co_2FeAl and $Co_{60}Fe_{20}B_{20}$ after annealing at 350 ˚C and 400 ˚C. The arrow

highlights the Co_2FeAl sample with an interfacial PMA. The damping parameter for the perpendicularly magnetized sample was ~0.012, much higher than the value observed in thick Co_2FeAl films. The increased damping parameter could be attributed to the effects from the decreased thickness and the reduced annealing temperature. With the annealing temperature fixed, the damping parameter was decreased from 0.012 to 0.009 as the Co_2FeAl thickness increased from 1.36 nm to 1.90 nm. A similar trend was also observed in the $Co_{60}Fe_{20}B_{20}$ reference samples in my study. The thickness effect has been reported in CoFeB and Ni-Fe systems previously[111, 130, 132], and it is likely due to the surface structural inhomogeneity[111] or spin pumping effect[133] in the films. On the other hand, the damping parameter decreased from 0.01 to 0.009 as the annealing temperature increased from 350°C to 400°C for films with a thickness ~1.90 nm. The decrease of the damping parameter could be due to the suppression of surface defects and the improvement of the B2 chemical ordering with an elevated annealing temperature as demonstrated in the previous section. A high annealing temperature is generally preferred for lowering the damping parameter. However, the interfacial PMA was only achieved at annealing temperatures below 425 °C. The B2 chemical ordering was sacrificed to some extent, leading to the larger damping parameter. Additionally, an much higher damping parameter ~0.04 has been reported in a structure of MgO(001)/ Cr(40 nm)/ Co_2FeAl(10 nm) through a conventional furnace annealing treatment at 350 °C in Ref[134]. The authors ascribed it to the residual magnetic moments in the Cr and the diffusion of Cr atoms into the Co_2FeAl layer. In my work, the rapid thermal annealing at the same temperature yielded a damping parameter of ~ 0.01 in MgO(001)/ Cr(40 nm)/ Co_2FeAl(1.9 nm)/MgO (2.3 nm), which might suggest that the diffusion of Cr was

significantly reduced likely due to the very short annealing time using RTA (~10 seconds).
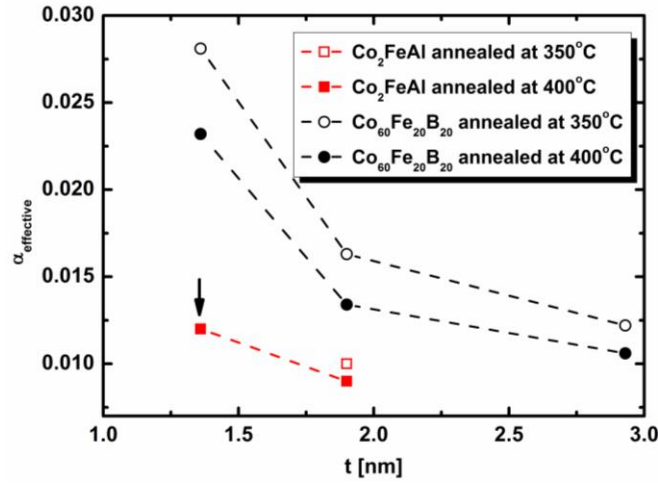
Figure 5-20 Damping parameters of Co₂FeAl and Co₆₀Fe₂₀B₂₀ films as a function of thickness. The open (solid) red squares represent Co₂FeAl films annealed at 350 ˚C (400 ˚C), and the open (solid) black circles represent Co₆₀Fe₂₀B₂₀ annealed at 350 ˚C (400 ˚C). The arrow highlights the Co₂FeAl sample with perpendicular magnetization.

By comparing the damping parameters between Co$_2$FeAl and Co$_{60}$Fe$_{20}$B$_{20}$ samples one should notice that the damping parameter yielded in each Co$_2$FeAl sample was still lower than that of the corresponding Co$_{60}$Fe$_{20}$B$_{20}$ sample with the same stack structure and the same annealing treatment. Thus the Heusler alloy Co$_2$FeAl would still have the advantage of a lower damping parameter than CoFeB, important for lowering the critical current density for spin torque switching. The improvement, however, may be less than expected due to the enhanced absolute value of the damping parameter in thin Co$_2$FeAl films.

5.5 Summary

In this chapter I studied Heusler alloy Co_2FeAl films fabricated by reactive BTIBD. Various growth parameters and post-annealing conditions were tried to improve the chemical ordering in Co_2FeAl films (~50 nm). A dominant B2 ordered phase with no $L2_1$ ordering was achieved via both conventional annealing treatments and RTA treatments. The degree of B2 ordering showed a significant dependence on the annealing temperature. Additionally, I investigated the effect of the B2 ordering parameter on saturation magnetization, Gilbert damping parameter and spin polarization, which are important factors in reducing the critical switching current density in STT-MRAMs. Particularly, $L2_1$ phase was not necessary to achieve a low damping parameter and a high spin polarization. B2 chemical ordering barely affected the magnetization and spin polarization efficiency, but it did play a key role in reducing the Gilbert damping parameter. The Co_2FeAl films annealed at 600 ˚C in RTA indicated an optimized B2 chemical ordering and gave a damping parameter in the level of ~0.002 and a spin polarization ~53% with no $L2_1$ ordering required.

As the Co_2FeAl thickness was reduced, interfacial PMA was established with an optimized MgO interface. The interfacial PMA was maximized via RTA annealing treatments at a temperature ~350 ˚C without the assistance of an external magnetic field. The PMA was comparable to previously reported values for Co_2FeAl/MgO (annealed in a magnetic field) and other systems with interfacial PMA such as CoFeB and CoFeGe. On the other hand, the reduced film thickness and annealing temperature led to an enhanced damping parameter of ~0.012 in the perpendicularly magnetized Co_2FeAl film. The damping parameters of Co_2FeAl films were still lower compared to those of CoFeB films

synthesized in the same fashion. Therefore, Co_2FeAl films still demonstrate the advantage of a low damping parameter over CoFeB for reducing the critical current density in STT-MRAMs, even subjected to a limited annealing temperature. However, in the case of perpendicular STT-MRAM applications, a trade-off between a large interfacial PMA and a low damping constant has to be taken into account carefully.

6. L1$_0$-MnAl

6.1 Introduction

Materials with perpendicular magnetic anisotropy (PMA) have attained much attention due to their applications in p-MTJs[10, 130, 135]. Among PMA materials like FePt and CoPt, ferromagnetic τ-MnAl shows advantages in STT-MRAM applications, which have been discussed in detail in Chapter 2. I introduced interfacial PMA in Co$_2$FeAl/MgO in last chapter. This chapter will highlight τ-MnAl thin films in which a crystalline PMA has been reported previously.

In this chapter, the epitaxial growth of τ phase MnAl thin films was first realized on template substrate MgO (001). Considering the periodically arranged monoatomic Mn and Al planes along the tetragonal c-axis in the L1$_0$ structure of τ-MnAl (Figure 6-1), an alternating Al/Mn quasi-monolayer deposition was developed to enhance the crystallinity of the τ phase, as compared to the co-sputtering of Mn and Al targets. A review of the previous literature indicated that a similar deposition method has been adopted in the first stage of MnAl deposition on GaAs to form a monocrystalline template for subsequent MnAl epitaxial growth[65]. Multilayered Al/Mn films deposited on MgO (001) have also been studied[136-139]. However in the reported structures each Mn or Al layer consisted of multiple atomic-layers (~10 nm) thus hindering the formation of τ phase MnAl. By optimizing the growth parameters, the structure and magnetic properties of the multilayered MnAl films were carefully examined.

The correlation between the lattice mismatch strain and the magnetic properties such as the magnetization and the uniaxial anisotropy has been calculated previously, and it

will be demonstrated experimentally in this chapter. Strain modulation was achieved using two different methods. The first was to modify the strain by changing the film thickness in τ-MnAl films on MgO(001). Secondly the strain was varied by adopting different growth templates including Cr-buffered MgO(001) and GaAs(001).
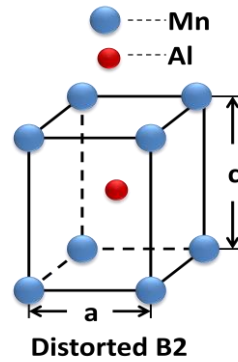
Figure 6-1 Reduced L1$_0$ structure of τ-MnAl with a high chemical ordering.

6.2   Multilayered τ-MnAl films on MgO(001)

6.2.1   Growth parameter optimization

The multilayered deposition of MnAl thin films on MgO(001) was carried out by the automated recipe control program in the BTIBD system. The growth procedure was described briefly in the following. First the targets were simultaneously pre-sputtered for 5 minutes to remove the surface cross-contamination. Before the deposition of each layer, the corresponding target was again lightly pre-cleaned for 5 seconds to remove any possible contamination introduced during the growth. The sequence for the bilayer deposition started from the Al layer due to its uniform nucleation forming a smooth seeding surface for the subsequent layers. To be Specific, the Al target was first pre-cleaned for 5 seconds, which also allowed the deposition variables to stabilize. Later on

the substrate was exposed to Al sputtering for a time of *s* seconds. After the deposition of Al, the ion source was set to the idle state for 5 seconds to avoid the residual deposition. The subsequent Mn layer followed exactly the same steps, and made a full run of one Al/Mn bilayer deposition. A full multilayer deposition was composed of *N* repeats of Al/Mn bilayer deposition. The diagram of the multilayer structure is shown in Figure 6-2. The variable *s* can be easily edited in the recipe to adjust the bilayer thickness *t* thus finely optimizing the film quality. All the multilayered samples had a typical structure of $[(Al/Mn)(t)]_N/Ta(7)$. The tantalum layer was deposited as the capping layer to protect the MnAl films from oxidation. To optimize the growth parameters, the number of repeats *N* was first fixed at 18. The bilayer thickness *t* changed from 4.5 Å to 6.4 Å when the deposition time *s* for single layers of Al and Mn varied simultaneously from 8 seconds to 12 seconds (Series 6-A-1). On the other hand, the bilayer thickness was fixed at 5.7 Å and *in-situ* heating during MnAl deposition was applied tending to improve the film crystallization (Series 6-A-2). All the MnAl samples were further treated with rapid thermal annealing in vacuum at 400 ˚C for 12 seconds. The details of the two sample series were summarized in Table 6-1. The sample composition was determined by Rutherford backscattering spectroscopy (RBS). AFM, XRD, VSM, FMR techniques were used for the thin film characterizations.
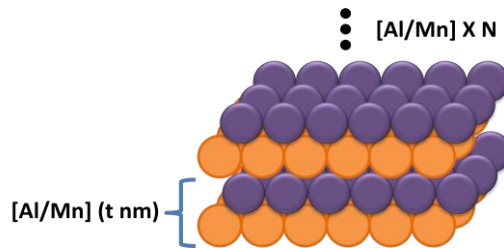
Figure 6-2 Diagram of the multilayer structure of MnAl

Table 6-1 Bilayer thickness and growth temperature were changed to optimize the multilayered growth recipe.

Series	Substrate Temperature	Bilayer thickness t
6-A-1	No *in-situ* heating	4.5 Å
		5.2 Å
		5.7 Å
		6.4 Å
6-A-2	No *in-situ* heating	5.7 Å
	51˚C	
	70˚C	
	100˚C	

(i)   Bilayer thickness optimization

Al/Mn bilayer thickness t determined the volume fraction of τ phase crystallization thus the film magnetization, given the fact that τ phase is the only ferromagnetic phase in MnAl. The first strategy in developing multilayer deposition was to tune t to maximize the film magnetization and map out the degree of the τ phase crystallization (Series 6-A-1). Figure 6-3 plots the film saturation moment M_s as a function of t. All the samples were treated with RTA at 400 ˚C for 12 seconds. The repetition number N was fixed at 18 since the effective crystallization of the τ phase MnAl mostly appeared near the interfaces between the Al and Mn layers. The saturation magnetization showed a maximum at $t \sim$ 5.7 Å, indicating the volume fraction of τ-MnAl has reached the maximum. When the bilayer thickness was smaller than 5.7 Å, the layers of Al (or Mn) nucleated discontinuously leading to the excess intermixing of Mn and Al atoms, which undermined the chemical ordering thus the ferromagnetism. On the other hand, for the films with the bilayer thickness above 5.7 Å, the crystallization of τ phase was not able to occur through the entire bilayer, leaving some fraction of non-magnetic phases such as nanocrystalline γ_2-MnAl and α/β-Mn[64, 136] (which was not observed in XRD) or an

amorphous phase. The optimized saturation magnetization was achieved by minimizing the Al/Mn intermixing and maximizing the volume fraction of τ phase at the given annealing conditions.
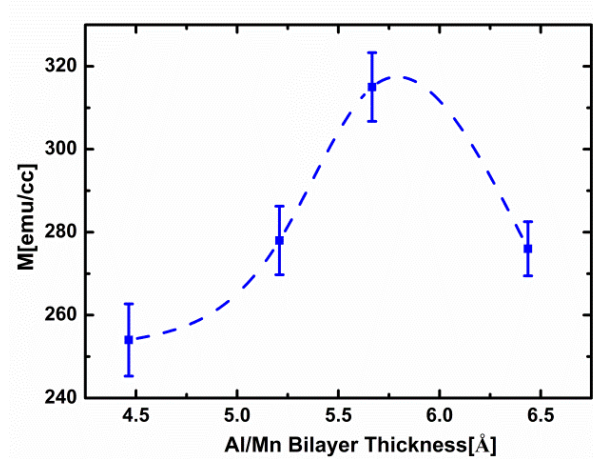
Figure 6-3 Variation of film magnetization on Al/Mn bilayer thickness *t* (Series 6-A-1). The dash line is added to guide the eye.

(ii) Growth temperature optimization

With the Al/Mn bilayer thickness fixed at the optimized value 5.7 Å, the growth temperature was slowly raised from room temperature to 100˚C (Series 6-A-2). The curve in Figure 6-4 shows the dependence of film magnetization on the growth temperature. Again, the samples were thermally treated with the same annealing conditions. The intentional heating during the growth failed to improve the film quality but induced a destructive effect on the film magnetization and concomitantly on the τ phase crystallization. At 100 ˚C, the magnetization was close to zero implying the growth temperature has passed the optimization window for τ phase formation.
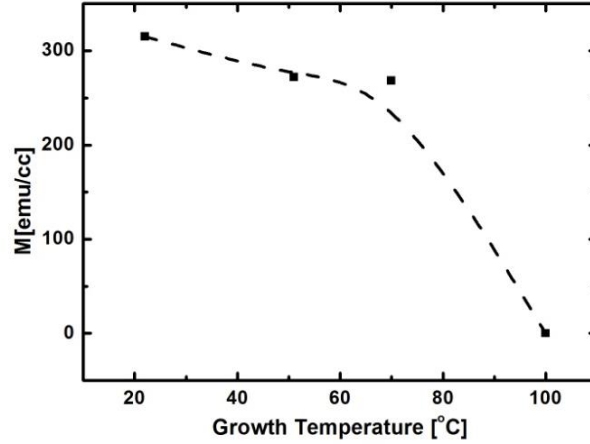
Figure 6-4 Variation of film magnetization on the growth temperature (Series 6-A-2). The dash line is added to guide the eye.

6.2.2 Epitaxy of MnAl films on MgO(001)

Compositional analysis for the sample grown with optimized parameters [(Al/Mn)(5.7 Å)]$_{18}$ indicated the Mn atomic percentage was 50.6%, which fell in the window of τ phase MnAl (50%-60%) in the Mn-Al phase diagram[64]. The AFM measurements also showed a smooth sample surface with a roughness ~ 0.2 nm. Figure 6-5(a) shows the *2θ* scan obtained from the same sample after the post annealing treatment (the total thickness ~10.2 nm). The strongest peak at ~42.9^o was due to the diffraction of (002)$_{MgO}$ planes. Two small diffraction peaks were observed around 29.78^o and 61.97^o in the *2θ* scan, which corresponded to (001)$_{\tau\text{-MnAl}}$ and (002)$_{\tau\text{-MnAl}}$ planes. This suggested that the τ phase was formed after annealing. The appearance of the fundamental (002) peak implied the presence of the tetragonal body centered lattice in the film, regardless of the chemical arrangement of Mn and Al. The superlattice (001) peak revealed the high B2 chemical ordering between Mn and Al planes along the *c*-axis. To

investigate the in-plane epitaxial relationship between τ phase MnAl and MgO, φ scans were performed with 2θ positions corresponding to the τ-MnAl (011) peak at 42.37° and the MgO (022) peak at 62.45°. The results are shown in Figure 6-5(b). The four τ-MnAl (011) peaks were due to the four-fold symmetry along the c-axis of MnAl, which also applied to the MgO (022) peaks. A separation of 45° between the τ-MnAl (011) peak and the MgO (022) peak was present, caused by an in-plane 45° orientation offset between the $(001)_{\tau\text{-MnAl}}$ and $(002)_{\text{MgO}}$ planes, which followed the same matching stratergy between Fe and MgO[23], and has also been observed previously in Co_2FeAl films deposited on MgO. Based on the XRD results, MnAl films grew epitaxially on the MgO(001) substrate with the orientation of the planes $(001)_{\tau\text{-MnAl}}//(001)_{\text{MgO}}$ and $(110)_{\tau\text{-MnAl}}//(100)_{\text{MgO}}$. From the 2θ values of the τ-MnAl (001) and (011) peaks, one can use Bragg's Law to calculate lattice constants a=3.02 Å (in plane) and c=3.00 Å (out of plane) with c/a ~1, which suggested a very small tetragonal distortion in comparison with bulk τ-MnAl[63] (a = 2.77 Å and c = 3.57 Å with c/a ~1.3). The reduced distortion ratio c/a was within our expectation. The lattice mismatch (~6.7 %) between the τ-MnAl lattice and MgO lattice caused a very large tensile strain in the 10 nm thick MnAl film due to the coherent interface. On the other hand, the in-plane tensile strain of the τ-MnAl lattice resulted in a reduced c from 3.57 Å to 3.00 Å due to the Poisson effect.
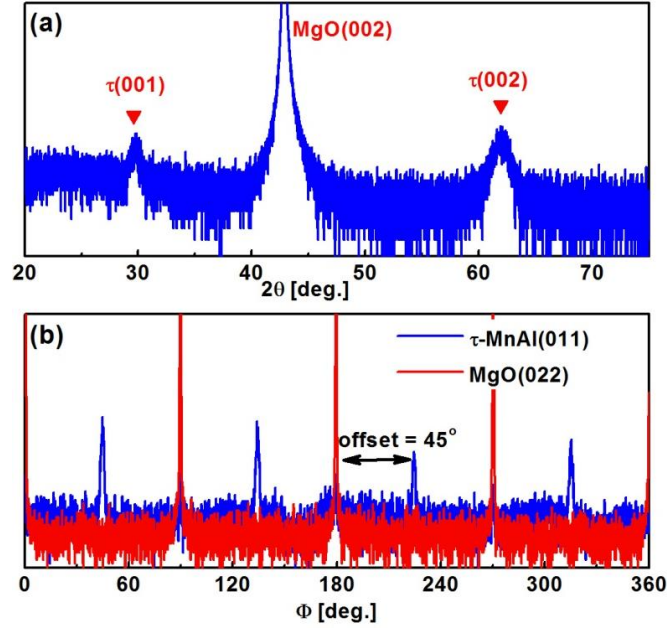
Figure 6-5 (a) *2θ* **scan of sample [Al/Mn(5.7 Å)]₁₈ on MgO(001). (b) 360° *φ* scans on the same sample. The blue line represents data taken at *2θ* of 42.37° (*τ*-MnAl (011) peak) and the red one represents data taken at 62.45° (MgO (022) peak).**

6.2.3   Magnetic properties of MnAl films on MgO(001)

The room temperature hysteresis loops measured along MgO [100] and [001] directions are shown in Figure 6-6. Due to the epitaxial growth of the *τ* phase MnAl with an in-plane 45° orientation offset between the (001)$_{τ\text{-MnAl}}$ and (002)$_{MgO}$ planes, the magnetic field for in-plane measurements was equivalently applied along *τ*-MnAl [110]. To compare the multilayerd growth method to the co-sputtering approach, a sample with the same structure MgO/MnAl(10)/Ta(7) was fabricated using the optimized co-sputtering recipe developed previously[13]. One should notice that the co-sputtered sample had the same composition according to Ref [13]. After the same annealing

treatment, the multilayered sample demonstrated a saturation magnetization ~ 394 emu/cc, twice as much as the moment obtained in the co-sputtered one (~174 emu/cc).
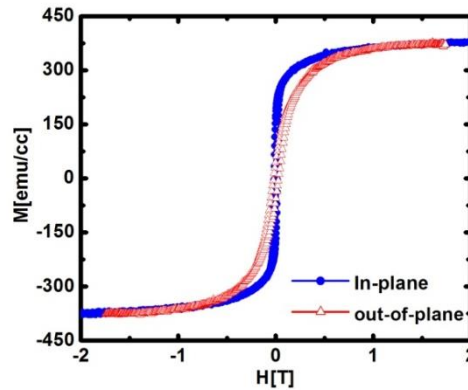
Figure 6-6 In-plane (blue) and out-of-plane (red) hysteresis loops of the [Al/Mn(5.7 Å)]$_{18}$ sample.

On the other hand, the film magnetization was lower than the bulk value (~ 490 emu/cc). The lower magnetization in MnAl could be attributed to point and plane defects in films such as antiphase boundaries (APBs)[67]. However, it should be pointed out that the lattice strain plays a critical role impacting the magnetic properties. A change in the tetragonal lattice distortion ratio could contribute to the lower magnetization. Bulk MnAl has a high tetragonal lattice distortion with a *c/a* ratio ~ 1.3, while MnAl films grown on MgO(001) exhibits a structure close to a B2 cube (*c/a*~1). Based on a calculation of the spin-polarized density of states in MnAl[70, 140], the DOS of the minority spins near the Fermi level is higher when the lattice transforms from the L1$_0$ structure to a B2 cubic structure, resulting in a decreased magnetization. Thirdly, a detailed analysis of the thickness dependence of the magnetization revealed that the reduced saturation moment could be partially due to a 'dead layer', i.e. non-ferromagnetic interfacial layer between the MnAl and the Ta capping layer; it is discussed in section **6.2.5**.

Unlike most of the previous reports on MnAl films showing a perpendicular anisotropy[65-68], the hysteresis loops suggested a magnetic anisotropy lying in plane. This was also ascribed to the lattice strains from the MgO template, which is discussed in detail in the section **6.2.5**.

6.2.4 Gilbert damping parameter

Previous studies have indicated experimentally large damping parameter in ferromagnets containing noble elements ($\alpha_{FePt} \sim 0.055$, $\alpha_{CoPd} \sim 0.045$) [71, 72] and rare earth elements ($\alpha_{FeTb} \sim 0.11$)[73]. Recently, a small damping parameter in a range of 0.0053-0.015 was reported in $L1_0$ MnGa films[74]. As pointed out in previous chapters the macroscopic spin damping α originates from the spin-orbit interaction and can be depicted quantitatively by the dependence $\alpha \sim \xi^2 D(\varepsilon_F)$. A large spin-orbit coupling parameter ξ was generally expected in noble elements or rare elements. However in manganese based alloys the calculated spin-orbit coupling parameter for Mn d orbitals was $\sim$ 40 meV, as small as those for the other 3d elements thus favorable for the low α[74]. In my study, the damping parameter α of the multilayered MnAl with a total thickness $\sim$10.2 nm was obtained around 0.033, based on the fitting of the linewidth of the resonance field verses the resonance frequency (Figure 6-7). It is smaller than those of Pt/Pd based or rare earth element based ferromagnets, but higher than that reported in $L1_0$-MnGa films. One should notice that the dynamic damping of $L1_0$-MnGa films in Ref[74] was determined by an all-optical pump-probe setup, in which the time-resolved Kerr signals directly depict the precession of local spins; the FMR used in my study is considered as a nonlocal technique which indirectly obtains information on damping from the broadening of the absorption lines and thus possibly includes some extrinsic

effects[141]. The authors of Ref[74] also theoretically demonstrated the correlation between α and the density of states at the Fermi level $D(\varepsilon_F)$, analogous to Heusler alloys discussed in last chapter. Therefore a detailed calculation of $D(\varepsilon_F)$ is required to make a reasonable comparison between the intrinsic damping parameters of L1$_0$-MnAl and L1$_0$-MnGa.
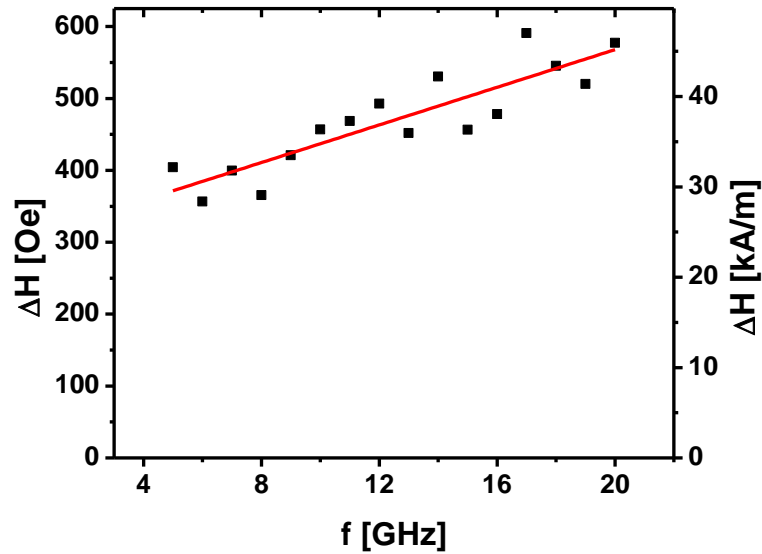
Figure 6-7 Dependence of the absorption linewidth on resonance frequency in the [Al/Mn(5.7 Å)]$_{18}$ sample, for the Gilbert damping parameter estimation (red linear fitting).

6.2.5   Thickness dependent anisotropy

The thickness series was fabricated by varying the number of the bilayers repeats N from 6 to 18 but fixing the bilayer thickness at the optimized value 5.7 Å. The total film thickness was varied from 3.4 nm to 10.2 nm. Samples were annealed via RTA at 400˚C. Figure 6-8 shows the normalized in-plane and out-of-plane hysteresis loops for the four

samples. As the thickness was increased the magnetic anisotropy rotated from perpendicular-to-the-plane to in-plane.
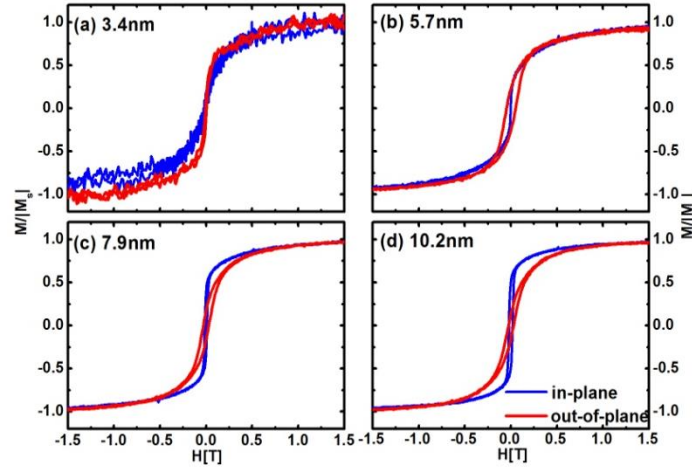
Figure 6-8 Normalized in-plane (blue dashed line) and out-of-plane (red solid line) hysteresis loops of samples in a structure of [Al/Mn(5.7 Å)]$_N$ with N selected as 6, 10, 14, 18, corresponding to film thicknesses of 3.4 nm, 5.7 nm, 7.9 nm and 10.2 nm.

Figure 6-9 shows the variation of the uniaxial anisotropy constant K_u and the c/a ratio for MnAl as the total film thickness ranged from 5.7 nm to 10.2 nm. The c/a ratio was calculated based on the out-of-plane and in-plane XRD results. The effective average anisotropy K_{eff} was first calculated by the area method introduced previously, allowing the calculation of K_u by deducting the contribution of shape anisotropy $2\pi M_s^2$ from K_{eff}[86]. When the thickness was 5.7nm (N=10), the perpendicular anisotropy field was dominant in the sample giving a K_u around 1.2×10^6 erg/cc. When the thickness was increased to 10.2 nm (N=18), it showed an in-plane anisotropy field with a negative uniaxial anisotropy constant of -0.7×10^5 erg/cc. Meanwhile, the lattice distortion c/a ratio exhibited a change from 1.02 to 1.00 as the thickness increased, suggesting a lattice strain dependent on the film thickness.
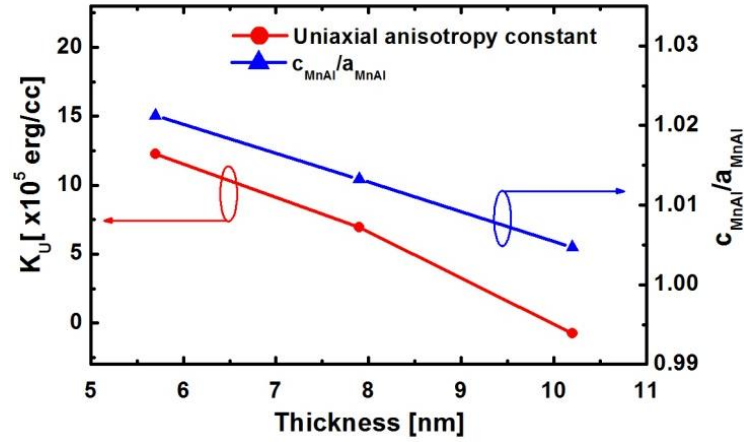
Figure 6-9 Dependence of the uniaxial anisotropy constant K_u and *c/a* ratio on the film thickness. The samples are in a structure of [Al/Mn(5.7 Å)]$_N$ with *N* varied from 10 to 18.

The change of K_u was due to the dependence of crystalline anisotropy on the lattice distortion, according to the spin polarized band calculation for τ phase MnAl in the literature[70, 140]. The theoretical prediction of the film anisotropy as a function of *c/a* ratio is shown in Figure 6-10. The system has a perpendicular uniaxial anisotropy along the *c*-axis for a *c/a* ratio above 1. It was reported in previous work that MnAl thin films on AlAs(001)/GaAs substrates had lattice parameters of *a* and *c* ~2.83 Å and 3.40 Å, yielding a *c/a* ratio of ~1.2, accompanied by a large PMA along the *c*-axis[67]. When the tetragonal distortion is reduced, approaching the critical value of 1, the magnetic anisotropy energy difference (ΔMAE) between the [110] direction and the [001] direction is diminished and shows an abrupt change from positive to negative near *c/a*=1, giving rise to a planar anisotropy. In the system of MgO(001)/τ-MnAl (5.7nm), due to the lattice mismatch between the MgO and τ-MnAl lattices, the in-plane lattice constant *a* was strained to ~2.98 Å with the spacing along *c*-axis reduced down to ~3.04 Å, leading to a crystal structure close to a lightly distorted B2 cubic structure, with which the

perpendicular anisotropy still survived. As the film thickness was increased, the *c/a* ratio showed a decreasing tendency approaching to 1 due to the change of the lattice strain. As a result, the ΔMAE decreased leading to the magnetic anisotropy gradually reorienting from out-of-plane to in-plane.
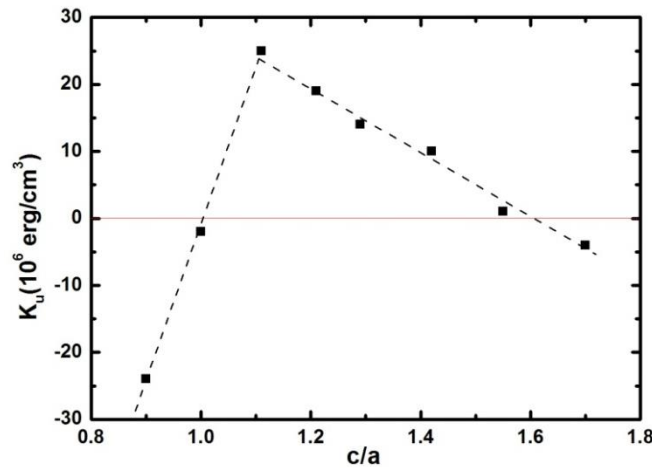
Figure 6-10 Theoretical dependence of the uniaxial anisotropy of MnAl on the lattice distortion ratio *c/a*. (data adapted from Ref [70])

Additionally, it was also noticed that the saturation magnetization M_s of the films was reduced as the thickness was reduced (Figure 6-11). Such a trend was also observed in thin Co_2FeAl films, implying the existence of a 'magnetically' dead layer. The 'dead' layer can be associated with the interfacial defects or an intermixing between MnAl and the Ta capping layer. Figure 6-11 shows the linear fitting of the magnetization per unit area, m_s, as a function of the film thickness to determine the 'dead' layer thickness and the extracted magnetization M_0 (Refer to Equations **(5-2)** and **(5-3)**). The dead layer thickness is given by the x-intercept, which was found ~ 2.7 nm, while the slope gives the extracted M_0 of 523 emu/cc, equivalent to ~1.90 μ_B/Mn. This value is consistent with the theoretical prediction. Due to the mismatch strain from the MgO substrates, the *c/a* ratio

decreases from the bulk value 1.3 to 1.0. It was shown by DOS calculations that for a composition of $Mn_{50}Al_{50}$, the magnetic moment changes correspondingly from 2.33 μ_B/Mn to 1.975 μ_B/Mn with the decrease of the lattice distortion[70]. The theoretical result reported by Park et al. also indicated a magnetic moment of 1.88 μ_B/Mn in a B2 lattice[140].
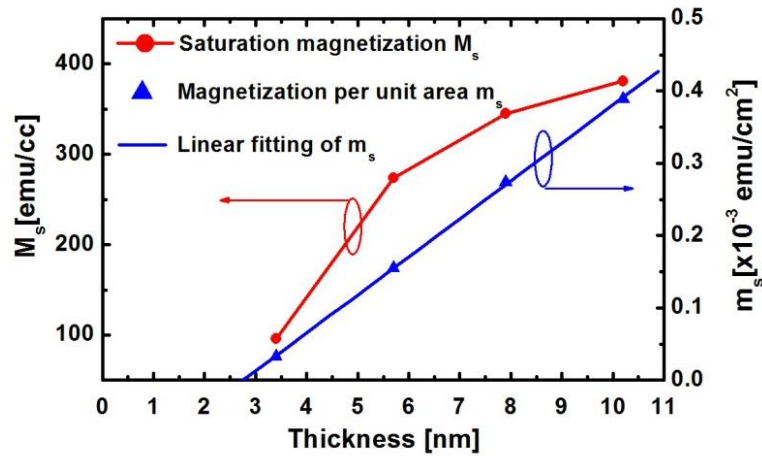
Figure 6-11 Dependence of the magnetization on the film thickness. The samples are in a structure of [Al/Mn(5.7 Å)]$_N$ with N varied from 10 to 18.

6.3   Other growth templates for τ-MnAl

The large impact of strain on the magnetic anisotropy led to the search for a seedling template with a smaller lattice mismatch to achieve PMA in τ-MnAl films. The following sections review the growth of MnAl on templates Cr buffered MgO(001) and GaAs(001), and their structural and magnetic properties compared to those of MnAl films on MgO(001). In this section, MnAl was synthesized using the optimized co-sputtering recipe thus the film composition was fixed at $Mn_{50.6}Al_{49.4}$.

6.3.1   MnAl on Cr-buffered MgO(001)

6.3.1.1   Optimization of fabrication conditions

Cr has a Body Centered Cubic structure with a lattice constant $a_{Cr} \sim 2.89$ Å when grown on MgO(001) substrates (Chapter 5). Thus the lattice mismatch with MnAl is expected to be reduced. For the sample fabrication, MgO(001) substrates were first heat treated and cleaned using the standard approach mentioned previously, followed by the deposition of Cr(40)/ MnAl(50)/ Cr(5) stacks. The growth temperature was varied from 100 ˚C to 250 ˚C for a preliminary crystallization of Cr and MnAl layers to enhance the epitaxial growth of each layer. All the samples were post-annealed at 500˚C for 30 seconds in the RTA furnace. For comparison, MnAl was directly co-deposited on MgO(001) at room temperature and annealed at 400˚C for 12 seconds, following the optimized co-sputtering recipe [13].

Figure 6-12 demonstrate the dependences of the magnetization and the PMA on the deposition temperature before and after annealing treatments, while other growth parameters were remained unchanged. For samples grown at a given temperature, both magnetic properties were dramatically improved after the annealing treatment, implying the recrystallization may have taken place during the annealing treatments. For the annealed samples, both the PMA and magnetization were significantly improved as the substrate temperature was raised from 100˚C to 250˚C. It could be ascribed to the enhancement of the crystallinity of the Cr layer, thus providing a better seeding condition. On the other hand, the roughness of the Cr seeding layer increased due to the crystallization as the temperature exceeded 200˚C, as demonstrated in Chapter 5.

Therefore the growth temperature was selected at 200°C for the growth of MnAl, which was also applied in the fabrication of the perpendicular spintronic devices discussed later.
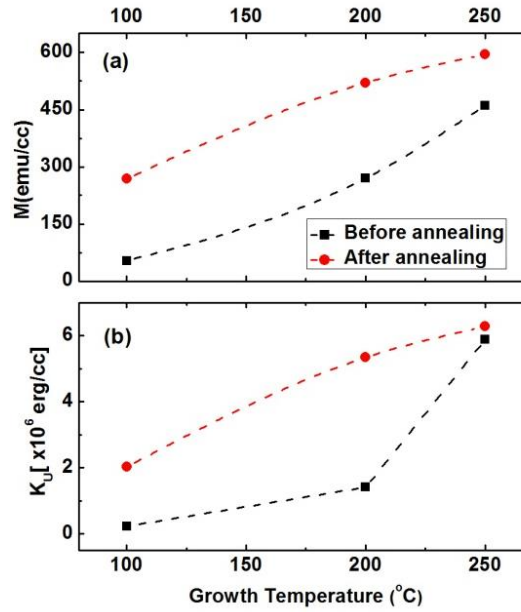
Figure 6-12 (a) Dependence of the saturation magnetization on the growth temperature for samples as-deposited (black square) and annealed at 500°C (red circle). (b) Dependence of the uniaxial anisotropy on the growth temperature for samples as-deposited (black square) and annealed at 500°C (red circle). The dash line is added to guide the eye.

6.3.1.2 Structural and magnetic properties

Figure 6-13 showed the *2θ* scans for the samples grown on MgO(001) substrates with a Cr buffer layer (a) as well as those without a Cr buffer layer for compare(b). The corresponding sample in Figure 6-13(a) was deposited at a temperature of 200°C and heat treated at 500°C in RTA. The peak at 64.34° was due to the diffraction of $(002)_{Cr}$ planes indicating the *bcc* crystallization of Cr layer. The superlattice and fundamental peaks of MnAl were shifted to 25.30° and 51.70° respectively, compared to the *2θ* scan for the one deposited directly on MgO(001) substrates in Figure 6-13(b).
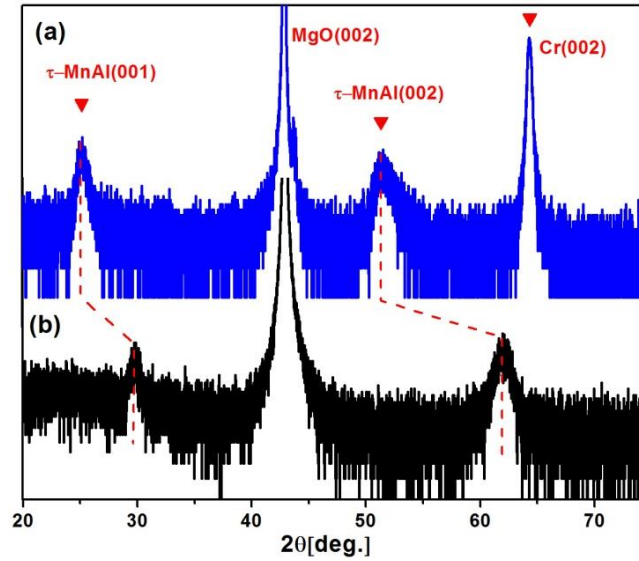
Figure 6-13 (a) *2θ* **scan for** *τ***-MnAl deposited on a Cr-buffered MgO substrate at a growth temperature 200 °C. (b)** *2θ* **scan for** *τ***-MnAl deposited on a MgO(001) substrate in comparison.**

φ scans were similarly taken with *2θ* positions corresponding to the *τ*-MnAl (011), Cr(011) and MgO (022) peaks to explore the growth strategy of each layer (Figure 6-14(a)). In this case, an in-plane 45° orientation offset occurred between the $(001)_{Cr}$ and $(001)_{MgO}$ planes while planes $(110)_{Cr}//(100)_{MgO}$ along the *c*-axis. On the other hand, the *τ*-MnAl grew on the Cr layer coherently with planes $(001)_{τ\text{-MnAl}}//(001)_{Cr}$ and $(100)_{τ\text{-MnAl}}//(100)_{Cr}$. The schematic diagram for the described lattice matching is presented in Figure 6-14(b). The lattice mismatch was reduced to ~4.4% based on the XRD results, indicating the role of the Cr buffer layer to reduce the lattice mismatch between a_{MgO} and $a_{τ\text{-MnAl}}$[75]. The lattice parameters yielded a *c/a* ratio ~1.26, which is much larger than that of MnAl grown on MgO directly (~1.0). The film surface has a roughness under 0.3 nm.
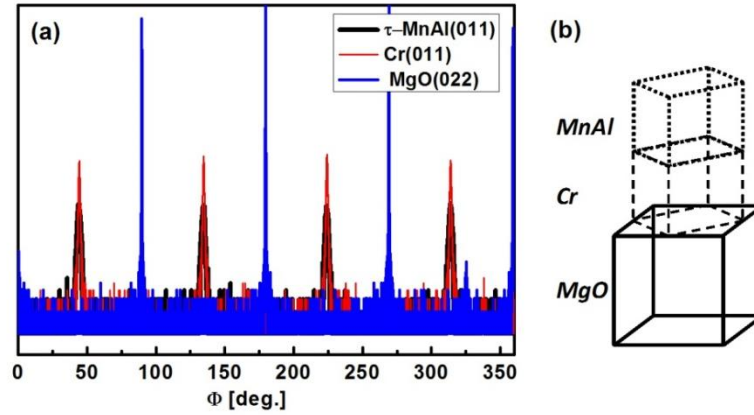
Figure 6-14 (a) *φ* scans on *τ*-MnAl deposited on a Cr-buffered MgO substrate at a growth temperature 200 °C. The black line represents data taken at *2θ* of 41.08° (τ-MnAl (011) peak), the red one for data taken at 44.24° (Cr (011) peak) and the blue one for data taken at 62.45° (MgO (022) peak). (b) Schematic diagram of the epitaxial relationships at MgO/Cr and Cr/MnAl interfaces.

The magnetic characterization of the same sample was shown in Figure 6-15. A large perpendicular magnetic anisotropy around 5.34 x 10^6 erg/cc was achieved as well as a high magnetization ~521 emu/cc. The magnetic anisotropy is one order of magnitude larger than that of MnAl directly deposited on MgO(001), which was within the expectation given the dependence of the film anisotropy on *c/a* ratio in Figure 6-10.
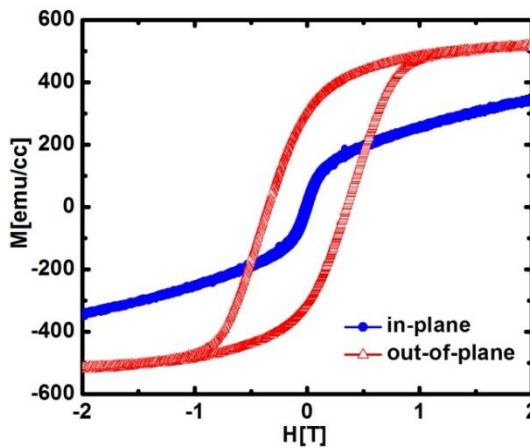
Figure 6-15 In-plane (blue) and out-of-plane (red) hysteresis loops of the sample *τ*-MnAl deposited on a Cr-buffered MgO substrate at a growth temperature 200 °C.

6.3.2 MnAl on GaAs(001)

The second template candidate in consideration is GaAs(001), which has been widely adopted in most reports on perpendicularly magnetized MnAl films[65-68]. The lattice mismatch between a_{MnAl} and a_{GaAs} is as small as 2% thus an epitaxial growth of τ-MnAl is expected[65, 66]. In most previous studies, τ-MnAl films were fabricated by evaporating Al and Mn simultaneously using molecular beam epitaxy (MBE)[65-67]. Typically, intentional heating to the substrates ~ 200˚C was applied during the film growth using MBE while a higher growth temperature ~ 440˚C was preferred using other deposition methods such as pulsed laser deposition (PLD)[68]. For this reason, film growth at elevated temperatures was carried out in my study.

MnAl(20)/Ta(7) stacks were deposited on the GaAs(001) substrates. The first series (6-B-1) was deposited at elevated temperatures from 350 ˚C to 475 ˚C and heat treated at 400˚C; the second series (6-B-2) was deposited at room temperature followed by a post annealing treatment at temperatures from 300 ˚C to 600 ˚C. Table 6-2 summarizes the details of the two series.

Table 6-2 Growth temperature and annealing temperature were adjusted to optimize the MnAl film quality.

Series	Substrate Temperature	Annealing Temperature
6-B-1	350 ˚C ~ 475 ˚C	As-deposited/ 400 ˚C
6-B-2	No *in-situ* heating	300 ˚C ~ 600 ˚C
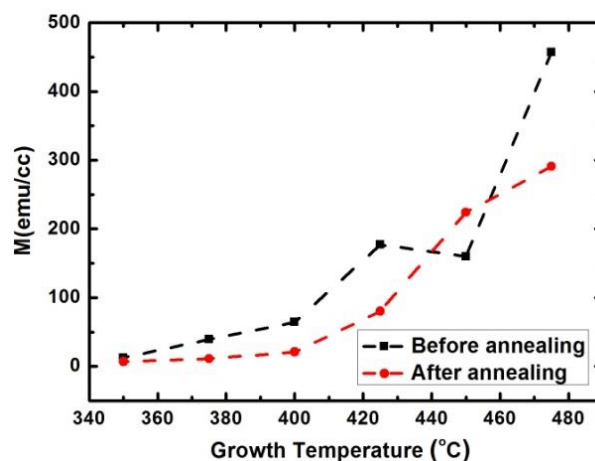
Figure 6-16 Dependence of the saturation magnetization on the growth temperature for Series 6-B-1 (as-deposited (black square) and annealed at 400˚C (red circle)). The dash line is added to guide the eye.

Figure 6-16 shows the dependence of the film magnetization on the substrate temperature in Series 6-B-1 before and after post-annealing treatments. It was revealed that the film magnetization was improved as the substrate temperature increased, indicating the atomic thermal kinetic energy promoted the τ-MnAl formation. On the other hand, the annealing treatment didn't necessarily help the recrystallization of the τ phase in MnAl. It is also worth mentioning that in most samples the perpendicular component of the magnetic anisotropy vanished after post annealing treatments. The changes of the magnetic anisotropy could be possibly ascribed to reactions at MnAl/GaAs interfaces during annealing.

Figure 6-17 showed the typical magnetic and structural characterizations for one sample from Series 6-B-1 grown at 450˚C without any post annealing treatment. The saturation moment was as low as ~160 emu/cc. Perpendicular anisotropy was dominant in the film combined with a small portion of in-plane anisotropy. Correspondingly, the *2θ*

scan indicated the distortion c/a ratio around 1.32, consistent with the theoretical prediction. One should note that an additional peak was observed and indexed as τ-MnAl (110) peak, which could be one of the reasons for the partial in-plane anisotropy. The mixed anisotropies and the low magnetization also might be ascribed to the possible existence of multiple phases in the MnAl films and the interdiffusion and reactions at MnAl/GaAs interfaces. In most previous literatures, an epitaxial AlAs layer was introduced as the buffer layer before MnAl growth. When grown on GaAs(001), AlAs has the same lattice mismatch ~ 2% in comparison with the τ-MnAl lattice. Besides, the adjacent AlAs layer contains the same III element Al as the MnAl layer, which minimizes any driving force for interfacial reactions[65, 66].
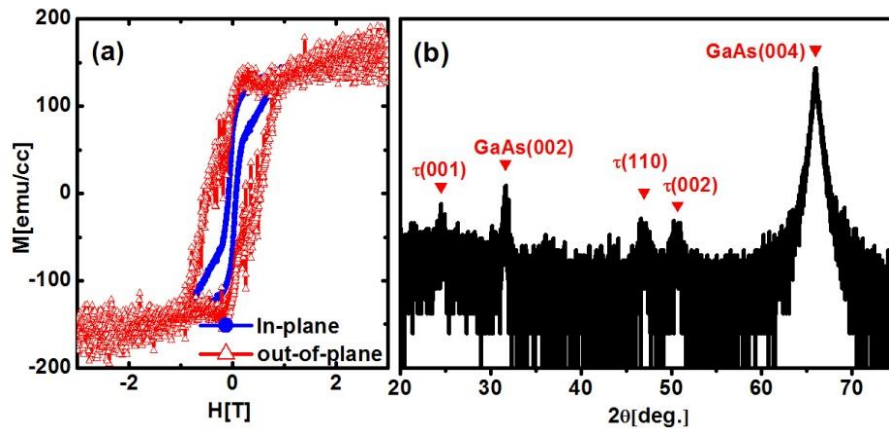
Figure 6-17 (a) In-plane (blue) and out-of-plane (red) hysteresis loops of the sample MnAl(20)/ Ta(5) grown on GaAs(001) at 450˚C. (b) *2θ* scan for the same sample.

Another hurdle for adopting this growth approach in spintronic device fabrication is the high level of the film roughness. It indicated that the sample roughness rose sharply with the growth temperature from 5.39 nm at 350˚C up to 11.34 nm at 450˚C. The situation was improved in Series 6-B-2 which was grown at room temperature. The

roughness was reduced to 0.69 nm yet the highest magnetization achieved was also reduced to only 74 emu/cc even with an RTA treatment at 550˚C.

In summary, the MnAl growth on GaAs is not favorable. *In-situ* heating introduced multiple crystal orientations indicated by the XRD. The high growth temperature also increased the film roughness. Room temperature deposition reduced the film roughness effectively but the magnetization was much lower than that of MnAl grown on MgO(001). The comparison of the MnAl properties grown on different templates are listed in Table 6-3.

Table 6-3 Comparison of properties of MnAl grown on MgO(001), Cr-buffered MgO(001) and GaAs(001).

Growth template	Film roughness	Magnetization	Magnetic anisotropy
MgO(001)	0.20 nm	394 emu/cc	In-plane
Cr buffered MgO(001)	0.30 nm	521 emu/cc	Fully perpendicular
GaAs(001)	0.67 nm	74 emu/cc	Partially perpendicular
	11.34 nm	160 emu/cc	Partially perpendicular; Non uniform

6.4   Summary

This chapter was devoted to the synthesis and characterization of ferromagnetic MnAl films, which is considered as a promising electrode candidate for p-MTJs in the STT-MRAM application. I started from depositions on MgO(001) which was pointed out as an ideal template for τ-MnAl growth in Ref[13]. The alternating Al/Mn quasi-monolayer deposition on MgO(001) was systematically optimized to enhance the crystallization of MnAl films thus improving their magnetic properties, in comparison with the co-sputtering approach. The XRD pattern for these films exhibited the well-

formed τ phase and both an in-plane and out-of-plane epitaxial relationship between the τ phase MnAl and the single crystal MgO. The tetragonal distortion c/a ratio was ~1 due to the templating effect provided by the MgO(001) substrates. The magnetic anisotropy was in-plane, which can be ascribed to the B2 structure (c/a ratio ~1) of MnAl films according to the spin polarized band calculation in previous literatures. A thickness-dependent change in the magnetic anisotropy in these films had been observed, which could be explained by the change of the lattice distortion (c/a ratio) as a function of film thickness. The extrapolated magnetization M_E in MnAl films grown on MgO(001) was 523 emu/cc (~1.90 μ_B/Mn), close to the theoretically predicted value (~1.975 μ_B/Mn). A damping parameter ~0.033 was obtained in the multilayered MnAl films.

Given the key effect of the template strains on the magnetic anisotropy of the MnAl films, further extensive studies were carried out, seeking a more appropriate template substrate to induce a large PMA in MnAl films. Cr buffered MgO(001) and GaAs(001) were proposed. Growth parameters such as substrate temperature and annealing conditions were carefully examined to optimize the MnAl film properties. Detailed comparisons were made within three growth templates including MgO(001), Cr buffered MgO(001) and GaAs(001). Particularly, MnAl grown on Cr buffered MgO(001) demonstrated a large PMA ~ 5.34 x 10^6 erg/cc along with a magnetization ~ 521 emu/cc. On the other hand, GaAs substrates failed to induce ideal MnAl film quality, which was possibly due to the interdiffusion and reactions at the MnAl/GaAs interfaces.

In conclusion, I have shown the modulation of the magnetic anisotropy of MnAl by modifying the lattice distortion ratio via the strain engineering. MnAl has the desired

combination of the ideal crystal structure, the low damping parameter and the large PMA

that is suitable for perpendicular spintronic applications.

7. Preliminary exploration of spintronics devices

7.1 Pseudo spin valves Co$_2$FeAl/Cr/Co$_2$FeAl

7.1.1 Sample preparation

All the samples were deposited on MgO(001) substrates using RBTIBD. Pseudo spin valves have a structure of Co$_2$FeAl(5)/Cr(x)/Co$_2$FeAl(5)/Al(5). The thickness of the Cr layer x was varied from 1.5 nm to 5 nm. The Al capping layer prevented oxidation in spin valve samples. VSM was used to characterize the magnetic behavior of the spin valves from room temperature to 50K. The *Van der Pauw* configuration was used for the magnetoresistance(MR) measurements.

7.1.2 Interlayer coupling

(i) Numerical simulation

In order to estimate the interlayer couplings quantitatively, the magnetization curves were simulated by minimizing the total energy of the pseudo spin valve samples. The total energy consists of Zeeman energy E_Z, anisotropy energy E_K, and exchange coupling energy E_J [142, 143]:

$$E_T = E_Z + E_K + E_J \qquad \text{(7-1)}$$

while each term is given as:

$$E_Z = -M_a t_a H \cos\alpha - M_b t_b H \cos\beta, \qquad \text{(7-2)}$$

$$E_K = K_a t_a \sin^2\alpha \cos^2\alpha + K_b t_b \sin^2\beta \cos^2\beta, \qquad \text{(7-3)}$$

$$E_J = -J_1 \cos(\alpha - \beta) - J_2 \cos^2(\alpha - \beta). \qquad \text{(7-4)}$$

The subscripts *a* and *b* refer to the bottom and top ferromagnetic Co_2FeAl layers, respectively. The parameters *M, t,* and *K* represent the saturation moment, thickness, and the first order cubic magnetocrystalline anisotropy energy constant of the corresponding layer. α and β are the angles between the magnetization and the external field for bottom and top Co_2FeAl layer, respectively (assuming the external field is applied along the direction of the anisotropy field). Therefore, the total moment of the sample can be estimated by $M_a t_a \cos\alpha + M_b t_b \cos\beta$. J_1 and J_2 are the exchange coupling constants of bilinear and biquadratic couplings. A positive/negative J_1 gives $0^o/180^o$ alignments, corresponding to ferromagnetic or antiferromagnetic coupling. A negative J_2 stabilizes 90° alignment between the two ferromagnetic layers. The energy expression can be simplified in my study due to the identical bottom and top ferromagnetic layers. *M, t,* and *K* are 1000 emu/cc, 5 nm, and 3 x 10^3 erg/cc respectively, which can be obtained from experiments. The toy model assumes coherent switching of Co_2FeAl regardless of the magnetic domain configuration and pinning sites. However it sheds some light on the variation of the exchange coupling constants.

Figure 7-1 shows the simulated magnetization curves with positive bilinear coupling constants J_1, assuming $J_2 = 0$. The ferromagnetic coupling leads to simultaneous switching of the two Co_2FeAl layers, thus resulting in a remnant normalized moment M_r/M_s equal to 1 and a saturation field H_s at 0. The magnetization curves show no dependence on the magnitude of the coupling constant.
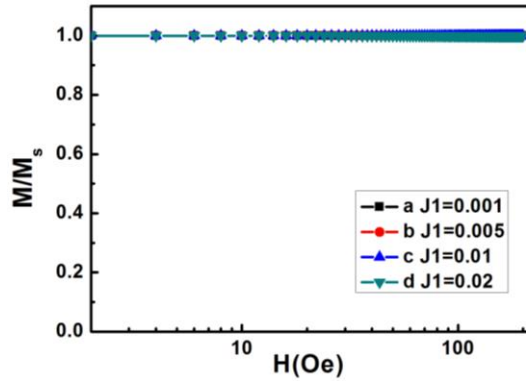
Figure 7-1 Calculated magnetization curves with positive J_1. From a to d, J_1 = 0.001, 0.005, 0.01, 0.02. J_2 is assumed as 0.

The simulated magnetization curves with a negative bilinear coupling constant J_1 is shown in Figure 7-2. At zero field, an energy minimum was reached with antiparallel alignment of the two ferromagnetic layers, leading to a zero M_r/M_s regardless of the magnitude of the coupling strength. As $-J_1$ increased, a larger magnetic field was required to overcome the exchange coupling energy, resulting in an increased H_s. The simulated shape of the magnetization curve is consistent with previous experimental results observed in sandwiched structures with a dominant antiferromagnetic coupling[144, 145].
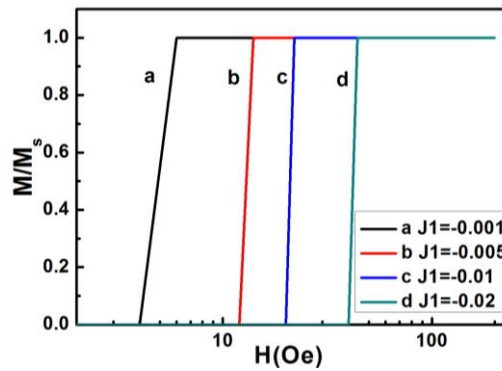
Figure 7-2 Calculated magnetization curves with negative J_1. From a to d, J_1 = -0.001, -0.005, -0.01, -0.02. J_2 is assumed as 0.

Figure 7-3 demonstrates the contribution of a negative J_2 to the magnetization curves while keeping $J_1 = 0$. A 90° alignment is preferred at zero field due to the biquadratic coupling. Therefore, the M_r/M_s ratio can be evaluated by $t_a/(t_a + t_b)$, which is 0.5 in this case[142, 143, 146, 147]. The saturation field increases as the coupling constant $-J_2$ is raised since a larger Zeeman energy is required to align two ferromagnetic layers to be parallel with each other.
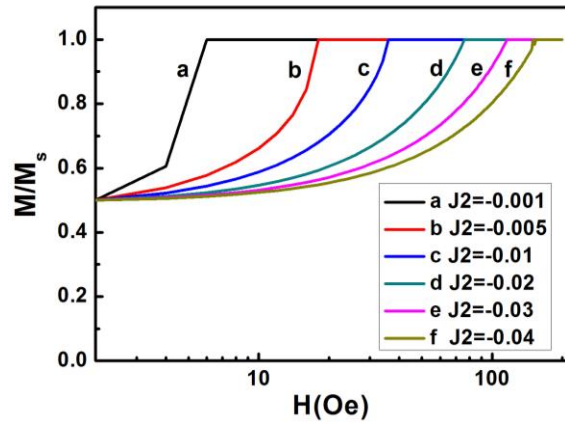
Figure 7-3 Calculated magnetization curves with negative J_2. From a to f, J_1 = -0.001, -0.005, -0.01, -0.02, -0.03, -0.04. J_1 is assumed as 0.

(ii) Thickness effect

The black lines with squares in Figure 7-4 show the experimental magnetic hysteresis loops of the pseudo spin valve samples with different Cr spacer thickness.
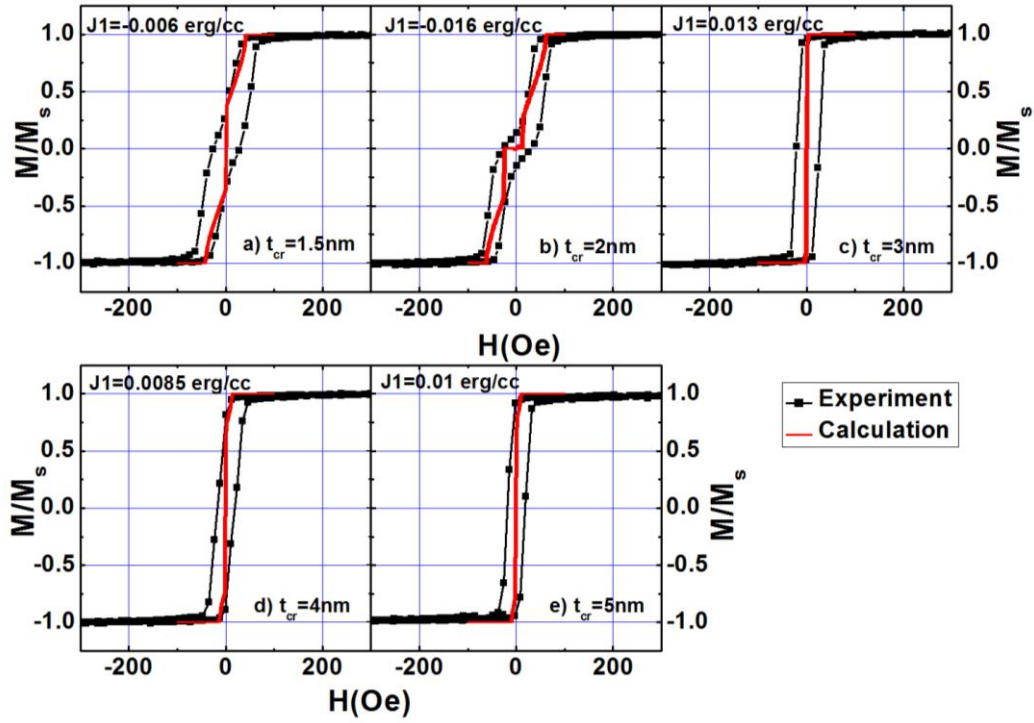
Figure 7-4 Experimental (black line with squares) and calculated hysteresis loops (red line) of samples (a-e) with different Cr thickness varied from 1.5 nm to 5 nm. The samples were measured room temperature. J_2 is assumed as a constant of -0.009 erg/cc.

The experimental M_r/M_s for each sample is shown in Figure 7-5. M_r/M_s remained in the range of 0 to 0.5 for sample (a) and (b), indicating the existence of an antiferromagnetic coupling (negative J_1). In samples (c)-(e), M_r/M_s varied in the range of 0.5 to 1, corresponding to a ferromagnetic coupling (positive J_1).
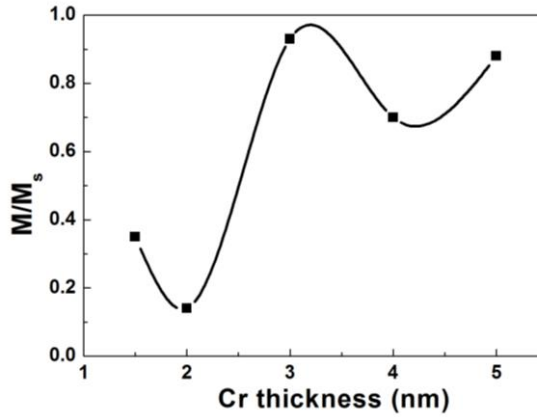
Figure 7-5 Experimental M_r/M_s for samples (a-e) with different Cr thickness varied from 1.5 nm to 5 nm. The solid line is added to guide the eye.

Furthermore, the two ferromagnetic layers are not perfectly aligned at 0° or 180° at zero field, implying a possible contribution from a 90° coupling (negative J_2). In previous studies, a large variation of saturation field was observed from tens of Oe up to 8000 Oe in similar sandwiched structures[142, 143, 146-148], including $Co_2FeAl/Cr/Co_2FeAl$[148]. The variation was ascribed to the oscillation of the biquadratic exchange coupling. In my study the saturation field remains below 50 Oe in all of the samples, indicating the change of the biquadratic coupling J_2 was barely perceivable. Therefore, J_2 is assumed as a constant $\sim$ -0.009 erg/cc in this case. The different behavior of the biquadratic coupling could be due to the choice of the capping layer, as reported in previous literature [148]. The calculated hysteresis curves were shown in red in Figure 7-4. A deviation in the coercive field between the experimental and calculated curves was observed. The deviation is attributed to the unrealistic assumption of single magnetic domain configuration without pinning sites in the ferromagnetic Co_2FeAl layers. The oscillatory experimental M_r/M_s led to an oscillatory J_1

to best fit the magnetic hysteresis curves (Figure 7-6). The oscillation of the bilinear coupling with a period of ~12 ML has been previously reported in Fe/Cr/Fe structures [149, 150]. There were several explanations for the origin of this coupling[151-153]. The consensus is that the oscillatory exchange coupling can be associated with the spin-dependent reflection at the interfaces. The oscillation period is determined by the critical spanning vectors of the Cr Fermi surface[29, 154].
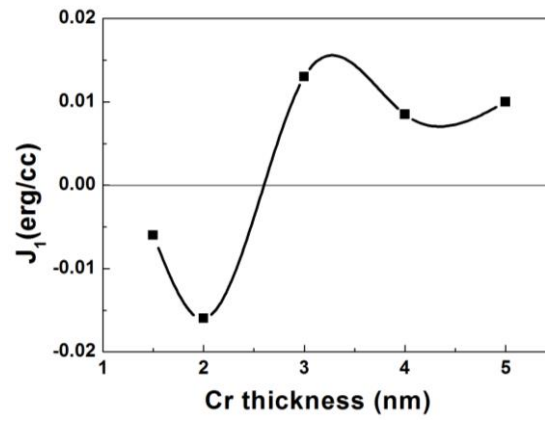
Figure 7-6 Calculated J_1 for samples (a-e) with different Cr thickness varying from 1.5 nm to 5 nm. The thick line is added to guide the eye. The sample showed a ferromagnetic coupling with a J_1 above the straight line and an antiferromagnetic coupling with that below the line.

(iii)　　Temperature effect

The magnetization curve of sample (a) with a Cr thickness ~1.5 nm was also measured at different temperatures from 300 K to 50 K, as shown in Figure 7-7 in black.
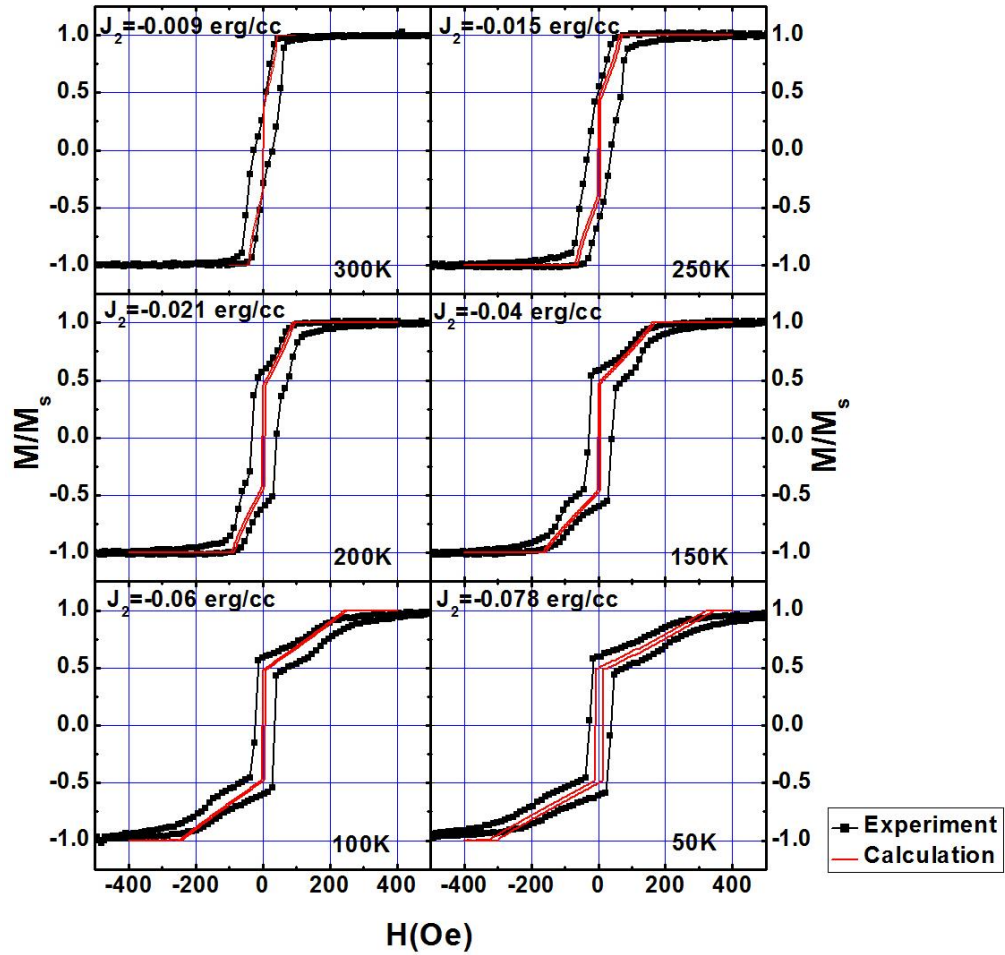
Figure 7-7 Experimental (black line with squares) and calculated hysteresis loops (red line) of sample (a) (Cr thickness = 1.5 nm) measured at different temperatures from 300K to 50K. J_1 is assumed as a constant of -0.006 erg/cc.

Figure 7-8 shows M_r/M_s and H_s as functions of the measurement temperature. It was noticed that M_r/M_s was around 0.36 at 300 K, but increased to ~ 0.55 as the temperature was reduced to 250 K and stayed at the same level at lower measurement temperatures. On the other hand, H_s continued to increase up to ~ 310 Oe as the temperature was decreased to 50 K. This indicated that the contribution of the bilinear antiferromagnetic coupling J_1 was comparable to the contribution of the biquadratic coupling J_2 at 300 K. However, as the temperature was reduced to/below 250 K, the contribution of the

biquadratic coupling became dominant, and thus the constant M_r/M_s stayed close to 0.5. The magnitude of J_2 continued to increase significantly at lower temperatures, leading to an enhanced H_s. The change in the bilinear coupling strength J_1 was not notable compared to the change in J_2.
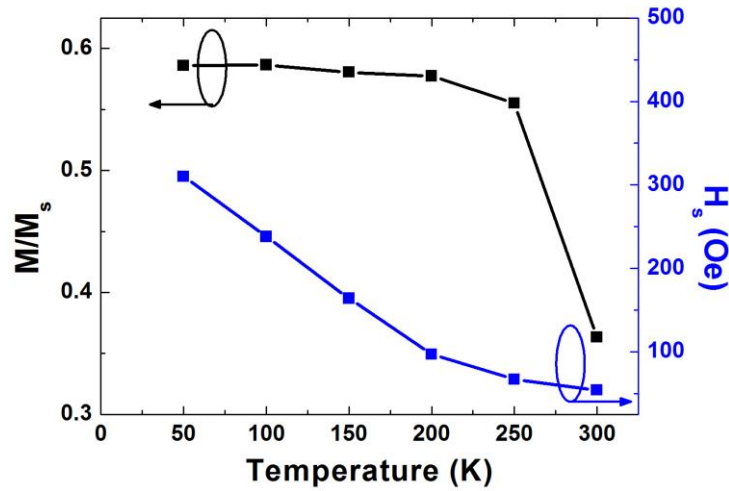
Figure 7-8 Experimental M_r/M_s and H_s varying with the measurement temperature from 300 K to 50 K. The sample has a Cr thickness of 1.5 nm.

The red lines in Figure 7-7 represented the calculated magnetization curves assuming the bilinear coupling J_1 is constant at -0.006 erg/cc. The variations of M_r/M_s and H_s were well described. The major feature of the experimental magnetization curves was reproduced in the calculated curves, in spite of the deviation of the coercive field due to the single domain assumption. This indicated that the analysis above was reasonable.

Figure 7-9 showed the simulated magnitude $-J_2$ varied with the temperature. Similar results were observed in Fe/Cr/Fe[155, 156] and other systems[157, 158].
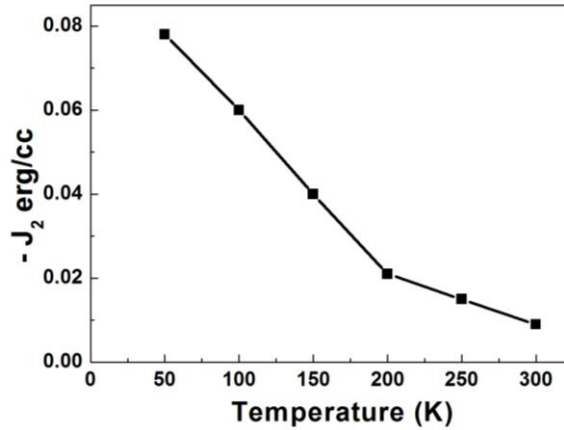
Figure 7-9 Calculated $-J_2$ as a function of the measurement temperature. The sample has a Cr thickness at 1.5 nm.

The biquadratic coupling cannot be related to the antiferromagnetic ordering in Cr. In Ref [156], it was shown the N éel temperature of Cr was reduced significantly reducing as decreasing film thickness. At thicknesses below 5 nm, Cr always had a paramagnetic ordering (Figure 7-10).

The near-linear behavior of J_2 as a function of the temperature indicated that the origin of the biquadratic coupling could be described using the thickness fluctuation model as mentioned in Chapter 2[35, 157], in which 90° couplings results from the compromise between 0° and 180° alignments.
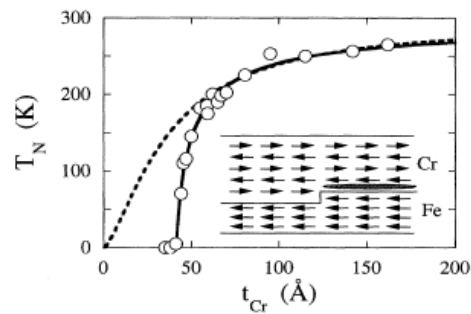
Figure 7-10 Thickness dependence of N éel temperature of Cr in Fe(14Å)/Cr(t_{Cr}) superlattices. The open circles represent the measured values. (adapted from Ref [156])

7.1.3 Magnetoresistance ratio (MR) characterization

The resistance response to the magnetic field was measured at room temperature (300 K) for sample (a) with the Cr thickness ~1.5 nm (Figure 7-11). Two resistance plateaus were observed. Parallel magnetizations of two layers were achieved above the saturation field H_s resulting in a low magnetoresistance. The resistance started ramping up as the magnetizations experienced a transition from the parallel alignment to an antiparallel alignment through a 90° alignment. The near-antiparallel alignment was achieved at a field from -14 Oe to -38 Oe, corresponding to the high magnetoresistance. The magetoresistance ratio was only around 0.1% in this sample.
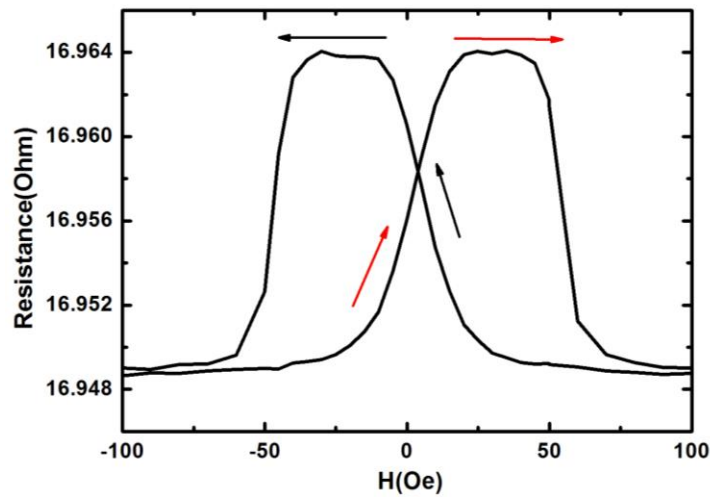
Figure 7-11 Magnetoresistance of the pseudo spin valve measured at room temperature (300 K). The sample has a Cr thickness of 1.5 nm.

7.2 Co$_2$FeAl based Magnetic tunnel junctions

7.2.1 MgO barrier layer

The quality of the MgO barrier layer is critical in achieving high TMR in magnetic tunnel junctions. It also plays a significant role in achieving interfacial perpendicular magnetic anisotropy in the interfaces of MgO and CoFe-based alloys. In our system, two approaches were developed to prepare a MgO layer. The first approach is natural oxidation, in which thin metallic a Mg layer (~1.3nm) is deposited followed by an oxidation procedure. The deposition/oxidation procedure is repeated to achieve the desired total thickness. In the oxidation procedure, the flow rate of O$_2$/Ar mixture was fixed at 10 sccm, while the oxidation time was varied from 100 seconds to 800 seconds. The second approach is to sputter metallic Mg in an oxygen ambient with a flow rate of 4 sccm.

To determine the oxidation state of MgO, samples with a structure of Ta(5)/CoFeB(2.5)/MgO(5)/Ta(5) were fabricated. A VSM measurement was performed at room temperature, and then the sample was cooled down to 50 K in a magnetic field followed by another VSM measurement. In the case of MgO barrier over-oxidation, a thin antiferromagnetic CoO will form at the ferromagnetic CoFeB surface. As the sample is cooled in a magnetic field from 300 K through the Néel temperature of CoO (293 K) down to 50 K, a FM/AFM exchange coupling can be observed in the low temperature magnetization curve of CoFeB, serving as an indicator of the MgO over-oxidation[159, 160]. Additionally, the film roughness was determined using the atomic force microscope.

Figure 7-12 showed the magnetic hysteresis loops of CoFeB at 300 K and 50 K. The MgO layer in the sample was fabricated using the first approach with an oxidation time ~ 400 seconds. Neither exchange bias nor coercive field broadening was observed at 50 K, indicating that there was no over-oxidation in the MgO layer. On the other hand, the inset shows the surface condition of an MgO film prepared in the same way. The roughness was ~ 1.84 nm. The non-uniform surface could possibly be due to an inhomogeneous oxidation of the Mg film. Besides, it was noticed that the film surface condition was independent of the oxidation time. One could possibly improve the surface condition with using a less drastic oxidation rate by reducing the O_2/Ar mixture flow rate and increasing the oxidation time. However these oxidation conditions lead to a less efficient synthesis of the MgO layer.
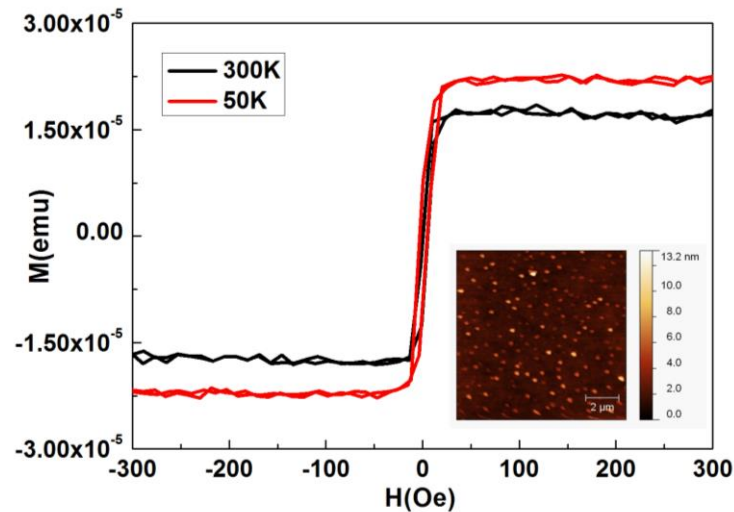
Figure 7-12 Magnetic hysteresis loops of sample Ta(5)/CoFeB(2.5)/MgO(5)/Ta(5) at 300 K and 50 K. The MgO layer was fabricated using the natural oxidation method. The inset shows the surface condition of a MgO film (~1.3 nm) prepared in the same way.

Figure 7-13 showed the VSM result of a Ta(5)/CoFeB(2.5)/MgO(5)/Ta(5) sample with the MgO layer prepared using the second approach. The surface scan of the sample

is also included. The film surface had a small roughness ~ 0.26 nm. However, the VSM result showed that the coercive field of CoFeB was broadened at 50 K, indicating the presence of a FM/AFM exchange coupling, indicative of over-oxidation of the MgO layer. This was expected because the CoFeB layer was exposed to the oxygen flow at the beginning of the MgO deposition. This over-oxidation was also observed in samples $Co_2FeAl(0.57)/Mg(x)MgO(2.3-x)$ for the interfacial PMA optimization (Chapter 5). No magnetic signal was detected without the protective thin Mg layer (x=0), indicating that the Co_2FeAl layer was fully oxidized.
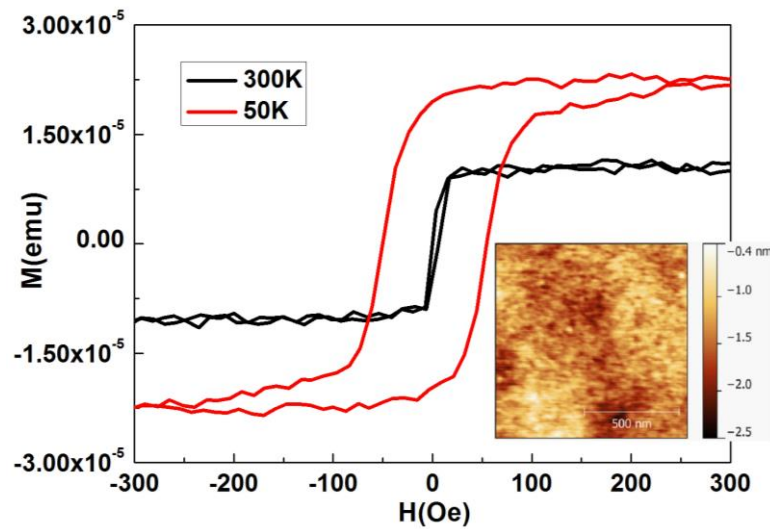
Figure 7-13 Magnetic hysteresis loops of sample Ta(5)/CoFeB(2.5)/MgO(5)/Ta(5) at 300 K and 50 K. The MgO layer was fabricated by reactive Mg sputtering. The inset shows the surface condition of a MgO film (~5 nm) prepared in the same way.

The over-oxidation of MgO can be effectively reduced by inserting a protective thin Mg layer before the MgO deposition. In Chapter 5, with a protective Mg layer thickness at 0.7 nm (x=0.7), the interfacial PMA was maximized, indicating a uniform, pure MgO layer with a minimization of the Co_2FeAl oxidation. A typical roughness ~ 0.2 nm was achieved using this approach.

7.2.2 Exchange bias in IrMn/Co$_2$FeAl

Three sample series were fabricated to study the exchange bias in IrMn/Co$_2$FeAl. Series 7-1 has a structure of IrMn(t)/Co$_2$FeAl(5nm)/Ru(5nm), in which the thickness of the IrMn layer t varies from 5nm to 15nm. Other growth condition for each layer was kept the same. Series 7-2 and 7-3 were designed to investigate the effect of the IrMn/Co$_2$FeAl interface condition on the exchange bias. The samples have a structure of IrMn(15nm)/Co$_2$FeAl(5nm)/Ru(5nm). In Series 7-2, the target bias for IrMn growth was varied from 300 V to 700 V, and the target bias for Co$_2$FeAl was fixed at 500 V. In Series 7-3, the target bias for Co$_2$FeAl was changed from 300 V to 700 V while IrMn was deposited with a target bias of 900 V. All the samples were annealed at 300 ˚C for 5 minutes in a magnetic field of 3000 Oe to establish the exchange bias. Table 7-1 summarizes the details of each series.

Table 7-1 Sample series designed for optimizing the IrMn/Co$_2$FeAl exchange bias.

Series	Sample Structure	IrMn target bias	Co$_2$FeAl target bias
7-1	IrMn(t)/Co$_2$FeAl(5nm)/Ru(5nm); t varied from 5-15nm	900 V	500 V
7-2	IrMn(15nm)/Co$_2$FeAl(5nm)/Ru(5nm)	300 – 700 V	500 V
7-3	IrMn(15nm)/Co$_2$FeAl(5nm)/Ru(5nm)	900 V	300 – 700 V

Figure 7-14 shows the magnetization curves of Co$_2$FeAl with different IrMn thicknesses. In sample (a) with a IrMn thickness of 5nm, the coercive field was broadened to ~ 100 Oe with an exchange bias close to 0. This indicated that the anisotropy of the antiferromagnetic IrMn layer $K_{AFM}t_{AFM}$ was relatively small compared to the interface coupling strength J_{INT} [18]. Therefore, the spins of IrMn follow the motion of the ferromagnetic spins, giving an enhanced coercive field instead of a non-

zero exchange bias. As the IrMn thickness was increased to 15nm, the magnetic anisotropy of the IrMn layer was improved, leading to a reduced coercive field ~ 19 Oe and an increased exchange bias ~ 211 Oe. The dependence of the coercive field and the exchange bias on the thickness of the antiferromagnetic layer has also been reported in previous literature. The magnitudes of H_c and H_{ex} eventually reached a saturation, which was related to the thickness of the partial domain wall in the antiferromagnetic layer parallel to the interface[161, 162].
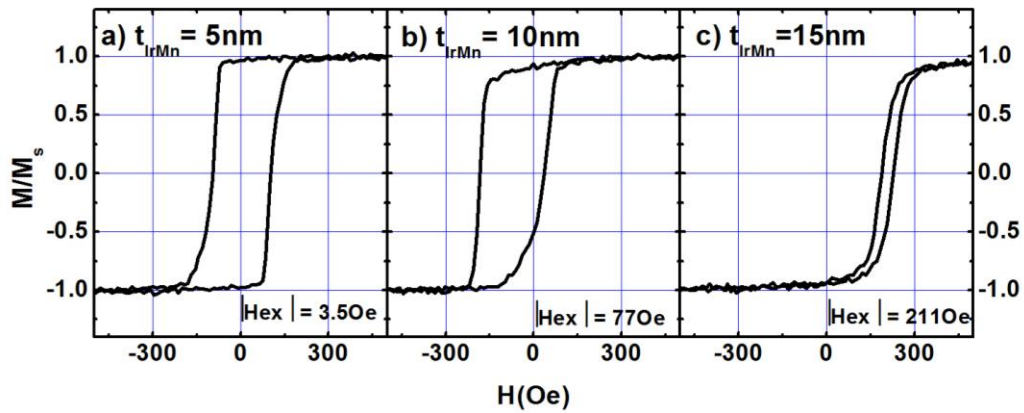
Figure 7-14 Magnetization curves of Series 7-1, in which the IrMn thickness increased from 5 nm to 15 nm.

Figure 7-15 demonstrates the effect of the growth target bias on the exchange bias. The target bias applied during the thin film growth is directly related to the sputtering energy gained by the atoms in sputtered materials. A large target bias results in a dense and chemically uniform film but, on the other hand, it promotes interlayer diffusion in multilayer structures. In Series 7-2, the exchange bias dramatically increased as the target bias applied during the IrMn growth was increased (Figure 7-15(a)). This is probably due to the fact that a denser and more uniform IrMn layer is achieved with a high target bias. On the other hand, the deposition bias of Co_2FeAl was varied in Series 7-3. In this case a

competing effect between the film uniformity and the interlayer diffusion has to be taken into account. The exchange bias deteriorated with a large target bias of Co_2FeAl due to the dominant interlayer diffusion effect.
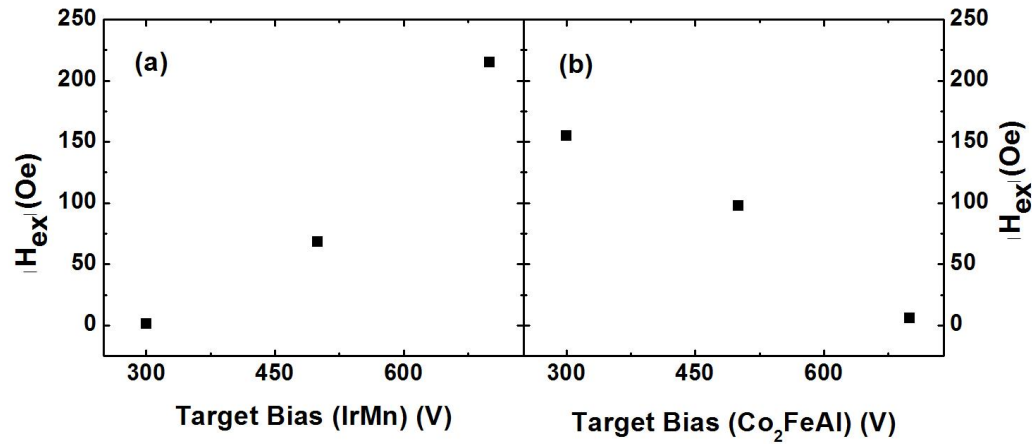
Figure 7-15 Dependence of the exchange bias on the target bias for the growth of the bottom IrMn layer (a) and the top Co_2FeAl layer (b).

7.2.3 Preliminary VSM results

Figure 7-16 shows the schematic structure of a Co_2FeAl based magnetic tunnel junction grown on a MgO(100) substrate and its magnetization curve. The exchange bias of the bottom Co_2FeAl layer (fixed layer) is around 228 Oe while the minor loop from the top Co_2FeAl layer (free layer) is centered at the zero field, indicating the negligible coupling between the fixed and the free layers. Lithographical patterning is required to define the device at micron scale to estimate the TMR.
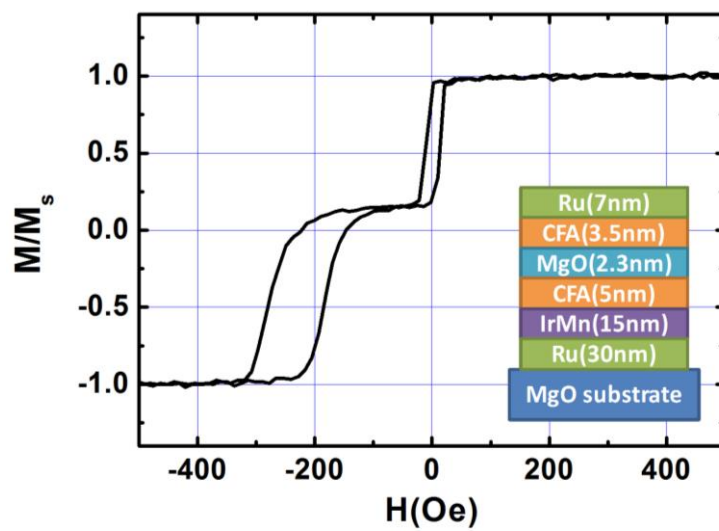
Figure 7-16 Magnetization curve of a Co₂FeAl-based magnetic tunnel junction. The inset shows the schematic structure of the magnetic tunnel junction.

8. Conclusion and Future Work

8.1 Research summary

The purpose of this dissertation is to investigate ferromagnetic materials aimed at reducing the critical current density for STT-MRAM applications. Preliminary efforts are also made to develop spintronic structures such as spin valves and MTJs.

In-plane material CoFeCrB was extensively studied. An amorphous feature was observed in as-deposited films, which is desired for a coherent *bcc* interface with MgO in MTJs. A *bcc* phase was formed with proper annealing treatments followed by a boron segregation at higher annealing temperatures. The boron segregation has to be suppressed in order to achieve a high TMR in MTJs. The onset crystallization temperatures showed a dependence on the Cr and B content. The Cr substitution also led to a reduced magnetization and an enhanced coercive field. On the other hand, the damping parameter in CoFeCrB was barely affected after Cr addition.

The B2-ordered Heusler alloy Co_2FeAl with an in-plane anisotropy was developed using different growth and post-annealing conditions. The magnetization, damping parameter and spin polarization were characterized. Their correlations with the B2 ordering parameter were discussed in detail. It was demonstrated that a high B2 ordering parameter is required in order to obtain a low damping parameter. In particular, an optimized B2 chemical ordering ~82.1% in the Co_2FeAl films annealed at 600 ˚C corresponded to a damping parameter at the level of ~0.002, which was much lower than that of CoFeB.

A dominant interfacial perpendicular magnetic anisotropy was achieved at Co_2FeAl/MgO interfaces with a reduced Co_2FeAl thickness (<2 nm). The perpendicular magnetic anisotropy was optimized by adjusting the MgO oxidation condition and the annealing condition. A maximized PMA ~1.9 x 10^6 erg/cc was achieved after annealing at 350 ˚C with no external magnetic field. This value is comparable to other interfacial PMA systems annealed in magnetic fields. The interfacial PMA of Co_2FeAl could be adopted in perpendicular STT-MRAMs for a reduced critical current density. The large value of PMA also allows for a high thermal stability of STT-memories. Additionally, the damping parameters of the perpendicularly magnetized Co_2FeAl films were characterized and were found to be lower that of CoFeB. This is another practical advantage of Co_2FeAl for STT-MRAM applications.

Ordered intermetallic τ-MnAl was synthesized with two growth approaches: co-sputtering and layer-by-layer deposition. Epitaxial growth of τ-MnAl was observed on template lattices including MgO(001), Cr(001), GaAs(001). Both the magnetization and the magnetic anisotropy of τ-MnAl were significantly affected by the lattice strains, which is consistent with the previous theoretical calculation. Particularly, a maximum PMA ~ 5.34 x 10^6 erg/cc along with a magnetization ~ 521 emu/cc was obtained in τ-MnAl films grown on Cr(001) lattices. The damping parameter of τ-MnAl films grown on MgO(001) templates was much lower compared to the damping parameter of other perpendicular systems such as FePt, CoPd and FeTb.

Table 8-1 shows the cross comparison of the benchmark properties between the three ferromagnetic materials in study to highlight their advantages and disadvantages for the STT-MRAM applications.

Table 8-1 Comparison of the benchmark properties of CoFeCrB, Co₂FeAl and MnAl for STT-MRAM applications.

	Amorphous on MgO before annealing	Lattice Mismatch with MgO	Ms (emu/cc)	Sample condition	Damping α	PMA (erg/cc)
CoFeCrB	Yes	3.9%	44~800 (Varied with Cr/B content)	450°C 30nm	0.006	No
Co₂FeAl	No	3.4%	1010	600°C 50nm	0.002	No
				400°C 1.36nm (CFA/MgO)	0.012	Yes (1.9 x 10⁶) Cr seeding/ MgO interface required
MnAl	Yes	6.7%	521	400°C 10nm	0.033	Yes (5.34 x 10⁶) Cr seeding required

Spintronic devices including pseudo spin valves and MTJs were developed. In pseudo spin valves Co₂FeAl/Cr/Co₂FeAl, two types of coupling strength were studied using numerical simulation. A combination of an oscillatory $0^o/180^o$ bilinear coupling and a near-constant 90° biquadratic coupling was observed with a varied Cr spacer thickness. As the measurement temperature was decreased, the biquadratic coupling strength became dominant, which resulted in an increasing saturation field and a constant remnant moment.

Co₂FeAl was integrated into a magnetic tunnel junction. The MgO barrier layer and the IrMn/Co₂FeAl exchange bias were preliminarily optimized, as both were critical for improving the TMR of MTJs.

8.2 Future work

8.2.1 Material aspect

(i) Half metal systems

Half metallicity was predicted in many Co/Fe based Heuslor alloys[54]. However, Co_2FeAl loses its half metallicity due to the strong hybridization between the Fe *3d* and Co *3d*[56]. Although a small minority band gap was obtained using the full potential linearized augmented plane wave model (FLAPW) in a previous study[122], the spin polarization is still low compared to other half metals. It has been predicted that a substitution of Fe with Cr gives rise to an enhanced minority band gap and an increased majority density of states at the Fermi level, thus leading to an improved spin polarization[56, 122]. PCAR measurements in bulk materials also confirmed that the spin polarization of B2 ordered Co_2CrAl was slightly improved and reach 58% whereas Co_2FeAl has a spin polarization of 53%[112]. Additionally, the magnetization was also diluted from 4.89 μ_B for Co_2FeAl down to 2.955 μ_B for Co_2CrAl according to the Slater-Pauling curve[54]. An increased spin polarization ~60% was also observed with a Si substitution ($Co_2FeSi_{0.5}Al_{0.5}$)[163]. On the other hand, the low damping parameter of Co_2FeAl might be compromised to some extent due to the altered shape of the DOS in Co_2CrAl[122]. A trade-off among the spin polarization, magnetization, and damping parameter has to be taken into account to find an optimal point of substitution.

(ii) Perpendicular systems

The τ phase is the only ferromagnetic phase of MnAl, which is metastable and only forms with a stoichiometric composition around $Mn_{0.5}Al_{0.5}$. One of the alternatives is

$Mn_{3-\delta}Ga$ system, in which thermodynamically stable ferromagnetic phases ($D0_{22}$ and $L1_0$) with perpendicular magnetic anisotropy can be achieved within a large range of δ (0~2)[74, 164]. A spin polarization ~58% was reported in Mn_3Ga and expected to be further improved by increasing the crystalline order[165]. Besides, a low damping parameter varied from 0.015 to 0.008 has been reported in Mn-Ga systems[74].

8.2.2   Device aspect

The magnetization loops of Co_2FeAl-based magnetic tunnel junctions showed well decoupled magnetic switchings in both the free and fixed layers. Lithography procedures are currently being developed to define MTJ devices in micron scale and thus to estimate the TMR. The TMR value can be also used as an indicator for the crystallization quality of MgO barrier layers. Thus, the growth and process conditions of MgO layer can be further fine-tuned accordingly. Perpendicular magnetized Co_2FeAl and τ-MnAl are also being adopted into spin torque oscillators(STO) for the future study of coupled STO arrays.

References

1. A. V. Pohm, J. S. T. Huang, J. M. Daughton, D. R. Krahn, V. Mehra, *The Design of a One Megabit Non-Volatile M-R Memory Chip Using 1.5 x 1.5 mm Cells.* IEEE Transactions on Magnetics, 1988. **24**: p. 3117.

2. M. A. M. Gijs, S. K. J. Lenczowski, J. B. Giesbers, *Perpendicular Giant Magnetoresistance of Microstructured Fe/Cr Magnetic Multilayers from 4.2 to 300 K.* Physical Review Letters, 1993. **70**: p. 3343.

3. Parkin SS, Kaiser C, Panchula A, Rice PM, Hughes B, Samant M, Yang SH, *Giant tunnelling magnetoresistance at room temperature with MgO (100) tunnel barriers.* Nature Materials, 2004. **3**: p. 862.

4. Shinji Yuasa, Taro Nagahama, Akio Fukushima, Yoshishige Suzuki, Koji Ando, *Giant room-temperature magnetoresistance in single-crystal Fe/MgO/Fe magnetic tunnel junctions.* Nature Materials, 2004. **3**: p. 868.

5. J. C. Slonczewski, *Current-driven excitation of magnetic multilayers.* Journal of Magnetism and Magnetic Materials, 1996. **159**: p. L1.

6. L. Berger, *Emission of spin waves by a magnetic multilayer traversed by a current.* Physical Review B, 1996. **54**: p. 9353.

7. Y. M. Huai, F. Albert, P. Nguyen, M. Pakala, T. Valet, *Observation of spin-transfer switching in deep submicron-sized and low-resistance magnetic tunnel junctions.* Applied Physics Letters, 2004. **84**: p. 3118.

8. Z. Diao, D. Apalkov, M. Pakala, Y. F. Ding, A. Panchula, Y. M. Huai,, *Spin transfer switching and spin polarization in magnetic tunnel junctions with MgO and AlO$_x$ barriers.* Applied Physics Letters, 2005. **87**: p. 232502.

9. Zhitao Diao, Alex Panchula, Yunfei Ding, Mahendra Pakala, Shengyuan Wang, Zhanjie Li, Dmytro Apalkov, Hideyasu Nagai, Alexander Driskill-Smith, Lien-Chang Wang, Eugene Chen, Yiming Huai *Spin transfer switching in dual MgO magnetic tunnel junctions* Applied Physics Letters, 2007. **90**: p. 132508.

10. Masahiko Nakayama, Tadashi Kai, Naoharu Shimomura, Minoru Amano, Eiji Kitagawa, Toshihiko Nagase, Masatoshi Yoshikawa, Tatsuya Kishi, Sumio Ikegawa, Hiroaki Yoda, *Spin transfer switching in TbCoFe/CoFeB/MgO/CoFeB/TbCoFe magnetic tunnel junctions with perpendicular magnetic anisotropy.* Journal of Applied Physics, 2008. **103**: p. 07A710.

11. N. F. Mott, *The Electrical Conductivity of Transition Metals.* Proceedings of the Royal Society (London), 1936. **153**: p. 699.

12. Claude Chappert, Albert Fert, Frédéric Nguyen Van Dau, *The emergence of spin electronics in data storage.* Nature Materials, 2007. **6**: p. 813.

13. W. Chen, PhD dissertation: *Structural and Material Exploration of Magnetic Tunnel Junctions*. 2010, University of Virginia

14. R. J. Soulen Jr., J. M. Byers, M. S. Osofsky, B. Nadgorny, T. Ambrose, S. F. Cheng, P. R. Broussard, C. T. Tanaka, J. Nowak, J. S. Moodera, A. Barry, J. M. D. Coey, *Measuring the Spin Polarization of a Metal with a Superconducting Point Contact.* Science, 1998. **282**: p. 85.

15. M. N. Baibich, et al., *Giant Magnetoresistance of (001)Fe/(001)Cr Magnetic Superlattices.* Physical Review Letters, 1988. **61**: p. 2472.

16. J. Barnaś, A. Fuss, R. E. Camley, P. Grünberg, W. Zinn *Novel magnetoresistance effect in layered magnetic structures: Theory and experiment.* Physical Review B, 1990. **42**: p. 8110.

17. S. S. P. Parkin, *Magnetotransport in Transition Metal Multilayered Structures.* Mat. -Fys. Medd. K. Dan. Vidensk. Selsk, 1997. **45**: p. 113.

18. J. Nogués, and Ivan K. Schuller, *Exchange bias.* Journal of Magnetism and Magnetic Materials, 1999. **192**: p. 203.

19. Yiming Huai, *Spin-Transfer Torque MRAM (STT-MRAM): Challenges and Prospects.* AAPPS Bulletin, 2008. **18**.

20. M. Julliere, *Tunneling between ferromagnetic films.* Physics Letters A, 1975. **54**: p. 225.

21. T. Miyazaki, and N. Tezuka, *Giant magnetic tunneling effect in Fe/Al$_2$O$_3$/Fe junction.* Journal of Magnetism and Magnetic Materials, 1995. **139**: p. L231.

22. Dexin Wang, Cathy Nordman, James M. Daughton, Zhenghong Qian, Jonathon Fink, *70% TMR at room temperature for SDT sandwich junctions with CoFeB as free and reference Layers.* IEEE TRANSACTIONS ON MAGNETICS, 2004. **40**: p. 2269.

23. Shinji Yuasa, *Giant Tunneling Magnetoresistance in MgO-Based Magnetic Tunnel Junctions.* Journal of the Physical Society of Japan, 2008. **77**: p. 031001.

24. Y. Sakuraba, M. Hattori, M. Oogane, Y. Ando, H. Kato, A. Sakuma, T. Miyazaki, H. Kubota, *Giant tunneling magnetoresistance in Co$_2$MnSi/Al–O/Co$_2$MnSi magnetic tunnel junctions.* Applied Physics Letters, 2006. **88**: p. 192508.

25. W. H. Butler, X.-G. Zhang, T. C. Schulthess, J. M. MacLaren, *Spin-dependent tunneling conductance of Fe/MgO/Fe sandwiches.* Physical Review B, 2001. **63**: p. 054416.

26. X.-G. Zhang, W. H. Butler, Amrit Bandyopadhyay, *Effects of the iron-oxide layer in Fe-FeO-MgO-Fe tunneling junctions.* Physical Review B, 2003. **68**: p. 092402.

27. Faiz Dahmani, *Effect of Seed Layer on Room Temperature Tunnel Magnetoresistance of MgO Barriers Formed by Radical Oxidation in IrMn-Based Magnetic Tunnel Junctions.* Japanese Journal of Applied Physics, 2012. **51**: p. 043002.

28. P. Grünberg, R. Schreiber, Y. Pang, M. B. Brodsky, H. Sowers, *Layered Magnetic Structures: Evidence for Antiferromagentic Coupling of Fe Layers across Cr Interlayers.* Physical Review Letters, 1986. **57**: p. 2442.

29. M. D. Stiles, in: J.A.C. Bland, B. Heinrich (Eds.), , *Ultrathin Magnetic Structures III, Chapter 3, Interlayer Exchange Coupling* 2005, Berlin: Springer.

30. B. D. Schrag, A. Anguelouch, S. Ingvarsson, Gang Xiao, Yu Lu, P. L. Trouilloud, A. Gupta, R. A. Wanner, W. J. Gallagher, P. M. Rice, S. S. P. Parkin, *Néel "orange-peel" coupling in magnetic tunneling junction devices.* Applied Physics Letters, 2000. **77**: p. 9.

31. Wei Chen, Dao N. H. Nam, Jiwei Lu, Kevin G. West, Stuart A. Wolf, *Effects of target bias voltage in magnetic tunnel junctions grown by ion beam deposition.* Journal of Applied Physics, 2009. **106**: p. 013905.

32. M. A. Ruderman, and C. Kittel, *Indirect Exchange Coupling of Nuclear Magnetic Moments by Conduction Electrons.* Physical Review, 1954. **96**: p. 99.

33. P. Bruno, and C. Chappert, *Ruderman-Kittel theory of oscillatory interlayer exchange coupling.* Physical Review B, 1992. **46**: p. 261.

34. J. C. Slonczewski, *Fluctuation mechanism for biquadratic exchange coupling in magnetic multilayers.* Physical Review Letters, 1991. **67**: p. 3172.

35. S O Demokritov, *Biquadratic interlayer coupling in layered magnetic systems.* Journal of Physics D: Applied Physics, 1998. **31**: p. 925.

36. Mark H. Kryder, Edward C. Gage, Terry W. McDaniel, William A. Challener, Robert E. Rottmayer, Ganpin Ju, Yiao-Tee Hsia, M. Fatih Erden, *Heat Assisted Magnetic Recording.* Proceedings of the IEEE, 2008. **96**: p. 1810.

37. J. A. Katine, F. J. Albert, R. A. Buhrman, *Current-Driven Magnetization Reversal and Spin-Wave Excitations in Co/Cu/Co Pillars.* Physical Review Letters, 2000. **84**: p. 3149.

38. J. C. Slonczewski, *Currents and torques in metallic magnetic multilayers.* Journal of Magnetism and Magnetic Materials, 2002. **247**: p. 324.

39. S. Mangin, D. Ravelosona, Y. Henry, J. A. Katine, Eric E. Fullerton, *Spin Transfer Torque Effects in Devices with Perpendicular Anisotropy.* AAPPS Bulletin, 2008. **18**: p. 41.

40. R. Sbiaa, S. Y. H. Lua, R. Law, H. Meng, R. Lye, H. K. Tan, *Reduction of switching current by spin transfer torque effect in perpendicular anisotropy magnetoresistive devices (invited).* Journal of Applied Physics, 2011. **109**: p. 07C707.

41. T. M. Maffitt, J. K. Debrosse, J. A. Gabric, E. T. Gow, M. C. Lamorey, J. S. Patenteau, D. R. Willmott, M. A. Wood, W. J. Gallagher, *Design considerations for MRAM.* IBM Journal of Research and Development, 2006. **50**: p. 25s.

42. S. A. Wolf, A. Y. Chtchelkanova, D. M. Treger, *Spintronics - A retrospective and perspective.* IBM Journal of Research and Development, 2006. **50**: p. 101s.

43. B. D. Cullity, and C. D. Graham, *Introduction to Magentic Materials.* 2nd ed 2009, New Jersey: John Wiley & Sons Inc.

44. L. Néel, *Anisotropie magnétique superficielle et surstructures d'orientation.* Journal de Physique et le Radium, 1954. **15**: p. 225.

45. Pavol Krivosik, Nan Mo, Sangita Kalarickal, Carl E. Patton, *Hamiltonian formalism for two magnon scattering microwave relaxation:Theory and applications.* Journal of Applied Physics, 2007. **101**: p. 083901.

46. V. Kamberský, *On the Landau–Lifshitz relaxation in ferromagnetic metals.* Canadian Journal of Physics, 1970. **48**: p. 2906.

47. M. C. Hickey, and J. S. Moodera, *Origin of Intrinsic Gilbert Damping.* Physical Review Letters, 2009. **102**: p. 137601.

48. Chando Park, Jian-Gang Zhu, Matthew T. Moneck, Yingguo Peng, David E. Laughlin, *Annealing effects on structural and transport properties of rf-sputtered CoFeB/MgO/CoFeB magnetic tunnel junctions.* Journal of Applied Physics, 2006. **99**: p. 08A901.

49. Hitoshi Kubota, Akio Fukushima, Kay Yakushiji, Satoshi Yakata, Shinji Yuasa, Koji Ando, Mikihiko Ogane, Yasuo Ando, Terunobu Miyazaki, *Reduction in switching current using a low-saturation magnetization Co–Fe–(Cr, V)–B free layer in MgO-based magnetic tunnel junctions.* Journal of Applied Physics, 2009. **105**: p. 07D117.

50. K. Oguz, M. Ozdemir, O. Dur, J. M. D. Coey, *Low magnetisation alloys for in-plane spin transfer torque devices.* Journal of Applied Physics, 2012. **111**: p. 113904.

51. R. A. de Groot, F. M. Mueller, P.G. van Engen, K. H. Buschow, *New Class of Materials: Half-Metallic Ferromagnets.* Physical Review Letters, 1983. **50**: p. 2024.

52. K.E.H.M. Hanssen, and P.E. Mijnarends, *Positron-annihilation study of the half-metallic ferromagnet NiMnSb: Theory.* Physical Review B, 1986. **34**: p. 5009.

53. M.N. Kirillova, A.A. Makhnev, E.I. Shreder, V.P. Dyakina, N.B. Gorina, *Interband Optical Absorption and Plasma Effects in Half-Metallic XMnY Ferromagnets.* Physica Status Solidi (B), 1995. **187**: p. 231.

54. I. Galanakis, P. H. Dederichs, N. Papanikolaou, *Slater-Pauling behavior and origin of the half-metallicity of the full-Heulser alloys.* Physical Review B, 2002. **66**: p. 174429.

55. Tomoya, Nakatani, PhD dissertation: *Spin-dependent scattering in CPP-GMR using Heusler alloy and the selection of the spacer material.* 2011, University of Tsukuba

56. Yoshio Miura, Kazutaka Nagao, Masafumi Shirai, *Atomic disorder effects on half-metallicity of the full-Heusler alloys Co2(Cr1-xFex)Al: A first-principles study.* Physical Review B, 2004. **69**: p. 144413.

57. Wenhong Wang, Enke Liu, Masaya Kodzuka, Hiroaki Sukegawa, Marec Wojcik, Eva Jedryka, G. H. Wu, Koichiro Inomata, Seiji Mitani, Kazuhiro Hono, *Coherent tunneling and giant tunneling magnetoresistance in $Co_2FeAl/MgO/CoFe$ magnetic tunneling junctions.* Physical Review B, 2010. **81**: p. 140402(R).

58. Wenhong Wang, Hiroaki Sukegawa, Koichiro Inomata, *Temperature dependence of tunneling magnetoresistance in epitaxial magnetic tunnel junctions using a Co_2FeAl Heusler alloy electrode.* Physical Review B, 2010. **82**: p. 092402.

59. S. Mizukami, D. Watanabe, M. Oogane, Y. Ando, Y. Miura, M. Shirai, T. Miyazaki, *Low damping constant for Co_2FeAl Heusler alloy films and its correlation with density of states.* Journal of Applied Physics, 2009. **105**: p. 07D306.

60. S. Maat, M. J. Carey, J. R. Childress, *Magnetotransport properties and spin-torque effects in current perpendicular to the plane spin valves with Co–Fe–Al magnetic layers.* Journal of Applied Physics, 2007. **101**: p. 093905.

61. Zhenchao Wen, Hiroaki Sukegawa, Seiji Mitani, Koichiro Inomata, *Perpendicular magnetization of Co2FeAl full-Heusler alloy films induced by MgO interface.* Applied Physics Letters, 2011. **98**: p. 242507.

62. H. Kono, *On the Ferromagnetic Phase in Manganese-Aluminum System.* Journal of the Physical Society of Japan, 1958. **13(12)**: p. 1444.

63. A. J. J. Koch, P. Hokkeling, M. G. V. D. Steeg, K. J. De Vos, *New Material for Permanent Magnets on a Base of Mn and Al.* Journal of Applied Physics, 1960. **31(Suppl.)**: p. 75S.

64. C. Yanar, J. M. K. Wiezorek, V. Radmilovic, W. A. Soffa, *Massive transformation and the formation of the ferromagnetic $L1_0$ phase in manganese-*

aluminum-based alloys. Metallurgical and Materials Transactions A, 2002. **33A**: p. 2413.

65. T. Sands, J. P. Harbison, M. L. Leadbeater, S. J. Allen, Jr., G. W. Hull, R. Ramesh, V. G. Keramidas, *Epitaxial ferromagnetic τ-MnAl films on GaAs.* Applied Physics Letters, 1990. **57**: p. 2609.

66. J. P. Harbison, T. Sands, R. Ramesh, L. T. Florez, B. J. Wilkens, V. G. Keramidas, *MBE growth of ferromagnetic metastable epitaxial MnAl thin films on AlAs/GaAs heterostructures.* Journal of Crystal Growth, 1991. **111**: p. 978.

67. W. Van Roy, J. De Boeck, H. Bender, C. Bruynseraede, A. Van Esch, G. Borghs, *Structural and magnetic investigations of epitaxial ferromagnetic τ MnAl films grown on GaAs/AlAs by molecular-beam epitaxy.* Journal of Applied Physics, 1995. **78**: p. 398.

68. T.M. Rosier, Y.W. He, N.A. El-Masry, *Ferromagnetic τ-MnAl epitaxially grown on (100) GaAs substrates by pulsed laser deposition.* Material Letters, 1996. **26**: p. 227.

69. G. A. Fischer, and M. L. Rudee, *Effect of magnetic annealing on the τ-phase of MnAl thin films.* Journal of Magnetism and Magnetic Materials, 2000. **213**: p. 335.

70. Akimasa Sakuma, *Electronic Structure and Magnetocrystalline Anisotropy Energy of MnAl.* Journal of the Physical Society of Japan, 1994. **63**: p. 1422.

71. S. Mizukami, S. Iihama, N. Inami, T. Hiratsuka, G. Kim, H. Naganuma, M. Oogane, Y. Ando, *Fast magnetization precession observed in $L1_0$-FePt epitaxial thin film.* Applied Physics Letters, 2011. **98**: p. 052501.

72. S. Pal, B. Rana, O. Hellwig, T. Thomson, A. Barman, *Tunable magnonic frequency and damping in $[Co/Pd]_8$ multilayers with variable Co layer thickness.* Applied Physics Letters, 2011. **98**: p. 082501.

73. Li Sun, Yukun Wang, Mao Yang, Zhaocong Huang, Ya Zhai, Yunxia Xu, Jun Du, Hongru Zhai, *Ferromagnetic resonance studies of Fe thin films with dilute heavy rare-earth impurities.* Journal of Applied Physics, 2012. **111**: p. 07A328.

74. S. Mizukami, F. Wu, A. Sakuma, J. Walowski, D. Watanabe, T. Kubota, X. Zhang, H. Naganuma, M. Oogane, Y. Ando, T. Miyazaki, *Long-Lived Ultrafast Spin Precession in Manganese Alloys Films with a Large Perpendicular Magnetic Anisotropy.* Physical Review Letters, 2011. **106**: p. 117201.

75. Masaki Hosoda, Mikihiko Oogane, Miho Kubota, Takahide Kubota, Haruaki Saruyama, Satoshi Iihama, Hiroshi Naganuma, Yasuo Ando, *Fabrication of $L1_0$-MnAl perpendicularly magnetized thin films for perpendicular magnetic tunnel junctions.* Journal of Applied Physics, 2012. **111**: p. 07A324.

76. Milton Ohring, *Materials Science of Thin films.* 2nd ed 2002, New Jersey: Academic Press.

77. P.J. Kelly, and R.D. Arnell, *Magnetron sputtering: a review of recent developments and applications.* Vacuum, 2000. **56**: p. 159.

78. Kevin G. West, PhD dissertation: *Exploration and Development of Novel Rutile Oxide Materials for Next Generation Spin Torque Transfer Heterostructures.* 2009, University of Virginia

79. Neil W. Ashcroft, and N. David Mermin, *Solid State Physics.* College ed 1976, Cornell University: Thomson Learning.

80. Susumu Okamura, Aya Miyazaki, Nobuki Tezuka, Satoshi Sugimoto, Koichiro Inomata, *Epitaxial Growth of Ordered Co$_2$(Cr$_{1-x}$Fe$_x$)Al Full-Heusler Alloy Films on Single Crystal Substrates.* Materials Transactions, 2006. **47**: p. 15.

81. N. Tezuka, S. Okamura, A. Miyazaki, M. Kikuchi, K. Inomata, *Structural dependence of the tunnel magnetoresistance for magnetic tunnel junctions with a full-Heusler Co$_2$Fe(Al,Si) electrode.* Journal of Applied Physics, 2006. **99**: p. 08T314.

82. Z. Gercsi, A. Rajanikanth, Y. K. Takahashi, K. Hono, M. Kikuchi, N. Tezuka, K. Inomate, *Spin polarization of Co$_2$FeSi full-Heusler alloy and tunneling magnetoresistance of its magnetic tunneling junctions.* Applied Physics Letters, 2006. **89**: p. 082512.

83. H. Bremers, J. Hesse, H. Ahlers, J. Sievert, D. Zachmann, *Order and magnetic properties of Fe$_{89-x}$Mn$_{11}$Al$_x$ alloys: magnetization measurements and X-ray diffraction.* Journal of Alloys and Compounds, 2004. **366**: p. 67.

84. K. Barmak, J. Kim, L. H. Lewis, K. R. Coffey, M. F. Toney, A. J. Kellock, J.-U. Thiele,, *On the relationship of magnetocrystalline anisotropy and stoichiometry in epitaxial L1$_0$ CoPt (001) and FePt (001) thin films.* Journal of Applied Physics, 2005. **98**: p. 033904.

85. A. Cebollada, R. F. C. Farrow, M. F. Toney, *Magnetic Nanostructures* 2002, California: American Scientific Publisher.

86. M T Johnsony, P J H Bloemenzx, F J A den Broedery, J J de Vriesz,, *Magnetic anisotropy in metallic multilayers* Reports on Progress in Physics, 1996. **59**: p. 1409.

87. O. Ersen, V. Parasote, V. Pierron-Bohnes, M. C. Cadeville, C. Ulhaq-Bouillet, *Growth conditions to optimize chemical order and magnetic properties in molecular-beam-epitaxy-grown CoPt/MgO(001) thin films.* Journal of Applied Physics, 2003. **93**: p. 2987.

88. Yishen Cui, Wenjing Yin, Wei Chen, Jiwei Lu, Stuart A. Wolf, *Epitaxial τ phase MnAl thin films on MgO (001) with thickness-dependent magnetic anisotropy.* Journal of Applied Physics, 2011. **110**: p. 103909.

89. C. Kittel, *Introduction to Solid State Physics*. 8th ed 2005, New York: John Wiley & Sons Inc.

90. R.D. McMichael, M. D. Stiles, P. J. Chen, W. F. Egelhoff, *Ferromagnetic resonance linewidth in thin films coupled to NiO.* Journal of Applied Physics, 1998. **83**: p. 7037.

91. M. J. Hurben, and C. E. Patton, *Theory of two magnon scattering microwave relaxation and ferromagnetic resonance linewidth in magnetic thin films.* Journal of Applied Physics, 1998. **83**: p. 4344.

92. S. Keshavarz, Y. Xu, S. Hrdy, C. Lemley, T. Mewes, Y. Bao, *Relaxation of Polymer Coated Fe$_3$O$_4$ Magnetic Nanoparticles in Aqueous Solution.* IEEE TRANSACTIONS ON MAGNETICS, 2010. **46**: p. 1541.

93. M. J. M. de Jong, and C. W. J. Beenakker *Andreev Reflection in Ferromagnet-Superconductor Junctions.* Physical Review Letters, 1995. **74**: p. 1657.

94. L.J. Van der Pauw, *A method of measuring specific resistivity and Hall effect of discs of arbitrary shape.* Philips Research Reports, 1958. **13**: p. 1.

95. Wenjing Yin, PhD dissertation: *Diluted Magnetic MnxGe1-x for Nanostructure Devices*. 2011, University of Virginia

96. C. Y. You, T. Ohkubo, Y. K. Takahashi, K. Hono, *Boron segregation in crystallized MgO/amorphous-$Co_{40}Fe_{40}B_{20}$ thin films.* Journal of Applied Physics, 2008. **104**: p. 033517.

97. P. Gupta, Tapas Ganguli, A. Gupta, A. K. Sinha, S. K. Deb, P. Svec Jr., V. Franco, *Influence of isochronal annealing on the microstructure and magnetic properties of Cu-free HITPERM $Fe_{40.5}Co_{40.5}Nb_7B_{12}$ alloy.* Journal of Applied Physics, 2012. **111**: p. 113518.

98. Vsevolod I. Razumovskiy, Andrei V. Ruban, Pavel A. Korzhavyi, *First-principles study of elastic properties of Cr- and Fe-rich Fe-Cr alloys.* Physical Review B, 2011. **84**: p. 024106.

99. A. Williams, V. Moruzzi, A. Malozemoff, K. Terakura, *Generalized Slater-Pauling curve for transition-metal magnets.* IEEE TRANSACTIONS ON MAGNETICS, 1983. **19**: p. 1983.

100. M. Sostarich, *Generalized Slater–Pauling curve and the role of metalloids in Fe-based amorphous alloys.* Journal of Applied Physics, 1990. **67**: p. 5793.

101. V. Saraswati, and P. L. Paulose, *Magnetic susceptibility and magnetic resonance in boron and boron carbides.* Journal of the Less-Common Metals, 1987. **128**: p. 185.

102. Yung-Hung Wang, Wei-Chuan Chen, Shan-Yi Yang, Kuei-Hung Shen, Chando Park, Ming-Jer Kao, Ming-Jinn Tsai *Interfacial and annealing effects on magnetic properties of CoFeB thin films.* Journal of Applied Physics, 2006. **99**: p. 08M307.

103. T. Dimopoulos, G. Gieres, J. Wecker, N. Wiese, M. D. Sacher *Thermal annealing of junctions with amorphous and polycrystalline ferromagnetic electrodes* Journal of Applied Physics, 2004. **96**: p. 6382.

104. J.D. Livingston, *A review of coercivity mechanisms (invited).* Journal of Applied Physics, 1981. **52**: p. 2544.

105. S. Jin, D. Brasen, and S. Mahajan, *Coercivity mechanisms in FeCrCo magnet alloys.* Journal of Applied Physics, 1982. **53**: p. 4300.

106. L. Tang, G. Thomas, Mahbub R. Khan, S. L. Duan, Neil Heiman, *Magnetic properties and microstructures of CoNiCr and CoFeCr thin films.* Journal of Applied Physics, 1991. **69**: p. 5166.

107. Tsung-Shune Chin, Kou-Her Wang, Cheng-Hsiung Lin, *High Coercivity Fe-Cr-Co Thin Films by Vacuum Evaporation.* Japanese Journal of Applied Physics, 1991. **30**: p. 1692.

108. S. Mahajan, E. M. Gyorgy, R. C. Sherwood, S. Jin, S. Nakahara, D. Brasen, M. Eibschutz, *Origin of coercivity in a Cr-Co-Fe alloy (chromindur).* Applied Physics Letters, 1978. **32**: p. 633.

109. Y. Belli, M. Okada, G. Thomas, M. Homma, H. Kaneko, *Microstructure and magnetic properties of FeCrCoV alloys.* Journal of Applied Physics, 1978. **49**: p. 2049.

110. Chih-Liang Wang, Sheng-Huang Huang, Chih-Huang Lai, Wei-Chuan Chen, Shan-Yi Yang, Kuei-Hung Shen, Hui-Yun Bor, *Reduction in critical current density by tuning damping constants of CoFeB for spin-torque-transfer switching* Journal of Physics D: Applied Physics, 2009. **42**: p. 115006.

111. Xiaoyong Liu, Wenzhe Zhang, Matthew J. Carter, Gang Xiao, *Ferromagnetic resonance and damping properties of CoFeB thin films as free layers in MgO-based magnetic tunnel junctions.* Journal of Applied Physics, 2011. **110**: p. 033910.

112. S.V. Karthik, A. Rajanikanth, Y.K. Takahashi, T. Ohkubo, K. Hono, *Microstructure and spin polarization of quaternary $Co_2Cr_{1-x}V_xAl$, $Co_2V_{1-x}Fe_xAl$ and $Co_2Cr_{1-x}Fe_xAl$ Heusler alloys.* Acta Materialia, 2007. **55**: p. 3867.

113. R. Kelekar, and B. M. Clemens, *Epitaxial growth of the Heusler alloy $Co_2Cr_{1-x}Fe_xAl$.* Journal of Applied Physics, 2004. **96**: p. 540.

114. K. H. J. Buschow, and P. G. van Engen, *Magnetic and magneto-optical properties of heusler alloys based on aluminium and gallium.* Journal of Magnetism and Magnetic Materials, 1981. **25**: p. 90.

115. Chunsheng Liu, Claudia K. A. Mewes, Mairbek Chshiev, Tim Mewes, William H. Butler, *Origin of low Gilbert damping in half metals.* Applied Physics Letter, 2009. **95**: p. 022509.

116. I. Galanakis, *Orbital magnetism in the half-metallic Heusler alloys.* Physical Review B, 2005. **71**: p. 012413.

117. Simon Trudel, Oksana Gaier, Jaroslav Hamrle, Burkard Hillebrands, *Magnetic anisotropy, exchange and damping in cobalt-based full Heusler compounds: An experimental review.* Journal of Physics D: Applied Physics, 2010. **43**: p. 193001.

118. T. Kubota, S. Tsunegi, M. Oogane, S. Mizukami, T. Miyazaki, H. Naganuma, Y. Ando, *Half-metallicity and Gilbert damping constant in $Co_2Fe_xMn_{1-x}Si$ Heusler alloys depending on the film composition.* Applied Physics Letter, 2009. **94**: p. 122504.

119. Mahdi Sargolzaei, Manuel Richter, Klaus Koepernik, Ingo Opahle, Helmut Eschrig, Igor Chaplygin, *Spin and orbital magnetism in full Heusler alloys: A density functional theory study of Co_2YZ (Y=Mn,Fe; Z=Al, Si,Ga,Ge).* Physical Review B, 2006. **74**: p. 224410.

120. Andreas Mann, PhD dissertation: *Determining the Spin Polarization of Heusler Compounds via Femtosecond Magnetization Dynamics.* 2010, Georg-August-Universität

121. G. T. Woods, R. J. Soulen, Jr., I. Mazin, B. Nadgorny, M. S. Osofsky, J. Sanders, H. Srikanth, W. F. Egelhoff, R. Datla, *Analysis of point-contact Andreev reflection spectra in spin polarization measurements.* Physical Review B, 2004. **70**: p. 054416.

122. Gerhard H Fecher, Hem Chandra Kandpal, Sabine Wurmehl, Jonder Morais, Hong-Ji Lin, Hans-Joachim Elmers, Gerd Schönhense, Claudia Felser, *Design of magnetic materials: the electronic structure of the ordered, doped Heusler compound $Co_2Cr_{1-x}Fe_xAl$.* Journal of Physics: Condensed Matter, 2005. **17**: p. 7237.

123. B. Nadgorny, M. S. Osofsky, D.J. Singh, G.T. Woods, R. J. Soulen, Jr., M. K. Lee, S.D. Bu, C. B. Eom, *Measurements of spin polarization of epitaxial SrRuO3 thin films.* Applied Physics Letter, 2003. **82**: p. 427.

124. S. Okamura, A. Miyazaki, S. Sugimoto, N. Tezuka, K. Inomata, *Large tunnel magnetoresistance at room temperature with a Co_2FeAl full-Heusler alloy electrode.* Applied Physics Letter, 2005. **86**: p. 232503.

125. Brent Fultz, and James M. Howe, *Transmission Electron Microscopy and Diffractometry of Materials*. 3rd ed 2007: Springer.

126. H. X. Yang, M. Chshiev, B. Dieny, J. H. Lee, A. Manchon, K. H. Shin, *First-principles investigation of the very large perpendicular magnetic anisotropy at Fe/MgO and Co/MgO interfaces.* Physical Review B, 2011. **84**: p. 054401.

127. S. Monso, B. Rodmacq, S. Auffret, G. Casali, F. Fettar, B. Gilles, B. Dieny, P. Boyer, *Crossover from in-plane to perpendicular anisotropy in Pt/CoFe/AlO$_x$ sandwiches as a function of Al oxidation: A very accurate control of the oxidation of tunnel barriers.* Applied Physics Letter, 2002. **80**: p. 4157.

128. Riki Shimabukuro, Kohji Nakamura, Toru Akiyama,Tomonori Ito, *Electric field effects on magnetocrystalline anisotropy in ferromagnetic Fe monolayers.* Physica E, 2010. **42**: p. 1014.

129. Wei-Gang Wang, Stephen Hageman, Mingen Li, Sunxiang Huang, Xiaoming Kou, Xin Fan, John Q. Xiao, C. L. Chien, *Rapid thermal annealing study of magnetoresistance and perpendicular anisotropy in magnetic tunnel junctions based on MgO and CoFeB.* Applied Physics Letter, 2011. **99**: p. 102502.

130. S. Ikeda, K. Miura, H. Yamamoto, K. Mizunuma, H. D. Gan, M. Endo, S. Kanai, J. Hayakawa, F. Matsukura and H. Ohno, *A perpendicular-anisotropy CoFeB–MgO magnetic tunnel junction.* Nature Materials, 2010. **9**: p. 721.

131. Manli Ding, and S. Joseph Poon, *Perpendicular magnetization of CoFeGe films induced by MgO interface.* Applied Physics Letters, 2012. **101**: p. 122408.

132. Yasushi Endo, Yoshio Mitsuzuka, Yutaka Shimada, Masahiro Yamaguchi, *Study on the Damping Constants of Ni-Fe Thin Films using Different CPW-FMR Measurements.* IEEJ Transactions on Fundamentals and Materials, 2011. **131**: p. 505.

133. Yaroslav Tserkovnyak, and Arne Brataas, *Enhanced Gilbert Damping in Thin Ferromagnetic Films.* Physical Review Letters, 2002. **88**: p. 117601-1.

134. Hiroaki Sukegawa, Zhenchao Wen, Kouta Kondou, Shinya Kasai, Seiji Mitani, Koichiro Inomata, *Spin-transfer switching in full-Heusler Co2FeAl-based magnetic tunnel junctions.* Applied Physics Letter, 2012. **100**: p. 182403.

135. P. de Person, P. Warin, M. Jamet, C. Beigne, Y. Samson, *Magnetic coupling between high magnetization perpendicular electrodes in an epitaxial FePt/MgO/FePt magnetic tunnel junction.* Physical Review B, 2007. **76**: p. 184402.

136. Y. Hirayama, T. Takeuchi, M. Futamoto, *On the origin of ferromagnetism in Mn-Al multilayered films.* Journal of Applied Physics, 1993. **73**: p. 1348.

137. Y. Hirayama, T. Takeuchi, M. Futamoto, *Layer thickness dependence of magnetic properties in Mn/Al multilayers.* Journal of Applied Physics, 1993. **73**: p. 6441.

138. T. Takeuchi, Y. Hirayama, M. Futamoto, *Dependence of anisotropy in Mn-Al multilayer films on the number of layers.* Journal of Magnetism and Magnetic Materials, 1992. **104**.

139. Y. Hirayama, T. Takeuchi, M. Futamoto, *Torque Measurements of Ferromagnetic Mn-Al Multilayered Films.* Japanese Journal of Applied Physics, 1992. **31**: p. 1798.

140. J. H. Park, Y. K. Hong, S. Bae, J. J. Lee, J. Jalli, G. S. Abo, N. Neveu, S. G. Kim, C. J. Choi, J. G. Lee, *Saturation magnetization and crystalline anisotropy*

calculations for MnAl permanent magnet. Journal of Applied Physics, 2010. **107**: p. 09A731.

141. M. van Kampen, C. Jozsa, J. T. Kohlhepp, P. LeClair, L. Lagae, W. J. M. de Jonge, B. Koopmans, *All-Optical Probe of Coherent Spin Waves.* Physical Review Letters, 2002. **88**: p. 227201-1.

142. H. Wang, S. Mitani, A. Sato, K. Saito, K. Takanashi, K. Yakushiji, *Numerical simulation of magnetization process in epitaxial $Co_2MnSi/Cr/Co_2MnSi$ trilayers with oscillatory interlayer coupling.* Journal of Applied Physics, 2007. **101**: p. 09J510.

143. H. Wang, A. Sato, K. Saito, S. Mitani, K. Takanashi, K. Yakushiji, *Oscillatory interlayer exchange coupling in epitaxial $Co_2MnSi/Cr/Co_2MnSi$ trilayers.* Applied Physics Letters, 2007. **90**: p. 142510.

144. N. Wiese, T. Dimopoulos, M. Rührig, J. Wecker, H. Brückl, G. Reiss, *Antiferromagnetically coupled CoFeB/Ru/CoFeB trilayers* Applied Physics Letters, 2004. **85**: p. 2020.

145. N. Wiese, T. Dimopoulos, M. Rührig, J. Wecker, G. Reiss, J. Nogues, J. Sort, *Strong temperature dependence of antiferromagnetic coupling in CoFeB/Ru/CoFeB.* Europhysics Letters, 2007. **78**: p. 67002.

146. S. Bosu, Y. Sakuraba, K. Saito, H. Wang, S. Mitani, K. Takanashi, C. Y. You, K. Hono *Interlayer thickness dependence of $90°$ exchange coupling in $Co_2MnAl/Cr/Co_2MnAl$ epitaxial trilayer structures* Journal of Applied Physics, 2009. **105**: p. 07C710.

147. Subrojati Bosu, Yuya Sakuraba, Kesami Saito, Hai Wang, Koki Takanashi, *Interlayer Exchange Coupling in Full Heusler $Co_2FeSi/Cr/Co_2FeSi$ Epitaxial Trilayer Structures.* IEEE TRANSACTIONS ON MAGNETICS, 2010. **46**: p. 2052.

148. Xiaoguang Xu, Jianli Zhang, Lei Sha, Delin Zhang, Yong Jiang, *A clear oscillation of the interlayer exchange coupling in $Co_2FeAl/Cr/Co_2FeAl$ structure with MgO capping layer.* Journal of Applied Physics, 2012. **112**: p. 073904.

149. S. S. P. Parkin, N. More, K. P. Roche, *Oscillations in Exchange Coupling and Magnetoresistance in Metallic Superlattice Structures: Co/Ru, Co/Cr, and Fe/Cr.* Physical Review Letters, 1990. **64**: p. 2304.

150. J. Unguris, R. J. Celotta, D. T. Pierce, *Observation of Two Different Oscillation Periods in the Exchange Coupling of Fe/Cr/Fe(100).* Physical Review Letters, 1991. **67**: p. 140.

151. Mark van Schilfgaarde, and Walter A. Harrison, *Oscillatory Exchange Coupling: RKKY or Quantum-Well Mechanism?* Physical Review Letters, 1993. **71**: p. 3870.

152. D. T. Pierce, Joseph A. Stroscio, J. Unguris, R. J. Celotta, *Influence of Cr growth on exchange coupling in Fe/Cr/Fe(100).* Physical Review B, 1994. **49**: p. 14564.

153. S. Mirbt, A. M. N. Niklasson, B. Johansson, H. L. Skriver, *Calculated oscillation periods of the interlayer coupling in Fe/Cr/Fe and Fe/Mo/Fe sandwiches.* Physical Review B, 1996. **54**: p. 6382.

154. M. D. Stiles, *Oscillatory Exchange Coupling in Fe/Cr Multilayers.* Physical Review B, 1996. **54**: p. 14679.

155. Sergey O. Demokritov, Alexey B. Drovosekov, Dmitry I. Kholin, Natalia M. Kreines, *Temperature dependence of interlayer coupling in a Fe/Cr/Fe wedge*

sample. MOKE and MBLS studies. Journal of Magnetism and Magnetic Materials, 2003. **258–259**: p. 391.

156. Eric E. Fullerton, K. T. Riggs, C. H. Sowers, S.D. Bader, and A. Berger, *Suppression of Biquadratic Coupling in Fe/Cr(001) Superlattices below the Néel Transition of Cr.* Physical Review Letters, 1995. **75**: p. 330.

157. M. Schäfer, S. Demokritov, S. Müller-Pfeiffer, R. Schäfer, M. Schneider, P. Grünberg, W. Zinn, *Investigation of 90° coupling in FelAglFe structures: "Loose spins" and fluctuation mechanism.* Journal of Applied Physics, 1995. **77**: p. 6432.

158. Eric E. Fullerton, and S. D. Bader *Temperature-dependent biquadratic coupling in antiferromagnetically coupled Fe/FeSi multilayers.* Physical Review B, 1996. **53**: p. 5112.

159. W. H. Meiklejohn, and C. P. Bean *New Magnetic Anisotropy.* Physical Review, 1956. **102**: p. 1413.

160. Wei Chen, Dao N. H. Nam, Jiwei Lu, Stuart A. Wolf, *Detection of bottom ferromagnetic electrode oxidation in magnetic tunnel junctions by magnetometry measurements.* Journal of Applied Physics, 2010. **108**: p. 113918.

161. M. Ali, C. H. Marrows, M. Al-Jawad, B. J. Hickey, A. Misra, U. Nowak, K. D. Usadel, *Antiferromagnetic layer thickness dependence of the IrMn/Co exchange bias system.* Physical Review B, 2003. **68**: p. 214420.

162. Haiwen Xi, and Robert M. White, *Antiferromagnetic thickness dependence of exchange biasing.* Physical Review B, 2000. **61**: p. 80.

163. T. M. Nakatani, A. Rajanikanth, Z. Gercsi, Y. K. Takahashi, K. Inomata, K. Hono *Structure, magnetic property, and spin polarization of $Co_2FeAl_xSi_{1-x}$ Heusler alloys.* Journal of Applied Physics, 2007. **102**: p. 033916.

164. M. Tanaka, J. P. Harbison, J. DeBoeck, T. Sands, B. Philips, T. L. Cheeks, V. G. Keramidas, *Epitaxial growth of ferromagnetic ultrathin MnGa films with perpendicular magnetization on GaAs.* Applied Physics Letters, 1993. **62**: p. 1565.

165. H. Kurt, K. Rode, M. Venkatesan, P. Stamenov, J. M. D. Coey, *$Mn_{3-x}Ga$ ($0 \leq x \leq 1$): Multifunctional thin film materials for spintronics and magnetic recording.* Physica Status Solidi B, 2011. **248**: p. 2338.